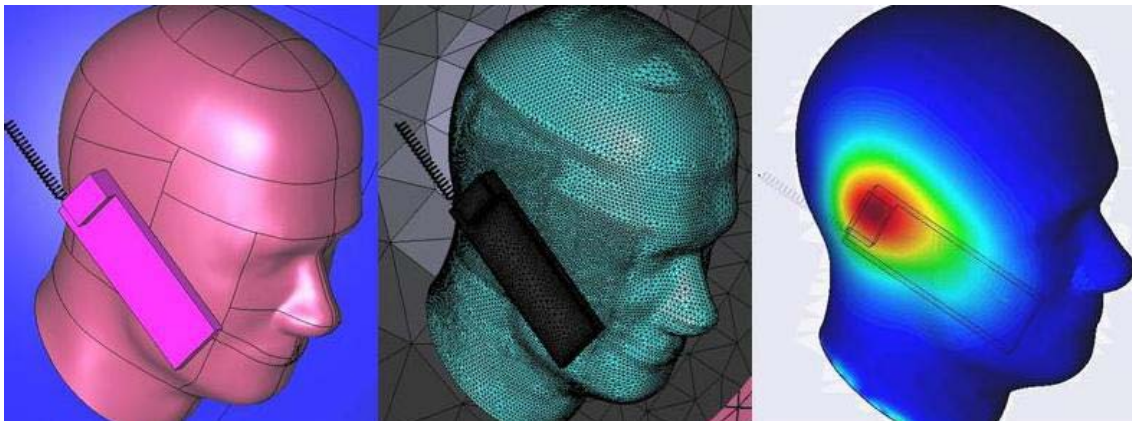


Regularized Maxwell Equations and Nodal Finite Elements for Electromagnetic Field Computations in Frequency Domain

Ruben Otín
Eugenio Oñate



Regularized Maxwell Equations and Nodal Finite Elements for Electromagnetic Field Computations in Frequency Domain

R. Otin, E. Oñate

Monograph CIMNE N°-123, May 2011

INTERNATIONAL CENTER FOR NUMERICAL METHODS IN ENGINEERING
Edificio C1, Campus Norte UPC
Gran Capitán s/n
08034 Barcelona, Spain
www.cimne.upc.es

First edition: May 2011

**REGULARIZED MAXWELL EQUATIONS AND NODAL FINITE ELEMENTS FOR ELECTROMAGNETIC
FIELD COMPUTATIONS IN FREQUENCY DOMAIN**

Monograph CIMNE M123

© The authors

ISBN: 978-84-89925-03-8

Depósito legal: B-20827-2011

Abstract

In this work we present an alternative approach to the usual finite element formulation based on edge elements and double-curl Maxwell equations. This alternative approach is based on nodal elements and regularized Maxwell equations. The advantages are that, without adding extra unknowns (such as Lagrange multipliers), it provides spurious-free solutions and well-conditioned matrices. Besides, its integral representation involves a less singular kernel (order 1 instead of 3), which makes this approach best suited to hybridization with integral numerical techniques. On the other hand, a new set of difficulties arises that were not present in the classical formulation. The main drawback is that a globally wrong solution is obtained when the electromagnetic field has a singularity in the problem domain. Also, boundary conditions and field discontinuities are more laborious to implement. This work explains how to overcome these difficulties and demonstrates that accurate solutions can be obtained with nodal elements and the regularized formulation.

We also present ERMES, the C++ implementation of the finite element approach depicted above and the main deliverable of this work. We compute with ERMES the scattering parameters of microwave filters and the specific absorption rate induced in a body when exposed to electromagnetic fields. ERMES is also the computational tool used in two novel numerical models introduced in this work. The first one characterizes electromagnetic metal forming processes and the second one the transfer impedance of cable shields.

The electromagnetic metal forming model calculates the driving Lorentz force and estimates the optimum frequency at which it is attained the maximum workpiece deformation. The main advantage of the approach is that it provides an explicit relation between the capacitance of the capacitor bank and the frequency of the discharge, which is a key parameter in the design of an electromagnetic forming system. The successful application of the regularized formulation in this model reveals its excellent behavior in the low-frequency (quasi-static) regime.

The second numerical model introduced in this work computes the transfer impedance of cable shields. The model reproduces the high frequency behavior of the transfer impedance more accurately than the approaches found in the literature and, moreover, it is able to analyze a wider variety of geometries and materials.

Keywords: finite element method, regularized Maxwell equations, nodal elements, scattering parameters, microwave engineering, specific absorption rate, antenna design, electromagnetic forming, optimum capacitance, transfer impedance, shielded cables, electromagnetic compatibility.

Contents

1	Introduction	11
1.1	Motivation	11
1.2	Outline of this monograph	12
2	Electromagnetic theory	13
2.1	Maxwell's equations	13
2.1.1	Lorentz force	15
2.1.2	Constitutive relations	16
2.2	Potentials	17
2.3	Time-harmonic Maxwell's equations	19
2.3.1	Time-harmonic Maxwell's equations in linear isotropic media	20
2.4	Fields at the interface between two media	22
2.4.1	Perfect electric conductor	23
2.4.2	Imperfect electric conductor	24
2.5	Radiation condition	24
2.6	Wave equation	25
2.7	Poynting theorem	25
2.8	Summary	26
3	Regularized Maxwell equations and nodal finite elements	27
3.1	Introduction	27
3.2	Double-curl Maxwell equations and edge elements	28
3.3	Regularized Maxwell equations and nodal elements	30
3.4	Nodal elements and field discontinuities	31
3.5	Regularized formulation and field singularities	32
3.6	Validation examples in two dimensions	34
3.7	Validation examples in three dimensions	44
3.8	Summary	48
4	Specific absorption rate computations	49
4.1	Introduction	49
4.2	Definitions	50
4.3	Numerical tool	51

4.4	Ellipsoidal phantom in rectangular waveguide	51
4.4.1	Description of the problem	51
4.4.2	Finite element model	51
4.4.3	Results	52
4.5	PROCOM MU9-XP4 antenna installed on motorbike	53
4.5.1	Description of the problem	53
4.5.2	Finite element model	54
4.5.3	Results	54
4.6	PMR antenna near SAM head	59
4.6.1	Description of the problem	59
4.6.2	Finite element model	59
4.6.3	Results	60
4.7	RFID antenna near vials of blood plasma	64
4.7.1	Description of the problem	64
4.7.2	Finite element model	64
4.7.3	Results	65
4.8	Summary	72
5	Electromagnetic metal forming	73
5.1	Introduction	73
5.2	Coupling strategies	74
5.3	Electromagnetic model	75
5.3.1	Input data	76
5.3.2	Inductance and resistance of the system coil-workpiece	77
5.3.3	Intensity in the RLC circuit	77
5.3.4	Capacitance and frequency	78
5.3.5	Lorentz force on the workpiece	79
5.3.6	Lorentz force in frequency domain	80
5.4	Numerical analysis tools	81
5.5	Application example I. Sheet bulging.	81
5.5.1	Description of the system coil-workpiece	81
5.5.2	Finite element model	82
5.5.3	Intensity through the RLC circuit	84
5.5.4	Magnetic pressure on the workpiece	87
5.5.5	Deflection of the workpiece	92
5.6	Application example II. Tube bulging.	93
5.6.1	Description of the system coil-workpiece	93
5.6.2	Finite element model	94
5.6.3	Intensity through the RLC circuit	94
5.6.4	Magnetic pressure on the workpiece	95
5.6.5	Deflection of the workpiece	95
5.7	Optimum frequency and optimum capacitance	97
5.8	Optimum capacitance estimation	98

5.8.1	Tube bulging	98
5.8.2	Tube compression	99
5.9	Summary	101
6	Transfer impedance of cable shields	103
6.1	Introduction	103
6.2	Definitions	104
6.3	Finite element model	106
6.4	Validation	108
6.4.1	Homogeneous tube	110
6.4.2	Perforated tubes with circular holes	111
6.4.3	Standard RG 58 coaxial cable tinned	113
6.5	Summary	118
7	Conclusions and future work	119
7.1	Regularized Maxwell equations and nodal finite elements	119
7.2	Electromagnetic metal forming	120
7.3	Transfer impedance of cable shields	120
A	ERMES: Numerical tool for electromagnetic field computations	121
A.1	Description of ERMES	121
A.2	Installation	121
A.3	Pre-Process	122
A.3.1	Materials	123
A.3.2	RWPport TE10	124
A.3.3	CoaxialPort TEM	125
A.3.4	Generic Robin Coefficients	126
A.3.5	Current Sources Properties	127
A.3.6	Dirichlet Conditions	128
A.3.7	Robin Conditions	129
A.3.8	Current Sources	130
A.3.9	Modes Projection	131
A.3.10	Solving Parameters	132
A.3.11	Results	134
A.4	Post-Process	135
A.4.1	Single frequency	135
A.4.2	Frequency sweep	135

Chapter 1

Introduction

This chapter exposes the motivation for writing this monograph and how the work is organized.

1.1 Motivation

The main contribution of this work is the development, implementation and application of a finite element formulation based on nodal elements and the regularized Maxwell equations. The generality and flexibility of this formulation allows its application in a wide variety of situations such in microwave engineering, specific absorption rate computations, antenna design, eddy currents, electromagnetic metal forming, cable shielding modeling, etc. This formulation offers, in principle, well-conditioned matrixes, an easier hybridization with integral numerical techniques and an easier multi-physics coupling with other numerical models that also use nodal elements. These features makes the regularized formulation an ideal choice to solve most of the problems encountered in the electromagnetic projects in which CIMNE was involved. Moreover, its study opens new paths and broadens the current knowledge in computational electromagnetism.

The finite element formulation developed in this work has been implemented in a C++ code called ERMES. This code is a user-friendly computational tool that has been applied to the above mentioned problems successfully. But, why develop another finite element code?, why not use the available commercial software?. The answer to the these questions is that, sometimes, you need to obtain results that the available commercial codes do not provide. In such a situations, you have two options, to adapt an existent software tool or to make a new one from scratch. To adapt an existent software requires full access to the internal algorithms of the tool and, usually, that is only possible with an in-house code. Furthermore, an in-house code is a cheaper option, it allows to know exactly the mathematical formulation behind it and it permits to test new algorithms. Therefore, to modify an in-house code or to make a new one from scratch, even although you can end up with a code less efficient than the commercial ones, is an advantageous option for the numerical methods research community.

1.2 Outline of this monograph

Because of the heterogenous nature of this work, each chapter has its own introduction and literature review. The monograph is organized as follows:

Chapter 2 briefly reviews the fundamentals of the classical electromagnetic theory. Its main objective is to introduce the notation and the basic formulas that will be used throughout this work.

Chapter 3 presents the main contribution of this work, i.e. the finite element formulation based on nodal elements and regularized Maxwell equations. It exposes its advantages and drawbacks and explains how to overcome the new difficulties that this formulation arises. The method is validated here computing the fields and scattering parameters of microwave filters and comparing the results with measurements and other numerical techniques.

Chapter 4 applies the formulation of chapter 3 to the computation of the specific absorption rate (SAR). It proves the applicability of the method for solving real-life problems. This chapter shows the SAR induced in an ellipsoidal phantom inside rectangular waveguide, a human dummy near an antenna installed on a motorbike and a dummy head near a PMR antenna. Also, at the end of the chapter, it is studied the thermal effects induced by a RFID antenna in vials filled with blood plasma.

Chapter 5 presents a numerical model for electromagnetic metal forming processes. It shows how the model calculates the driving Lorentz force and estimates the optimum frequency and capacitance at which it is attained the maximum workpiece deformation for a given set of coil, workpiece and initial energy. This chapter reveals the applicability of the regularized formulation to low-frequency (quasi-static) problems.

Chapter 6 presents a numerical model for computing the transfer impedance of a cable shield. It validates the model for perforated tubes and shows that it reproduces the high frequency behavior of the transfer impedance more accurately than the approaches found in the literature.

Chapter 7 summarizes the main conclusions of this work and the futures lines of research and development.

Finally, in the appendix A, it is shown the user manual of ERMES, the C++ code which implements the finite element formulation of chapter 3.

Chapter 2

Electromagnetic theory

This chapter briefly reviews the fundamentals of the classical electromagnetic theory. Only the portions of the electromagnetic theory needed to understand the developments of the following chapters will be presented here. If it is desired a more detailed information on the fundamentals of electromagnetic theory we recommend the books [42, 30, 91, 56, 103, 113, 90]. For more advanced topics and specific applications in frequency domain we recommend [2, 35, 12].

2.1 Maxwell's equations

In the second half of the 19th century James Clerk Maxwell established in [61, 62] a set of twenty equations with twenty unknowns that summarized all the electromagnetic phenomena known in those days. This set of equations was later reduced by Oliver Heaviside [37, 68], who simplified and transformed the original set with the help of the vector notation developed by himself concurrently with Josiah Willard Gibbs [116, 115]. The term *Maxwell's equations* is nowadays applied to the simplified version due to Heaviside:

$$\nabla \cdot \mathbf{D} = \rho, \quad (2.1)$$

$$\nabla \times \mathbf{H} - \frac{\partial \mathbf{D}}{\partial t} = \mathbf{J}, \quad (2.2)$$

$$\nabla \times \mathbf{E} + \frac{\partial \mathbf{B}}{\partial t} = 0, \quad (2.3)$$

$$\nabla \cdot \mathbf{B} = 0, \quad (2.4)$$

where the vector functions \mathbf{E} , \mathbf{D} , \mathbf{B} and \mathbf{H} are usually called (although there is no universal agreement and different names can be found in the literature):

\mathbf{E} : electric field (*volt/meter*),

\mathbf{D} : electric displacement field (*coulomb/meter²*),

B: magnetic induction (*tesla*),

H: magnetic field (*ampere/meter*).

The sources that generate these electromagnetic fields are:

J: electric current density (*ampere/meter²*),

ρ : electric charge density (*coulomb/meter³*),

which are related through the continuity equation

$$\nabla \cdot \mathbf{J} + \frac{\partial \rho}{\partial t} = 0. \quad (2.5)$$

The above relation express the law of conservation of charge. This law can be deduced from equations (2.2) and (2.1) using the fact that, for any vector function \mathbf{F} , is satisfied

$$\nabla \cdot (\nabla \times \mathbf{F}) = 0. \quad (2.6)$$

The symbols $\nabla \cdot$ and $\nabla \times$ correspond to the divergence and the curl, respectively. The divergence is defined by

$$\nabla \cdot \mathbf{F} \equiv \lim_{V \rightarrow 0} \frac{1}{V} \oint_S \mathbf{F} \cdot \hat{\mathbf{n}} \, dS, \quad (2.7)$$

where \mathbf{F} is a vector function, V is an arbitrary volume, S is the surface of that volume, and the integral, is a surface integral with $\hat{\mathbf{n}}$ being the outward normal to the surface S . In a cartesian coordinates system, with $\mathbf{F} = F_x \hat{\mathbf{x}} + F_y \hat{\mathbf{y}} + F_z \hat{\mathbf{z}}$, the divergence takes the form

$$\nabla \cdot \mathbf{F} = \frac{\partial F_x}{\partial x} + \frac{\partial F_y}{\partial y} + \frac{\partial F_z}{\partial z}. \quad (2.8)$$

The curl, in the direction given by the unit vector $\hat{\mathbf{n}}$, is defined by

$$(\nabla \times \mathbf{F}) \cdot \hat{\mathbf{n}} \equiv \lim_{S \rightarrow 0} \frac{1}{S} \oint_C \mathbf{F} \cdot d\mathbf{x}, \quad (2.9)$$

where \mathbf{F} is a vector function, and the integral, is a line integral along the boundary C of the area S , which is perpendicular to $\hat{\mathbf{n}}$. In a cartesian coordinates system, with $\mathbf{F} = F_x \hat{\mathbf{x}} + F_y \hat{\mathbf{y}} + F_z \hat{\mathbf{z}}$, the curl takes the form

$$\nabla \times \mathbf{F} = \left(\frac{\partial F_z}{\partial y} - \frac{\partial F_y}{\partial z} \right) \hat{\mathbf{x}} + \left(\frac{\partial F_x}{\partial z} - \frac{\partial F_z}{\partial x} \right) \hat{\mathbf{y}} + \left(\frac{\partial F_y}{\partial x} - \frac{\partial F_x}{\partial y} \right) \hat{\mathbf{z}}. \quad (2.10)$$

In principle, it is recognized that Maxwell's equations are always valid, and that, if a vector function satisfies them, it is a possible electromagnetic field. This statement is, of course, subject to the assumption that the boundary conditions, source distribution and material's properties are coherent and have physical meaning. We must keep in mind that the Maxwell's equations are not more than the mathematical expression of some experimental results, that is:

- (2.1) summarizes Coulomb's law of forces plus the effects of matter,
 (2.2) represents an extension of Ampere's circuital law,
 (2.3) represents Faraday's law of induction,
 (2.4) proclaims the non-existence of magnetic monopoles.

Under these circumstances, Maxwell's equations can not be demonstrated, but its applicability can be verified experimentally. Therefore, as a result of an extensive experimental work, it is considered that these set of equations can be applied to almost all macroscopic situations and they are used as guiding principles in the same way as we use the conservation of energy or the conservation of the linear momentum.

2.1.1 Lorentz force

To have a complete description of the electromagnetic phenomena we must add to the Maxwell's equations the *Lorentz force law*. This law relates electromagnetism with mechanics and it is given by the equation

$$\mathbf{f} = \rho(\mathbf{E} + \mathbf{v} \times \mathbf{B}), \quad (2.11)$$

where \mathbf{f} is the force density (*newton/meter³*), \mathbf{v} is the velocity of the electric charge density (*meter/second*) and \times represents the cross product.

Using the continuity equation (2.5), it can be shown that an electric charge density moving with a velocity \mathbf{v} satisfies

$$\mathbf{J} = \rho \mathbf{v}. \quad (2.12)$$

With this relation we can express the Lorentz force by

$$\mathbf{f} = \rho \mathbf{E} + \mathbf{J} \times \mathbf{B}, \quad (2.13)$$

and the power per unit volume p (*watt/meter³*) delivered by the Lorentz force by

$$p = \mathbf{f} \cdot \mathbf{v} = \rho(\mathbf{E} + \mathbf{v} \times \mathbf{B}) \cdot \mathbf{v} = \mathbf{E} \cdot \mathbf{J}. \quad (2.14)$$

Lorentz force acting on a charged particle

To obtain the electromagnetic force acting on a charged particle we use the electric charge density

$$\rho(\mathbf{r}) = q \delta(\mathbf{r} - \mathbf{r}_0), \quad (2.15)$$

where q is the total electric charge of the particle, $\delta(\mathbf{r} - \mathbf{r}_0)$ is the Dirac's delta function and \mathbf{r}_0 is the position of the particle. With (2.15) and (5.11) we can write

$$\mathbf{F} = q(\mathbf{E} + \mathbf{v} \times \mathbf{B}), \quad (2.16)$$

where \mathbf{F} is the total force (*newton*) acting on the particle.

2.1.2 Constitutive relations

Maxwell's equations cannot be solved until the relations $\mathbf{D} = \mathbf{D}[\mathbf{E}, \mathbf{B}]$ and $\mathbf{H} = \mathbf{H}[\mathbf{E}, \mathbf{B}]$ are known. These connections are called *constitutive relations* and can be expressed as

$$\mathbf{D} = \epsilon_0 \mathbf{E} + \mathbf{P}, \quad (2.17)$$

$$\mathbf{H} = \frac{1}{\mu_0} \mathbf{B} - \mathbf{M}, \quad (2.18)$$

where

\mathbf{P} : polarization (*coulomb/meter²*),

\mathbf{M} : magnetization (*ampere/meter*),

ϵ_0 : vacuum permittivity ($\frac{1}{36\pi} \cdot 10^{-9}$ *farad/meter*),

μ_0 : vacuum permeability ($4\pi \cdot 10^{-7}$ *henry/meter*).

The quantity \mathbf{P} represents the macroscopically averaged electric dipole moment per unit volume of a material medium. The quantity \mathbf{M} represents the macroscopically averaged magnetic dipole moment per unit volume of a material medium. Higher order multipole moments are negligible in most materials, therefore, the knowledge of \mathbf{P} and \mathbf{M} is usually enough to have a complete characterization of a macroscopic media from the standpoint of the electromagnetic theory. \mathbf{P} and \mathbf{M} are functions of the fields, position and time and can not be predicted by the macroscopic electromagnetic theory, but they are accepted as an external information. These relations can be very complex and its determination are left to experiment or to be calculated theoretically from microscopic models.

To complete the description of matter we should add a third constitutive equation, $\mathbf{J} = \mathbf{J}[\mathbf{E}, \mathbf{B}]$, which also has to be known experimentally, or theoretically, and represents the electric current density induced on the media.

Linear isotropic materials

There is a tremendous diversity in the electric and magnetic properties of matter but, in this work, we are only interested in linear isotropic materials. Linear materials are those in which the constitutive relations $\mathbf{D} = \mathbf{D}[\mathbf{E}, \mathbf{B}]$, $\mathbf{H} = \mathbf{H}[\mathbf{E}, \mathbf{B}]$ and $\mathbf{J} = \mathbf{J}[\mathbf{E}, \mathbf{B}]$ are linear. Isotropic materials are those in which \mathbf{D} is related to \mathbf{E} , \mathbf{B} is related to \mathbf{H} , and the induced current density \mathbf{J} is related to \mathbf{E} , with the field direction in each pair aligned. Inside a linear isotropic material (time-invariant and local in space) the constitutive relations have the general form [12]:

$$\mathbf{D}(\mathbf{r}, t) = \int_{-\infty}^{\infty} \epsilon(\mathbf{r}, t') \mathbf{E}(\mathbf{r}, t - t') dt', \quad (2.19)$$

$$\mathbf{B}(\mathbf{r}, t) = \int_{-\infty}^{\infty} \mu(\mathbf{r}, t') \mathbf{H}(\mathbf{r}, t - t') dt', \quad (2.20)$$

$$\mathbf{J}(\mathbf{r}, t) = \int_{-\infty}^{\infty} \sigma(\mathbf{r}, t') \mathbf{E}(\mathbf{r}, t - t') dt', \quad (2.21)$$

where ϵ , μ and σ are scalar functions denominated

ϵ : electric permittivity (*farad/meter*),

μ : magnetic permeability (*henry/meter*),

σ : electric conductivity (*siemens/meter*).

The assumed time-invariant property reveals a non-instantaneous response of the material to an applied field. This property allows to express the linear constitutive relation by means of a convolution in time. The assumed locality in space property is a valid approximation when the spatial variation of the applied fields has a scale that is large compared with the dimensions involved in the creation of the atomic or molecular polarization. For visible light, or electromagnetic radiation of longer wavelength, it is often permissible to neglect the non-locality in space [42]. For conductors, however, the presence of free charges with macroscopic mean free paths makes this assumption to break down at much lower frequencies. Nevertheless, in this work, it is assumed that the constitutive relation between \mathbf{J} and \mathbf{E} is local in space.

If we apply to (2.19)-(2.21) the Fourier transform defined by

$$F(\omega) = \int_{-\infty}^{\infty} f(t)e^{-i\omega t} dt, \quad (2.22)$$

we obtain, considering the spatial coordinates as parameters, the following equations:

$$\mathbf{D}(\mathbf{r}, \omega) = \epsilon(\mathbf{r}, \omega) \mathbf{E}(\mathbf{r}, \omega), \quad (2.23)$$

$$\mathbf{B}(\mathbf{r}, \omega) = \mu(\mathbf{r}, \omega) \mathbf{H}(\mathbf{r}, \omega), \quad (2.24)$$

$$\mathbf{J}(\mathbf{r}, \omega) = \sigma(\mathbf{r}, \omega) \mathbf{E}(\mathbf{r}, \omega), \quad (2.25)$$

where $\mathbf{D}(\mathbf{r}, \omega)$, $\mathbf{B}(\mathbf{r}, \omega)$, $\mathbf{J}(\mathbf{r}, \omega)$, $\mathbf{E}(\mathbf{r}, \omega)$ and $\mathbf{H}(\mathbf{r}, \omega)$ are the Fourier transform in time of $\mathbf{D}(\mathbf{r}, t)$, $\mathbf{B}(\mathbf{r}, t)$, $\mathbf{J}(\mathbf{r}, t)$, $\mathbf{E}(\mathbf{r}, t)$ and $\mathbf{H}(\mathbf{r}, t)$, respectively. Also, $\epsilon(\mathbf{r}, \omega)$, $\mu(\mathbf{r}, \omega)$ and $\sigma(\mathbf{r}, \omega)$ are the Fourier transform in time of $\epsilon(\mathbf{r}, t)$, $\mu(\mathbf{r}, t)$ and $\sigma(\mathbf{r}, t)$, respectively. A linear isotropic material is completely characterized, from the standpoint of the macroscopic electromagnetic theory, when ϵ , μ and σ are known, either in time domain or in frequency domain.

2.2 Potentials

Using Helmholtz's theorem and the equations (2.4) and (2.3) it can be shown that there exist a scalar function Φ , called the electric potential, and a vectorial function \mathbf{A} , called magnetic vector potential, such as

$$\mathbf{B} = \nabla \times \mathbf{A}, \quad (2.26)$$

$$\mathbf{E} = -\nabla\Phi - \frac{\partial\mathbf{A}}{\partial t}. \quad (2.27)$$

If we replace the above equations into (2.1) and (2.2), we obtain

$$\nabla^2\Phi + \frac{\partial}{\partial t}\nabla\cdot\mathbf{A} = -\frac{1}{\epsilon_0}(\rho - \nabla\cdot\mathbf{P}), \quad (2.28)$$

$$\nabla^2\mathbf{A} - \mu_0\epsilon_0\frac{\partial^2\mathbf{A}}{\partial t^2} - \nabla\left(\nabla\cdot\mathbf{A} + \mu_0\epsilon_0\frac{\partial\Phi}{\partial t}\right) = -\mu_0\left(\mathbf{J} + \nabla\times\mathbf{M} + \frac{\partial\mathbf{P}}{\partial t}\right), \quad (2.29)$$

where we have taken into account the general expressions for the constitutive relations (2.17) and (2.18). The operator ∇^2 , when applied to a scalar function in a cartesian coordinate system, is defined by

$$\nabla^2\Phi = \frac{\partial^2\Phi}{\partial x^2} + \frac{\partial^2\Phi}{\partial y^2} + \frac{\partial^2\Phi}{\partial z^2} \quad (2.30)$$

and, when it is applied to a vectorial function in a cartesian coordinate system, is defined by

$$\nabla^2\mathbf{A} = \nabla^2A_x\hat{\mathbf{x}} + \nabla^2A_y\hat{\mathbf{y}} + \nabla^2A_z\hat{\mathbf{z}}. \quad (2.31)$$

The equations (2.28) and (2.29) plus the definitions (2.26) and (2.27) are a set of equations totally equivalent to the set (2.1)-(2.4). If we are able to find a solution of (2.28) and (2.29) then, the fields \mathbf{E} and \mathbf{B} obtained with (2.26) and (2.27), will satisfy automatically all the Maxwell's equations (2.1)-(2.4).

There are different choices of \mathbf{A} and Φ which give the same \mathbf{E} and \mathbf{B} . In fact, if χ is an arbitrary scalar function, any potential of the form

$$\mathbf{A}^+ = \mathbf{A} + \nabla\chi, \quad (2.32)$$

$$\Phi^+ = \Phi - \frac{\partial\chi}{\partial t}, \quad (2.33)$$

will give the same fields \mathbf{E} and \mathbf{B} . This happens because any scalar function χ satisfy

$$\nabla\times(\nabla\chi) = 0, \quad (2.34)$$

where the operator ∇ represents a gradient which, in a cartesian coordinate system, is defined by

$$\nabla\chi = \frac{\partial\chi}{\partial x}\hat{\mathbf{x}} + \frac{\partial\chi}{\partial y}\hat{\mathbf{y}} + \frac{\partial\chi}{\partial z}\hat{\mathbf{z}}. \quad (2.35)$$

To have a unique solution in (2.28) and (2.29) we must impose an extra condition over \mathbf{A} and Φ . This extra condition is called the *gauge* and there are several options. The most used gauge conditions are the *Coulomb gauge*

$$\nabla\cdot\mathbf{A} = 0 \quad (2.36)$$

and the *Lorenz gauge* [5, 70]

$$\nabla\cdot\mathbf{A} + \mu_0\epsilon_0\frac{\partial\Phi}{\partial t} = 0. \quad (2.37)$$

In some situations, thanks to the gauge freedom, a suitable choice of \mathbf{A} and Φ can simplify equations (2.28) and (2.29) and make them easier to solve than the Maxwell's equations (2.1)-(2.4) themselves.

2.3 Time-harmonic Maxwell's equations

In this work we are mainly interested in electromagnetic fields with a sinusoidal time dependence and in a steady-state condition. These fields are called *time-harmonic* and, although a pure monochromatic time-harmonic steady-state electromagnetic field is a mathematical idealization, this assumption is a good approximation in most of the situations we can find in microwave engineering, antenna design or scattering problems. Time-harmonic fields are properly represented in *phasor notation*:

$$\mathbf{E}(\mathbf{r}, t) = \text{Real} [\mathbf{E}_c(\mathbf{r})e^{-i\omega t}], \quad (2.38)$$

$$\mathbf{D}(\mathbf{r}, t) = \text{Real} [\mathbf{D}_c(\mathbf{r})e^{-i\omega t}], \quad (2.39)$$

$$\mathbf{B}(\mathbf{r}, t) = \text{Real} [\mathbf{B}_c(\mathbf{r})e^{-i\omega t}], \quad (2.40)$$

$$\mathbf{H}(\mathbf{r}, t) = \text{Real} [\mathbf{H}_c(\mathbf{r})e^{-i\omega t}], \quad (2.41)$$

where $i = \sqrt{-1}$ is the imaginary unit, $e^{-i\omega t} = \cos(\omega t) - i \sin(\omega t)$ is the Euler's formula modified by a sign, ω is a positive real number ($\omega \in \mathbb{R}$ and $\omega > 0$), $\text{Real}[\cdot]$ denotes the real part of the expression in brackets and $\mathbf{E}_c(\mathbf{r})$, $\mathbf{D}_c(\mathbf{r})$, $\mathbf{B}_c(\mathbf{r})$ and $\mathbf{H}_c(\mathbf{r})$ are vector complex functions that only depend on position. Other authors choose a time dependence of $e^{i\omega t}$. Of course, the choice is arbitrary, and provided it is used consistently, produces no difficulties. It also assumed a sinusoidal time dependence for the sources which, in phasor notation, are represent as

$$\mathbf{J}(\mathbf{r}, t) = \text{Real} [\mathbf{J}_c(\mathbf{r})e^{-i\omega t}], \quad (2.42)$$

$$\rho(\mathbf{r}, t) = \text{Real} [\rho_c(\mathbf{r})e^{-i\omega t}]. \quad (2.43)$$

If the expressions (2.38)-(2.43) are substituted into equations (2.1)-(2.4) it is obtained the so-called *time-harmonic Maxwell's equations*:

$$\nabla \cdot \mathbf{D}_c(\mathbf{r}) = \rho_c(\mathbf{r}), \quad (2.44)$$

$$\nabla \times \mathbf{H}_c(\mathbf{r}) + i\omega \mathbf{D}_c(\mathbf{r}) = \mathbf{J}_c(\mathbf{r}), \quad (2.45)$$

$$\nabla \times \mathbf{E}_c(\mathbf{r}) - i\omega \mathbf{B}_c(\mathbf{r}) = 0, \quad (2.46)$$

$$\nabla \cdot \mathbf{B}_c(\mathbf{r}) = 0. \quad (2.47)$$

To reach these equations we use the fact that for an arbitrary complex function $F_c = F_r + iF_i$ is satisfied

$$\text{Real} [F_c e^{-i\omega t}] = 0 \quad \forall t \Leftrightarrow F_r = 0, F_i = 0 \quad (2.48)$$

and

$$\frac{\partial}{\partial t} (F_c e^{-i\omega t}) = -i\omega F_c e^{-i\omega t}. \quad (2.49)$$

Observing the expressions (2.44)-(2.47) we see that an obvious benefit of the phasor notation is that we can manipulate field quantities without involving the sinusoidal time dependence. Only

vector complex functions which depend exclusively on the position are present in the time-harmonic Maxwell's equations. When the calculations are complete, we can return to the physical solution in time domain using

$$\mathbf{F}(\mathbf{r}, t) = \text{Real} [(\mathbf{F}_r(\mathbf{r}) + i \mathbf{F}_i(\mathbf{r}))e^{-i\omega t}] = \mathbf{F}_r(\mathbf{r}) \cos(\omega t) + \mathbf{F}_i(\mathbf{r}) \sin(\omega t), \quad (2.50)$$

where \mathbf{F} is any electromagnetic field. Another benefit of the phasor notation is that we can find easily the time average of the dot and cross product of two quantities. This is often of interest when dealing with power and energy. The time average of the dot and cross product of the quantities $\mathbf{F}(\mathbf{r}, t) = \text{Real} [\mathbf{F}_c(\mathbf{r})e^{-i\omega t}]$ and $\mathbf{G}(\mathbf{r}, t) = \text{Real} [\mathbf{G}_c(\mathbf{r})e^{-i\omega t}]$ can be calculated as

$$\langle \mathbf{F}(\mathbf{r}, t) \cdot \mathbf{G}(\mathbf{r}, t) \rangle = \frac{1}{T} \int_0^T \mathbf{F}(\mathbf{r}, t) \cdot \mathbf{G}(\mathbf{r}, t) dt = \frac{1}{2} \text{Real} [\mathbf{F}_c(\mathbf{r}) \cdot \bar{\mathbf{G}}_c(\mathbf{r})], \quad (2.51)$$

$$\langle \mathbf{F}(\mathbf{r}, t) \times \mathbf{G}(\mathbf{r}, t) \rangle = \frac{1}{T} \int_0^T \mathbf{F}(\mathbf{r}, t) \times \mathbf{G}(\mathbf{r}, t) dt = \frac{1}{2} \text{Real} [\mathbf{F}_c(\mathbf{r}) \times \bar{\mathbf{G}}_c(\mathbf{r})], \quad (2.52)$$

being $\bar{\mathbf{G}}_c$ the complex conjugate of \mathbf{G}_c and $T = 2\pi/\omega$ the period. For the specific case where $\mathbf{F}_c = \mathbf{G}_c$ we have

$$\langle \mathbf{F}(\mathbf{r}, t) \cdot \mathbf{F}(\mathbf{r}, t) \rangle = \langle |\mathbf{F}(\mathbf{r}, t)|^2 \rangle = \frac{1}{2} \mathbf{F}_c(\mathbf{r}) \cdot \bar{\mathbf{F}}_c(\mathbf{r}) = \frac{1}{2} |\mathbf{F}_c(\mathbf{r})|^2. \quad (2.53)$$

2.3.1 Time-harmonic Maxwell's equations in linear isotropic media

Inside a linear isotropic material (time-invariant and local in space) the constitutive relations have the general form given in (2.19)-(2.21). If we assume the presence of time-harmonic electromagnetic fields and replace expressions (2.38)-(2.41) in equations (2.19)-(2.21), we obtain

$$\mathbf{D}_c(\mathbf{r}) = \epsilon_c(\mathbf{r}) \mathbf{E}_c(\mathbf{r}), \quad (2.54)$$

$$\mathbf{B}_c(\mathbf{r}) = \mu_c(\mathbf{r}) \mathbf{H}_c(\mathbf{r}), \quad (2.55)$$

$$\mathbf{J}_c(\mathbf{r}) = \sigma_c(\mathbf{r}) \mathbf{E}_c(\mathbf{r}), \quad (2.56)$$

where \mathbf{E}_c , \mathbf{D}_c , \mathbf{B}_c and \mathbf{H}_c are the complex valued vectorial functions defined in (2.38)-(2.41) and ϵ_c , μ_c and σ_c are the complex conjugate of the Fourier transform in time of the functions $\epsilon(\mathbf{r}, t)$, $\mu(\mathbf{r}, t)$ and $\sigma(\mathbf{r}, t)$ defined in (2.19)-(2.21). In other words, if $\epsilon(\mathbf{r}, \omega)$, $\mu(\mathbf{r}, \omega)$ and $\sigma(\mathbf{r}, \omega)$ are the functions given in (2.23)-(2.25) and $\bar{\epsilon}(\mathbf{r}, \omega)$, $\bar{\mu}(\mathbf{r}, \omega)$ and $\bar{\sigma}(\mathbf{r}, \omega)$ are its complex conjugates, then

$$\epsilon_c = \bar{\epsilon}(\mathbf{r}, \omega), \quad (2.57)$$

$$\mu_c = \bar{\mu}(\mathbf{r}, \omega), \quad (2.58)$$

$$\sigma_c = \bar{\sigma}(\mathbf{r}, \omega), \quad (2.59)$$

where ω is the frequency at which the fields are oscillating. Since the response of materials to alternating fields is characterized by a complex value, we can separate its real and imaginary parts

in the following way:

$$\epsilon_c = \epsilon' + i\epsilon'', \quad (2.60)$$

$$\mu_c = \mu' + i\mu'', \quad (2.61)$$

$$\sigma_c = \sigma' + i\sigma''. \quad (2.62)$$

The imaginary parts ϵ'' and μ'' and the real part σ' accounts for the dissipation (or loss) of energy within a medium. The real parts ϵ' and μ' and the imaginary part σ'' are related to the stored energy within the medium. For the frequencies of interest in this work ($\omega < 100 \text{ GHz}$), we can consider the imaginary part of the conductivity σ'' as been essentially zero [42].

If we substitute (2.54)-(2.56) into (2.44)-(2.47) we obtain the time-harmonic Maxwell's equations for linear isotropic media:

$$\nabla \cdot (\epsilon_c \mathbf{E}_c) = \rho_c, \quad (2.63)$$

$$\nabla \times \mathbf{H}_c + i\omega\epsilon_c \mathbf{E}_c = \mathbf{J}_c, \quad (2.64)$$

$$\nabla \times \mathbf{E}_c - i\omega\mu_c \mathbf{H}_c = 0, \quad (2.65)$$

$$\nabla \cdot (\mu_c \mathbf{H}_c) = 0, \quad (2.66)$$

where \mathbf{E}_c , \mathbf{H}_c , \mathbf{J}_c , ρ_c , ϵ_c and μ_c are complex valued functions that only depend on position. The term \mathbf{J}_c in (2.64) includes all the *free* current densities which are present in the problem domain. By free current densities we mean all the currents densities except those produced by the polarization and magnetization of the material. The currents densities produced by the polarization and magnetization of the material are implicit in ϵ_c and μ_c . Free current densities are, for instance, the diffusion of charged particles, the induced eddy currents in conductive materials, the impressed currents that are independent of the fields, etc. Hence, we can write

$$\mathbf{J}_c = \sigma_c \mathbf{E}_c + \mathbf{J}_c^{imp}, \quad (2.67)$$

where \mathbf{J}_c^{imp} represents all the free current densities except those induced by the electric field in materials with conductivity. Substituting (2.67) into (2.64) gives

$$\nabla \times \mathbf{H}_c + i\omega \left(\epsilon_c + i \frac{\sigma_c}{\omega} \right) \mathbf{E}_c = \mathbf{J}_c^{imp}. \quad (2.68)$$

If we apply the divergence to (2.68) and recall (2.6), we have

$$\nabla \cdot (\epsilon_c \mathbf{E}_c) = \rho_c^{imp}, \quad (2.69)$$

$$\nabla \times \mathbf{H}_c + i\omega\epsilon_c \mathbf{E}_c = \mathbf{J}_c^{imp}, \quad (2.70)$$

$$\nabla \times \mathbf{E}_c - i\omega\mu_c \mathbf{H}_c = 0, \quad (2.71)$$

$$\nabla \cdot (\mu_c \mathbf{H}_c) = 0, \quad (2.72)$$

where

$$\varepsilon_c = \epsilon_c + i \frac{\sigma_c}{\omega} = \epsilon' - \frac{\sigma''}{\omega} + i \left(\epsilon'' + \frac{\sigma'}{\omega} \right) \quad (2.73)$$

and

$$\rho_c^{imp} = \frac{1}{i\omega} \nabla \cdot \mathbf{J}_c^{imp}. \quad (2.74)$$

In equations (2.69)-(2.72) the effect of the induced currents is included in ε_c . On the other hand, in the equivalent set of equations (2.63)-(2.66), the effect of the induced currents must be detailed explicitly as it is shown in (2.67).

2.4 Fields at the interface between two media

When solving electromagnetic problems we usually find that different materials are present in the domain of study. It is expected that these materials will have different electromagnetic properties and that these properties will change continuously in a narrow region between the two media (*transition layer*). This expectation is consistent with the assumption that the physical fields are continuous and have a continuous derivative. However, in general, we are not interested in the specific details of what actually happens in the transition layer. Therefore, it is customary to replace the real situation by an idealized one in which the width of the transition layer tends to zero and becomes a surface. Using Maxwell's equations can be demonstrated that, at this surface, the fields must satisfy

$$\hat{\mathbf{n}} \cdot (\mathbf{D}_1 - \mathbf{D}_2) = \rho_s, \quad (2.75)$$

$$\hat{\mathbf{n}} \times (\mathbf{H}_1 - \mathbf{H}_2) = \mathbf{J}_s, \quad (2.76)$$

$$\hat{\mathbf{n}} \times (\mathbf{E}_1 - \mathbf{E}_2) = 0, \quad (2.77)$$

$$\hat{\mathbf{n}} \cdot (\mathbf{B}_1 - \mathbf{B}_2) = 0, \quad (2.78)$$

where $\hat{\mathbf{n}}$ is the unit normal to the surface S (the idealized transition layer) and it points from region 2 into region 1 (see fig. 2.1). \mathbf{J}_s and ρ_s represent, respectively, a surface current density and a surface electric charge density located at S . The fields \mathbf{E}_1 , \mathbf{D}_1 , \mathbf{H}_1 and \mathbf{B}_1 denotes the limiting values of the fields as S is approached from region 1. Analogously, \mathbf{E}_2 , \mathbf{D}_2 , \mathbf{H}_2 and \mathbf{B}_2 denotes the limiting values of the fields as S is approached from region 2. The expressions (2.75)-(2.78) are useful in solving Maxwell's equations in different adjacent regions and then connecting the solutions to obtain the fields throughout all the space. In the presence of linear isotropic materials and time-harmonic fields and sources we can use equations (2.69)-(2.72) to find that, at the surface

S , the fields must satisfy

$$\hat{\mathbf{n}} \cdot (\varepsilon_{c1} \mathbf{E}_{c1} - \varepsilon_{c2} \mathbf{E}_{c2}) = \rho_{cs}^{imp}, \quad (2.79)$$

$$\hat{\mathbf{n}} \times (\mathbf{H}_{c1} - \mathbf{H}_{c2}) = \mathbf{J}_{cs}^{imp}, \quad (2.80)$$

$$\hat{\mathbf{n}} \times (\mathbf{E}_{c1} - \mathbf{E}_{c2}) = 0, \quad (2.81)$$

$$\hat{\mathbf{n}} \cdot (\mu_{c1} \mathbf{H}_{c1} - \mu_{c2} \mathbf{H}_{c2}) = 0, \quad (2.82)$$

where ε_{c1} and μ_{c1} are the complex permittivity and permeability of the material 1 as it is defined in (2.73) and (2.55). Analogously, ε_{c2} and μ_{c2} are the complex permittivity and permeability of the material 2. The complex vector functions \mathbf{E}_{c1} and \mathbf{H}_{c1} , which are defined in (2.38) and (2.41), denotes the limiting values of the fields as S is approached from region 1. Similarly, \mathbf{E}_{c2} and \mathbf{H}_{c2} denotes the limiting values of the fields as S is approached from region 2. \mathbf{J}_{cs}^{imp} and ρ_{cs}^{imp} , which are defined in (2.67) and (2.74), represent, respectively, an imposed surface current density and an imposed surface electric charge density located at S . Usually \mathbf{J}_{cs}^{imp} and ρ_{cs}^{imp} are zero. In (2.79)-(2.82) it is not necessary to include explicitly the surface charge density and surface current density due to polarization, magnetization and conductivity of the material, because their effects are implicit in ε_c and μ_c .

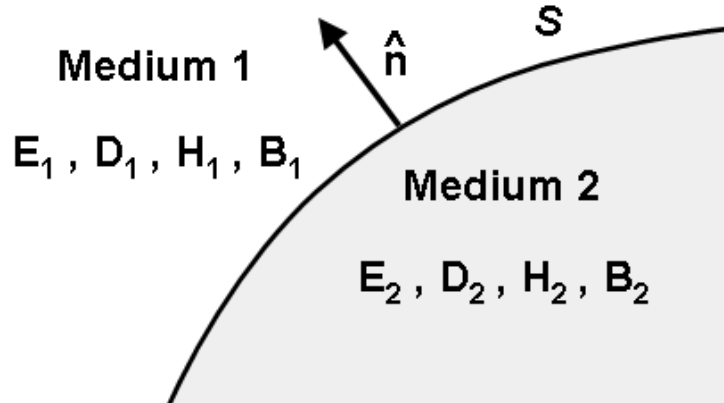


Figure 2.1: Interface between two media.

2.4.1 Perfect electric conductor

A perfect electric conductor (PEC) is a material in which the electric conductivity is considered infinite. A remarkable feature of this idealized material is that, in its interior, any time-harmonic field is zero. This can be seen, heuristically, using equations (2.56) and (2.65) and assuming that, inside a PEC, the fields and the induced currents remain finite. From (2.56), if the conductivity is infinite then \mathbf{E}_c must vanish to have a finite \mathbf{J}_c . On the other hand, from (2.65), if \mathbf{E}_c is zero then

\mathbf{H}_c must also be zero. Equations (2.79)-(2.82) are deduced from (2.69)-(2.72) and they are valid in time-harmonic regimen for linear isotropic materials with finite conductivity. Instead, when the conductivity is infinite, we use (2.63)-(2.66) to obtain

$$\hat{\mathbf{n}} \cdot \epsilon_{c_1} \mathbf{E}_{c_1} = \rho_{cs}, \quad (2.83)$$

$$\hat{\mathbf{n}} \times \mathbf{H}_{c_1} = \mathbf{J}_{cs}, \quad (2.84)$$

$$\hat{\mathbf{n}} \times \mathbf{E}_{c_1} = 0, \quad (2.85)$$

$$\hat{\mathbf{n}} \cdot \mu_{c_1} \mathbf{H}_{c_1} = 0, \quad (2.86)$$

where we have consider in figure 2.1 that the medium 2 is a PEC. \mathbf{J}_{cs} and ρ_{cs} represent, respectively, a free surface current density and a free surface electric charge density confined in S . From (2.85) and (2.86) we can conclude that, outside a PEC, the electric field is normal to the surface S and the magnetic field is tangential to surface S .

2.4.2 Imperfect electric conductor

If the material 2 in figure 2.1 is not a perfect conductor, but allows the fields to penetrate a small distance, then a time-harmonic electric field at S satisfies approximately the relation [97, 98]

$$\frac{1}{\mu_{c_1}} \hat{\mathbf{n}} \times (\nabla \times \mathbf{E}_{c_1}) + \left(i\omega \sqrt{\frac{\epsilon_{c_2}}{\mu_{c_2}}} \right) \hat{\mathbf{n}} \times (\hat{\mathbf{n}} \times \mathbf{E}_{c_1}) = 0. \quad (2.87)$$

Analogously, a time-harmonic magnetic field at S satisfies approximately the relation

$$\frac{1}{\epsilon_{c_1}} \hat{\mathbf{n}} \times (\nabla \times \mathbf{H}_{c_1}) + \left(i\omega \sqrt{\frac{\mu_{c_2}}{\epsilon_{c_2}}} \right) \hat{\mathbf{n}} \times (\hat{\mathbf{n}} \times \mathbf{H}_{c_1}) = 0. \quad (2.88)$$

In the above expressions, \mathbf{E}_{c_1} and \mathbf{H}_{c_1} denotes the limiting values of the fields as S is approached from region 1, ϵ_{c_2} and μ_{c_2} are the complex permittivity and permeability of the imperfect conductor and ϵ_{c_1} and μ_{c_1} are the complex permittivity and permeability of the material outside the imperfect conductor. The relations (2.87) and (2.88) are called the *impedance boundary conditions*.

2.5 Radiation condition

To ensure the uniqueness of the solution of the time-harmonic Maxwell's equations (2.69)-(2.72) on problems where the domain is unbounded, we must specify some boundary condition at infinite [12]. Assuming all the sources and objects at a finite distance from the origin of the coordinate system and immersed in an infinite linear, isotropic, homogeneous and lossless medium (characterize by the real parameters ϵ_r and μ_r), it is required that the time-harmonic electric and magnetic fields satisfy

$$\lim_{r \rightarrow \infty} r [\nabla \times \mathbf{E}_c - i\omega \sqrt{\epsilon_r \mu_r} (\hat{\mathbf{r}} \times \mathbf{E}_c)] = 0, \quad (2.89)$$

$$\lim_{r \rightarrow \infty} r [\nabla \times \mathbf{H}_c - i\omega \sqrt{\epsilon_r \mu_r} (\hat{\mathbf{r}} \times \mathbf{H}_c)] = 0, \quad (2.90)$$

where $r = |\mathbf{r}| = \sqrt{x^2 + y^2 + z^2}$ and $\hat{\mathbf{r}} = \mathbf{r}/|\mathbf{r}|$. Equations (2.89) and (2.90) are the well-known outgoing *Silver-Müller radiation conditions* [63].

2.6 Wave equation

Applying the curl operator to (2.71) and using (2.70) to eliminate \mathbf{H}_c it is obtained the equation

$$\nabla \times \left(\frac{1}{\mu_c} \nabla \times \mathbf{E}_c \right) - \omega^2 \varepsilon_c \mathbf{E}_c = i\omega \mathbf{J}_c^{imp}. \quad (2.91)$$

Applying now the curl operator to (2.70) and using (2.71) to eliminate \mathbf{E}_c it is obtained the equation

$$\nabla \times \left(\frac{1}{\varepsilon_c} \nabla \times \mathbf{H}_c \right) - \omega^2 \mu_c \mathbf{H}_c = \nabla \times \left(\frac{1}{\varepsilon_c} \mathbf{J}_c^{imp} \right). \quad (2.92)$$

These expressions are the *inhomogeneous electromagnetic vector wave equations* for time-harmonic fields in linear isotropic media. Equations (2.91) and (2.92) are very useful because the fields are decoupled, which means that, to calculate \mathbf{E}_c and \mathbf{H}_c , we only need to solve (2.91) and then find \mathbf{H}_c with

$$\mathbf{H}_c = \frac{1}{i\omega \mu_c} (\nabla \times \mathbf{E}_c), \quad (2.93)$$

or, equivalently, we can solve instead the equation (2.92) and then find \mathbf{E}_c with

$$\mathbf{E}_c = \frac{1}{i\omega \varepsilon_c} (\mathbf{J}_c^{imp} - \nabla \times \mathbf{H}_c). \quad (2.94)$$

2.7 Poynting theorem

If we make the dot product of \mathbf{E} with equation (2.2) and the dot product of \mathbf{H} with equation (2.3) and then subtract both expressions, we obtain

$$-\mathbf{E} \cdot \mathbf{J} = \left(\mathbf{E} \cdot \frac{\partial \mathbf{D}}{\partial t} + \mathbf{H} \cdot \frac{\partial \mathbf{B}}{\partial t} \right) + \nabla \cdot (\mathbf{E} \times \mathbf{H}), \quad (2.95)$$

where we have used the identity

$$\nabla \cdot (\mathbf{F} \times \mathbf{G}) = \mathbf{G} \cdot \nabla \times \mathbf{F} - \mathbf{F} \cdot \nabla \times \mathbf{G}. \quad (2.96)$$

If we now integrate (2.95) over a volume V delimited by a surface S and apply the divergence theorem to the last term in the right-hand side, we arrive at the expression

$$-\int_V \mathbf{E} \cdot \mathbf{J} \, dV = \int_V \left(\mathbf{E} \cdot \frac{\partial \mathbf{D}}{\partial t} + \mathbf{H} \cdot \frac{\partial \mathbf{B}}{\partial t} \right) dV + \oint_S (\mathbf{E} \times \mathbf{H}) \cdot d\mathbf{S}, \quad (2.97)$$

which is known as the *Poynting's theorem* [84]. This theorem states the conservation of energy for the electromagnetic fields. The left-hand side of equation (2.97) can be recognized as the power

delivered against the Lorentz force (2.14) or, in other words, as the rate at which energy is supplied to the fields by the currents. The first term of the right-hand side accounts for the the rate at which energy is stored in the electromagnetic fields and for the power dissipated within a material. This dissipation is produced by a time lag between the field applied to the medium and the resulting polarization or magnetization of the atoms. Finally, the last term of the right-hand side represents the power radiated out of the volume V through the surface S .

If the fields are time-harmonic we are usually more interested in the time-average of the expression (2.97). Using (2.51), (2.52) and (2.49), we can express the time-average of (2.97) for time-harmonic fields as

$$\begin{aligned} -\frac{1}{2} \int_V \text{Real} [\mathbf{E}_c \cdot \bar{\mathbf{J}}_c] dV &= -\frac{\omega}{2} \int_V \text{Imag} [\mathbf{E}_c \cdot \bar{\mathbf{D}}_c + \mathbf{H}_c \cdot \bar{\mathbf{B}}_c] dV \\ &+ \frac{1}{2} \oint_S \text{Real} [\mathbf{E}_c \times \bar{\mathbf{H}}_c] \cdot d\mathbf{S}, \end{aligned} \quad (2.98)$$

where $\text{Imag}[\cdot]$ denotes the imaginary part of the expression in brackets. If the materials present are linear and isotropic we can use the definitions (2.53)-(2.56), (2.60)-(2.62) and (2.67), to obtain

$$\begin{aligned} -\frac{1}{2} \int_V \text{Real} [\mathbf{E}_c \cdot \bar{\mathbf{J}}_c^{imp}] dV &= \frac{1}{2} \int_V \sigma' |\mathbf{E}_c|^2 dV \\ &+ \frac{\omega}{2} \int_V (\epsilon'' |\mathbf{E}_c|^2 + \mu'' |\mathbf{H}_c|^2) dV \\ &+ \frac{1}{2} \oint_S \text{Real} [\mathbf{E}_c \times \bar{\mathbf{H}}_c] \cdot d\mathbf{S}, \end{aligned} \quad (2.99)$$

where the left-hand side represents the time-average power delivered by the imposed sources, the first and second term of the right-hand side account for the time-average power dissipated as heat in the volume V due to conductivity, dielectric and magnetic losses and, finally, the last term of the right-hand side, represents the time-average power transmitted through the surface S .

2.8 Summary

In this chapter we have made a review of the equations of the electromagnetic theory that will be used throughout this work. Henceforth, we will omit the subindex c from all the complex valued electromagnetic fields, sources and material properties. Also, as it is mentioned in subsection 2.3.1, we will consider the imaginary part of the electrical conductivity σ'' as been essentially zero and, therefore, $\sigma_c = \sigma' = \sigma$.

Chapter 3

Regularized Maxwell equations and nodal finite elements

This chapter presents an alternative approach to the usual finite element formulation based on edge elements and double-curl Maxwell equations. This alternative approach is based on nodal elements and regularized Maxwell equations. The advantage is that, without adding extra unknowns (such as Lagrange multipliers), it provides spurious-free solutions and well-conditioned matrices. The drawback is that a globally wrong solution is obtained when the electromagnetic field has a singularity in the problem domain. The main objective of this work is to obtain accurate solutions with nodal elements and the regularized formulation, even in the presence of electromagnetic field singularities. The work described in this chapter has been presented in [76, 73, 72] and it is part of the project SANTTRA (Sistema de ANTenas para Transceptores de RAdio), Spanish MCIT PROFIT, ref.: FIT-330210-2006-44, framed in the project SMART (SMart Antennas system for Radio Transceivers), European Commission EUREKA, ref.: PIDEA+ Project n^o04-161. This work has also been partially founded by the project CaRDian (Cálculo de Radiación electromagnética en presencia de Dieléctricos mediante Análisis Numérico), Spanish MCI National R+D Plan 2008-2011, ref.: CIT-370000-2008-10.

3.1 Introduction

The typical approach when solving a general electromagnetic problem with the finite element method (FEM) is to use edge elements and double-curl Maxwell equations. These edge elements, proposed by Nédélec [69], seem to be the answer to most of the drawbacks exhibited by FEM when applied to electromagnetism [92, 44]. With edge elements, spurious-free solutions are obtained, boundary conditions are easier to implement, and the normal discontinuity and tangential continuity between different media are automatically satisfied. In addition, they present a better behavior in nonconvex domains than Lagrangian elements [114]. However, using edge elements with the double-curl formulation has also disadvantages [67, 66]. The most important flaw is the matrices produced, which are ill-conditioned and, in problems with a high number of unknowns, can even be singular [53]. The use of potentials or Lagrange multipliers can improve the con-

ditioning of the matrix [14, 39] or even be necessary [49, 54], but the number of unknowns is increased by the presence of these scalar functions. Therefore, although edge elements present several advantageous features, there can be trouble when trying to solve big problems where the use of direct methods, or good preconditioning, can be limited by computer hardware. Because of this, it would be desirable to explore alternative FEM formulations that provide matrices that are easy to solve by means of iterative solvers.

The alternative approach proposed in this work is based on nodal elements and regularized Maxwell equations [36, 17]. The good point of this proposal is that it provides spurious-free solutions with well-conditioned matrices and, moreover, only the three components of \mathbf{E} or \mathbf{H} are the unknowns; that is, there is no need of extra functions such as Lagrange multipliers or scalar potentials. Furthermore, its integral representation involves a less singular kernel (order 1 instead of 3), which makes the regularized FEM formulation best suited to hybridization with integral numerical techniques [36]. On the other hand, new difficulties arise that were not present in the classical formulation. The main drawback is that if the electromagnetic field has a singularity in the problem domain, a *globally wrong* solution is obtained. Also, boundary conditions and field discontinuities are more laborious to implement. This chapter explains how to overcome these difficulties. The main objective is to demonstrate that accurate solutions can be obtained using nodal elements and the regularized formulation. The comparative performance of the classical *edge-double-curl* formulation versus the *nodal-regularized* formulation presented in this chapter will be the topic of future work.

In the first two sections, the classical double-curl formulation and the regularized Maxwell formulation are exposed, both adapted to electromagnetic problems in frequency domain. The formulations are written to emphasize their differences in the differential and weak form and also in the boundary conditions. This method can use \mathbf{E} or \mathbf{H} as the primary unknown but, in this work, for simplicity, only the \mathbf{E} field is used. The next section explains how to deal with field discontinuities and nodal elements, not only how to solve problems with a discontinuity surface present, but also how to work with the intersection of three or more different materials. Following that, the problem of the singularities is described: why it is produced and how to overcome this critical question. Finally, in the last sections, several examples in two and three dimensions are shown to check the accuracy of the method.

3.2 Double-curl Maxwell equations and edge elements

The generic problem to be solved is to find the electric field \mathbf{E} in a domain Ω with boundary $\partial\Omega$ produced by a divergence-free source \mathbf{J} driven at a frequency ω . The equation that \mathbf{E} satisfies in Ω , the so-called *double-curl Maxwell equation*, is

$$\nabla \times \left(\frac{1}{\mu} \nabla \times \mathbf{E} \right) - \omega^2 \varepsilon \mathbf{E} = i\omega \mathbf{J}, \quad (3.1)$$

where μ and ε are, respectively, the complex magnetic permeability and the complex electric permittivity defined in section 2.3.1. On the surface of a perfect electric conductor (PEC), the field \mathbf{E} satisfies the boundary condition

$$\hat{\mathbf{n}} \times \mathbf{E} = 0. \quad (3.2)$$

On the surface of a perfect magnetic conductor (PMC), the field \mathbf{E} satisfies the boundary condition

$$\hat{\mathbf{n}} \times \nabla \times \mathbf{E} = 0. \quad (3.3)$$

In an open domain, the Silver-Müller radiation boundary condition must be added at infinity:

$$\lim_{r \rightarrow \infty} \oint_{\partial\Omega_r} \|\hat{\mathbf{n}} \times \nabla \times \mathbf{E} + (i\omega\sqrt{\epsilon_0\mu_0}) \mathbf{E}\|^2 = 0. \quad (3.4)$$

In a waveguide port, the boundary conditions will be adapted to take into account the specific modes of the waveguide. For instance, in a rectangular waveguide port with only the fundamental mode TE₁₀ propagating,

$$\hat{\mathbf{n}} \times \nabla \times \mathbf{E} = \gamma (\hat{\mathbf{n}} \times \hat{\mathbf{n}} \times \mathbf{E}) + \mathbf{U} \quad (3.5)$$

holds, where γ is the propagation constant of the fundamental mode and

$$\begin{aligned} \mathbf{U} &= -2\gamma (\hat{\mathbf{n}} \times \hat{\mathbf{n}} \times \mathbf{E}_{10}), \\ \mathbf{U} &= 0 \end{aligned} \quad (3.6)$$

for the input and the output port, respectively [44]. The field \mathbf{E}_{10} is the incident mode TE₁₀ imposed in the input port. The boundary condition (3.5) can also be adapted to represent the behavior of \mathbf{E} on the surface of an imperfect conductor (see section 2.4.2) or to approximate the Silver-Müller radiation boundary condition (3.4) with the first order absorbing boundary condition (1st ABC), which is

$$\hat{\mathbf{n}} \times \nabla \times \mathbf{E} = i\omega\sqrt{\epsilon_0\mu_0} (\hat{\mathbf{n}} \times \hat{\mathbf{n}} \times \mathbf{E}). \quad (3.7)$$

The above set of equations can be solved using an equivalent weak formulation, that is, if

$$\mathbf{H}_0(\mathbf{curl}; \Omega) := \{ \mathbf{F} \in \mathbf{L}^2(\Omega) \mid \nabla \times \mathbf{F} \in \mathbf{L}^2(\Omega), \hat{\mathbf{n}} \times \mathbf{F} = 0 \text{ in PEC} \} \quad (3.8)$$

is defined, solving equation (3.1) is equivalent to finding $\mathbf{E} \in \mathbf{H}_0(\mathbf{curl}; \Omega)$ such that $\forall \mathbf{F} \in \mathbf{H}_0(\mathbf{curl}; \Omega)$ holds:

$$\int_{\Omega} \frac{1}{\mu} (\nabla \times \mathbf{E}) \cdot (\nabla \times \bar{\mathbf{F}}) - \omega^2 \int_{\Omega} \epsilon \mathbf{E} \cdot \bar{\mathbf{F}} + \mathbf{B.C.}|_{\partial\Omega} = i\omega \int_{\Omega} \mathbf{J} \cdot \bar{\mathbf{F}}, \quad (3.9)$$

where the bar over the magnitudes denotes its complex conjugate and $\mathbf{B.C.}|_{\partial\Omega}$ is the term that takes into account the radiation boundary conditions or the modes in a waveguide port. Its general expression is

$$\mathbf{B.C.}|_{\partial\Omega} = \int_{\partial\Omega} \frac{1}{\mu} (\hat{\mathbf{n}} \times \nabla \times \mathbf{E}) \cdot \bar{\mathbf{F}}. \quad (3.10)$$

The weak formulation (3.9), discretized with edge elements, is the classical way to use the FEM when applied to electromagnetic field problems. The advantages and disadvantages of this approach were cited in the introduction of this chapter.

3.3 Regularized Maxwell equations and nodal elements

An alternative for solving equation (3.1) is to use an equivalent second-order differential equation, the so-called *regularized Maxwell equation*:

$$\nabla \times \left(\frac{1}{\mu} \nabla \times \mathbf{E} \right) - \bar{\varepsilon} \nabla \cdot \left(\frac{1}{\bar{\varepsilon} \varepsilon \mu} \nabla \cdot (\varepsilon \mathbf{E}) \right) - \omega^2 \varepsilon \mathbf{E} = i\omega \mathbf{J}. \quad (3.11)$$

On the surface of a perfect electric conductor, the PEC boundary condition (3.2) must be extended to take into account the regularization

$$\begin{aligned} \nabla \cdot (\varepsilon \mathbf{E}) &= 0, \\ \hat{\mathbf{n}} \times \mathbf{E} &= 0. \end{aligned} \quad (3.12)$$

On the surface of a perfect magnetic conductor, the PMC boundary condition (3.3) must be also adapted to the regularization

$$\begin{aligned} \hat{\mathbf{n}} \times \nabla \times \mathbf{E} &= 0, \\ \hat{\mathbf{n}} \cdot \mathbf{E} &= 0. \end{aligned} \quad (3.13)$$

In an open domain, the extended Silver-Müller radiation boundary condition is

$$\begin{aligned} \lim_{r \rightarrow \infty} \oint_{\partial\Omega_r} \|\hat{\mathbf{n}} \times \nabla \times \mathbf{E} - i\omega \sqrt{\varepsilon_0 \mu_0} (\hat{\mathbf{n}} \times \hat{\mathbf{n}} \times \mathbf{E})\|^2 &= 0, \\ \lim_{r \rightarrow \infty} \oint_{\partial\Omega_r} |\nabla \cdot \mathbf{E} - i\omega \sqrt{\varepsilon_0 \mu_0} (\hat{\mathbf{n}} \cdot \mathbf{E})|^2 &= 0. \end{aligned} \quad (3.14)$$

If we approximate the extended Silver-Müller radiation boundary condition with the 1st ABC then, instead of (3.7), we have to use:

$$\begin{aligned} \hat{\mathbf{n}} \times \nabla \times \mathbf{E} &= i\omega \sqrt{\varepsilon_0 \mu_0} (\hat{\mathbf{n}} \times \hat{\mathbf{n}} \times \mathbf{E}), \\ \nabla \cdot \mathbf{E} &= i\omega \sqrt{\varepsilon_0 \mu_0} (\hat{\mathbf{n}} \cdot \mathbf{E}). \end{aligned} \quad (3.15)$$

On the surface of a rectangular waveguide port with only the fundamental mode TE₁₀ propagating, the boundary condition (3.5) is now extended to:

$$\begin{aligned} \hat{\mathbf{n}} \times \nabla \times \mathbf{E} &= \gamma (\hat{\mathbf{n}} \times \hat{\mathbf{n}} \times \mathbf{E}) + \mathbf{U}, \\ \hat{\mathbf{n}} \cdot \mathbf{E} &= 0. \end{aligned} \quad (3.16)$$

The above differential equation can be solved using an equivalent weak formulation; that is, if

$$\begin{aligned} \mathbf{H}_0(\mathbf{curl}, \mathbf{div}; \Omega) &:= \{ \mathbf{F} \in \mathbf{L}^2(\Omega) \mid \nabla \times \mathbf{F} \in \mathbf{L}^2(\Omega), \nabla \cdot (\varepsilon \mathbf{F}) \in L^2(\Omega), \\ &\quad \hat{\mathbf{n}} \times \mathbf{F} = 0 \text{ in PEC}, \hat{\mathbf{n}} \cdot \mathbf{F} = 0 \text{ in PMC} \} \end{aligned} \quad (3.17)$$

is defined, solving (3.11) is equivalent to finding $\mathbf{E} \in \mathbf{H}_0(\mathbf{curl}, \mathbf{div}; \Omega)$ such that $\forall \mathbf{F} \in \mathbf{H}_0(\mathbf{curl}, \mathbf{div}; \Omega)$ holds:

$$\begin{aligned} \int_{\Omega} \frac{1}{\mu} (\nabla \times \mathbf{E}) \cdot (\nabla \times \bar{\mathbf{F}}) + \int_{\Omega} \frac{1}{\bar{\varepsilon} \varepsilon \mu} (\nabla \cdot (\varepsilon \mathbf{E})) \cdot (\nabla \cdot (\bar{\varepsilon} \bar{\mathbf{F}})) \\ - \omega^2 \int_{\Omega} \varepsilon \mathbf{E} \cdot \bar{\mathbf{F}} + \mathbf{R.B.C.}|_{\partial\Omega} = i\omega \int_{\Omega} \mathbf{J} \cdot \bar{\mathbf{F}}, \end{aligned} \quad (3.18)$$

where $\mathbf{R.B.C.}|_{\partial\Omega}$ is the term, properly adapted to the regularization, that takes into account the radiation boundary conditions or the modes in a waveguide port. Its general expression is

$$\mathbf{R.B.C.}|_{\partial\Omega} = \int_{\partial\Omega} \frac{1}{\mu} (\hat{\mathbf{n}} \times \nabla \times \mathbf{E}) \cdot \bar{\mathbf{F}} - \int_{\partial\Omega} \frac{1}{\mu} (\nabla \cdot \mathbf{E}) (\hat{\mathbf{n}} \cdot \bar{\mathbf{F}}). \quad (3.19)$$

In [36], the equivalence between the *classical* problem (3.1)-(3.10) and the *regularized* problem (3.11)-(3.19) is demonstrated. The regularized formulation has the characteristics required for an efficient FEM simulation; that is, it calculates spurious-free solutions with \mathbf{E} as the only unknown, and it produces well-conditioned matrices. Nodal elements can be used as the finite element base, being careful to explicitly consider the discontinuities between different media, as explained in the next section.

Although equation (3.18) looks like a penalized method, the regularized formulation has no undetermined constants, and with the help of the extra boundary conditions, the problem is well-posed. It is worth emphasizing the importance of the extension of the boundary conditions in the regularized formulation: if these extra boundary conditions are omitted, the number of iterations needed for an iterative solver to achieve convergence can be severely increased or we can even obtain spurious solutions.

3.4 Nodal elements and field discontinuities

As mentioned in the previous section, nodal elements are used along with the regularized formulation. Due to the fact that these elements impose normal and tangential continuity, the discontinuities between different media must explicitly be considered. To do so, the technique explained in [83] is employed. This technique consists of defining two different nodes (one on each side of the discontinuity) and during the assembly procedure, relate the two nodes as follows:

$$\begin{pmatrix} E_x^+ \\ E_y^+ \\ E_z^+ \end{pmatrix} = \begin{pmatrix} n_x^2 \xi + 1 & n_x^2 n_y^2 \xi & n_x^2 n_z^2 \xi \\ n_x^2 n_y^2 \xi & n_y^2 \xi + 1 & n_y^2 n_z^2 \xi \\ n_x^2 n_z^2 \xi & n_y^2 n_z^2 \xi & n_z^2 \xi + 1 \end{pmatrix} \begin{pmatrix} E_x^- \\ E_y^- \\ E_z^- \end{pmatrix} \quad (3.20)$$

being

$$\xi = \frac{\epsilon^- + i(\sigma^-/\omega)}{\epsilon^+ + i(\sigma^+/\omega)} - 1,$$

$\mathbf{n} = (n_x, n_y, n_z)$ is the unit normal at the surface, and superscripts "+" and "-" denote each side of the discontinuity surface. In this procedure, the node on side "+" is removed from the total linear system with the help of (3.20), and only the unknowns on the side "-" are solved. No extra unknowns are added, and the symmetry of the total FEM matrix is retained if the side "+" is removed using (3.20) and its transpose [7].

Although this technique works well for discontinuity surfaces, a procedure is needed to deal with the intersection of three or more different materials. An attempt was made in [82], but the finite element bases appearing there do not belong to $\mathbf{H}_0(\text{curl}, \text{div}; \Omega)$ and cannot be used to discretize (3.18). The approach here to overcome this setback consists of a simple extension of the

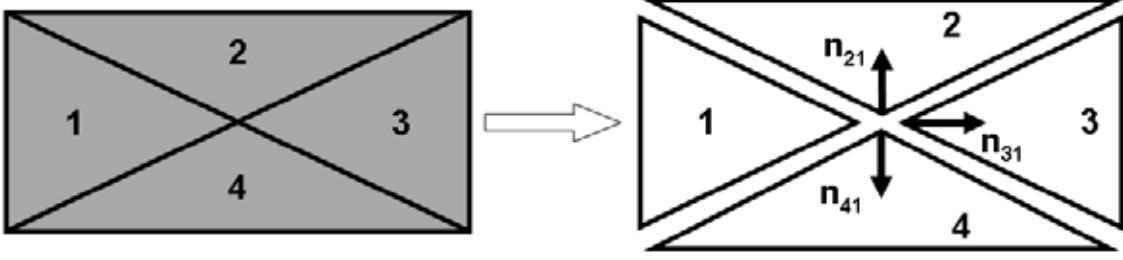


Figure 3.1: Intersection of four different materials. The interface between different materials is considered as two separated surfaces related by equation (3.20). The vectors \mathbf{n}_{21} , \mathbf{n}_{31} and \mathbf{n}_{41} are the unit normal to the surfaces limiting the volume of materials 2, 3, and 4, respectively. In the intersection, equation (3.20) is applied to the pairs 2-1, 3-1, and 4-1.

method presented at the beginning of this section. For instance, in a situation like the one shown in fig. 3.1, four different nodes at the center are defined. One of the nodes defined at the center plays the role of “-” in equation (3.20). In this case, the selected node is in material 1. Then, during the assembly procedure, equation (3.20) is applied to the pairs 2-1, 3-1 and 4-1, with unit normals \mathbf{n}_{21} , \mathbf{n}_{31} and \mathbf{n}_{41} , respectively. Nodes 2, 3, and 4 are removed from the total linear system, and only the unknowns of node 1 are solved. The best choice for the role of “-” is the node that is in the material with the smallest $|\epsilon + i(\sigma/\omega)|$. It was observed that this option always gives the lowest number of iterations when solving the total FEM matrix with iterative solvers.

3.5 Regularized formulation and field singularities

In [36], it is shown that solving (3.18) analytically is equivalent to solving (3.9). However, care must be taken when solving (3.18) numerically with nodal finite elements in a nonconvex polyhedral domain. If \mathbf{V}_h is the vectorial space spanned by K nodal basis functions $N_i(\mathbf{r})$,

$$\mathbf{V}_h := \left\{ \mathbf{u}_h \mid \mathbf{u}_h = \hat{\mathbf{x}} \sum_{i=1}^K c_{x_i} N_i(\mathbf{r}) + \hat{\mathbf{y}} \sum_{i=1}^K c_{y_i} N_i(\mathbf{r}) + \hat{\mathbf{z}} \sum_{i=1}^K c_{z_i} N_i(\mathbf{r}), c_i \in \mathbb{C} \right\}$$

and

$$\mathbf{H}_0^1(\Omega) := \left\{ \mathbf{F} \in \mathbf{L}^2(\Omega) \mid \frac{\partial \mathbf{F}}{\partial x}, \frac{\partial \mathbf{F}}{\partial y}, \frac{\partial \mathbf{F}}{\partial z} \in \mathbf{L}^2(\Omega), \hat{\mathbf{n}} \times \mathbf{F} = 0 \text{ in PEC} \right\},$$

it is clear that \mathbf{V}_h is included in $\mathbf{H}_0^1(\Omega)$. But, for nonconvex polyhedral domains, $\mathbf{H}_0^1(\Omega)$ is strictly included in $\mathbf{H}_0(\mathbf{curl}, \text{div}; \Omega)$ and, moreover, $\mathbf{H}_0^1(\Omega)$ is closed in $\mathbf{H}_0(\mathbf{curl}, \text{div}; \Omega)$ [15, 17]. As a consequence of this theorem, if \mathbf{E} , the analytical solution of (3.18), belongs to $\mathbf{H}_0(\mathbf{curl}, \text{div}; \Omega)$ but not to $\mathbf{H}_0^1(\Omega)$; then, it is impossible to approximate \mathbf{E} using nodal elements. In fact, such an approximation is impossible using any \mathbf{H}^1 -conforming finite element discretization [16]. This situation happens, for instance, when the electric field is singular in the corners or edges of a PEC. In other words, for nonconvex polyhedral domains,

$$\mathbf{V}_h \subseteq \mathbf{H}_0^1(\Omega) \subset \mathbf{H}_0(\mathbf{curl}, \text{div}; \Omega).$$

If the electric field is singular at some point of the domain, the analytical solution \mathbf{E} belongs to $\mathbf{H}_0(\mathbf{curl}, \text{div}; \Omega)$ but not to $\mathbf{H}_0^1(\Omega)$. This means that \mathbf{E} can not be approximated with nodal elements and (3.18), because any approximation of \mathbf{E} , regardless of the element size or the polynomial order used in the discretization, will belong to $\mathbf{H}_0^1(\Omega)$. In fact, what is approximated using (3.18) and nodal elements is the Galerkin projection of \mathbf{E} onto $\mathbf{H}_0^1(\Omega)$, which is, in general, globally different to \mathbf{E} . An example of this behavior is shown in figure 3.2.

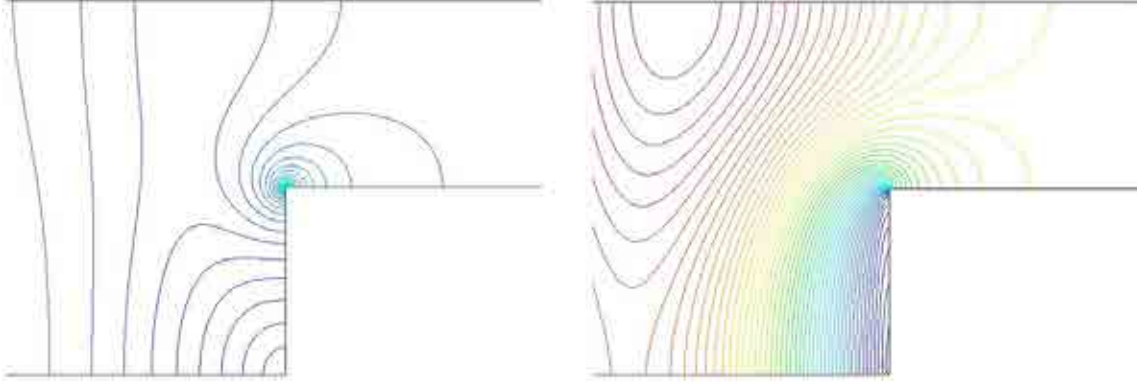


Figure 3.2: Modulus of the electric field in a waveguide step discontinuity. Left: reference solution. Right: same problem solved with the regularized formulation.

A good option to overcome the problem with the singularities in the regularized formulation is to follow the weighted regularized Maxwell equations (WRME) method explained in [17]. There are other possibilities, such as [20, 1] or [8], but the WRME method is more general and robust. In the WRME method, the divergence term of (3.18) is multiplied by a geometry-dependent weight. This weight tends to zero when approaching to a field singularity. To be more specific, the weight τ is

$$\tau := \left(\prod_{\text{corners}} r^{\gamma_c} \right) \cdot \left(\prod_{\text{edges}} \rho^{\gamma_e} \right), \quad (3.21)$$

where r and ρ are the distances from a point in the domain to the corner or edge where the field is singular. The coefficients γ_c and γ_e only depend on the geometry and can be calculated theoretically [17]. The WRME method defines the space

$$\mathbf{X} := \left\{ \mathbf{u} \in \mathbf{H}_0(\mathbf{curl}; \Omega) \mid \tau(\nabla \cdot \mathbf{u}) \in L_{loc}^2(\Omega) \right\},$$

and solves the problem of finding $\mathbf{E} \in \mathbf{X}$ such that $\forall \mathbf{F} \in \mathbf{X}$ holds

$$\begin{aligned} \int_{\Omega} \frac{1}{\mu} (\nabla \times \mathbf{E}) \cdot (\nabla \times \bar{\mathbf{F}}) + \int_{\Omega} \frac{\tau}{\bar{\varepsilon} \varepsilon \mu} (\nabla \cdot (\varepsilon \mathbf{E})) \cdot (\nabla \cdot (\bar{\varepsilon} \bar{\mathbf{F}})) \\ - \omega^2 \int_{\Omega} \varepsilon \mathbf{E} \cdot \bar{\mathbf{F}} + \mathbf{W.R.B.C.}|_{\partial\Omega} = i\omega \int_{\Omega} \mathbf{J} \cdot \bar{\mathbf{F}}, \end{aligned} \quad (3.22)$$

where $\mathbf{W.R.B.C.}|_{\partial\Omega}$ is the term, properly adapted to the weighted regularization, that takes into account the radiation boundary conditions or the modes in a waveguide port. In [17], it is demonstrated that solving (3.22) is equivalent to solving the Maxwell equations and also that $\mathbf{H}_0^1(\Omega)$ is dense in \mathbf{X} . These results imply that nodal elements converge to the right electromagnetic field solution even in the presence of singularities.

The method proposed in this work is a simplification of the WRME method. Instead of (3.21), the divergence term of (3.18) is multiplied by a weight which is equal to zero in the elements near a singularity and equal to one in the rest. The same idea appears in [86] for eddy current problems with the $\mathbf{T} - \Omega$ formulation and also in [46] for magnetostatic problems with the potential \mathbf{A} formulation. It is worth to mention that the WRME method always needs finer meshes and more iterations of the iterative solvers to achieve the same accuracy as the simplified formulation. This was observed for the 2D problems in the next section. No testing of the WRME method for 3D problems was performed.

Henceforth, when a problem is said to be solved with one ungauged layer (UL), it means that only the elements with a node in contact with a singularity have a weight equal to zero. If a problem is said to be solved with 2 ULs, it means that the weight is set to zero in the elements with a node in contact with a singularity and also in the elements that have a node in contact with the elements of the first layer. An equivalent definition is applied for 3 ULs, 4 ULs, and so on. Only the elements in the UL have a weight equal to zero; for the rest, the weight is equal to one. These ULs must be applied in all places where the field is singular. If a singularity point is kept without this treatment, the simulation can give a globally wrong solution. To know the places where the field is singular, analyze the geometry and look for [6]:

- 1) Reentrant corners and edges of PECs.
- 2) Corners and edges of dielectrics.
- 3) Intersection of several dielectrics.

Once these points are located, the number of ULs depends on the size and order of the elements, as shown in the next sections. If, for some reason, very small elements are required around the singularity, the number of ULs must be increased. Not doing so is equivalent to use (3.18) instead of (3.22). To distinguish the simplified formulation from the WRME method, it is called RME-UL (*Regularized Maxwell Equations with Ungauged Layers*).

3.6 Validation examples in two dimensions

This section shows some 2D configurations used to check the accuracy of the RME-UL method. The geometries employed represent four different discontinuities in a parallel-plate waveguide (figures 3.3, 3.7, 3.11 and 3.15). The problems are driven by a current density $\mathbf{J}_y = 1 \text{ A/m}^2$ at a frequency of $\nu = 10 \text{ GHz}$. The walls of the waveguide are PECs. The discontinuous lines at the sides of the geometries symbolize the application of the first-order absorbing boundary condition (1st ABC). The graphs 3.5, 3.6, 3.9, 3.10, 3.13, 3.14, 3.17 and 3.18 show the modulus of the electric field $|\mathbf{E}| = \sqrt{E_x^2 + E_y^2}$ calculated with three different approaches: Reference (reference

solution), RME (regularized Maxwell equations) and RME-UL (regularized Maxwell equations with ungauged layers).

The reference solution $\mathbf{E} = (E_x, E_y)$ is obtained with the method explained in [44, ch.4]. That is, we solve with the FEM and a dense mesh of first order triangular nodal elements the equation

$$\nabla \cdot \left(\frac{1}{\varepsilon} \nabla H_z \right) + \omega^2 \mu H_z = \frac{\partial}{\partial y} \left(\frac{1}{\varepsilon} J_x \right) - \frac{\partial}{\partial x} \left(\frac{1}{\varepsilon} J_y \right), \quad (3.23)$$

with

$$\hat{\mathbf{n}} \cdot \left(\frac{1}{\varepsilon} \nabla H_z \right) = 0 \quad (3.24)$$

in the PEC walls of the waveguide and

$$\hat{\mathbf{n}} \cdot \left(\frac{1}{\varepsilon} \nabla H_z \right) = i\omega \sqrt{\frac{\mu}{\varepsilon}} H_z \quad (3.25)$$

in the discontinuous lines at the sides of the geometries (see figures 3.3, 3.7, 3.11 and 3.15). Once H_z is known, we compute $\mathbf{E} = (E_x, E_y)$ with

$$\mathbf{E} = \frac{i}{\omega \varepsilon} (\nabla \times \mathbf{H} - \mathbf{J}) = \frac{i}{\omega \varepsilon} \left(\frac{\partial H_z}{\partial y} - J_x, -\frac{\partial H_z}{\partial x} + J_y \right). \quad (3.26)$$

In [45] is demonstrated that the numerical solution provided by this approach approximates to the analytical solution for a sufficient dense mesh. In figures 3.4, 3.8, 3.12 and 3.16 is shown the modulus of the electric field calculated with this method.

The RME solution is obtained from (3.18), (3.12) and (6.4) assuming that the z component of the electric field and all the derivatives in the z direction are equal to zero ($E_z = 0$ and $\partial(\cdot)/\partial z = 0$). We used triangular nodal elements from first- to sixth-order and we treat the electric field discontinuities at the material interfaces as it is explained in section 3.4. The unit normals at the nodes placed in the corners are calculated as a geometric average and they are used in (3.20), or in the PEC condition, like in any other node [7]. No special treatment is given to the points where the field is singular.

The RME-UL solution is obtained in the same way that the RME solution but taking into account the field singularities as it is explained in section 3.5. The RME-UL approach was also tested with triangular nodal elements from first- to sixth-order. From third- to sixth-order elements and 1 UL, accurate solutions were obtained even near the singularity. With second-order elements and 3 ULs, correct solutions were also obtained. With first-order elements, it was not possible to obtain accurate solutions even with 6 ULs.

In the graphs of figures 3.5, 3.6, 3.9, 3.10, 3.13, 3.14, 3.17 and 3.18, it can be seen that the reference solution and the RME-UL solution overlap perfectly, even in the neighborhood of the singularity. On the other hand, the RME solution is completely different from the reference solution. This shows graphically the consequences of using (3.18) without taking into account the effect of the singularities.

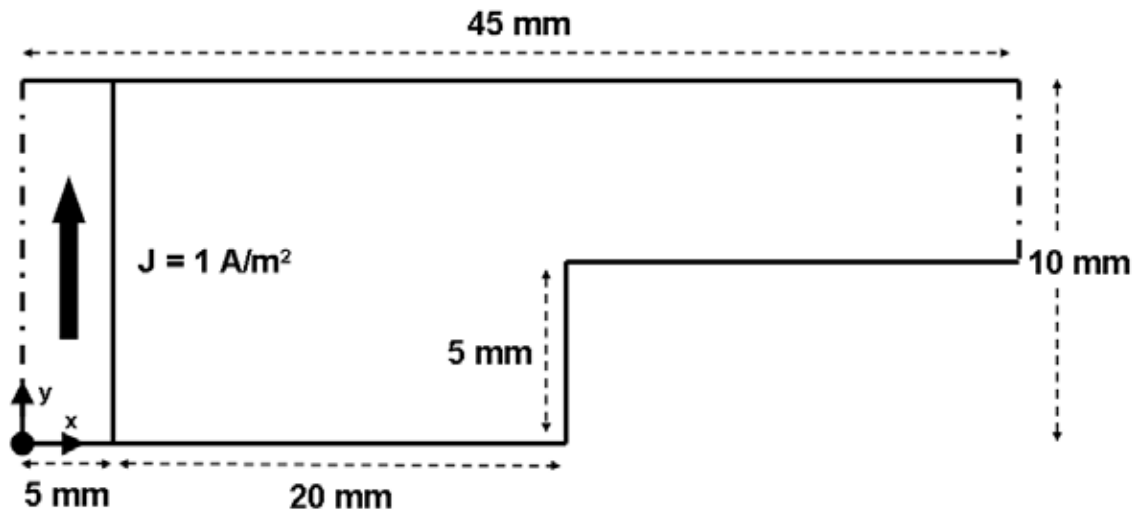


Figure 3.3: Step discontinuity in a parallel-plate waveguide.

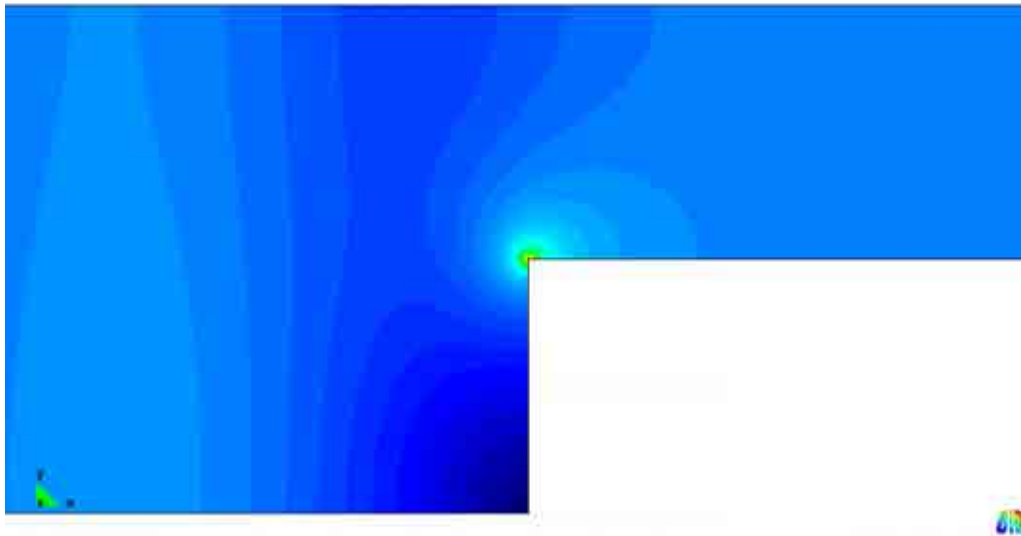


Figure 3.4: Modulus of the electric field in the parallel-plate waveguide step discontinuity of fig. 3.3. Reference solution.

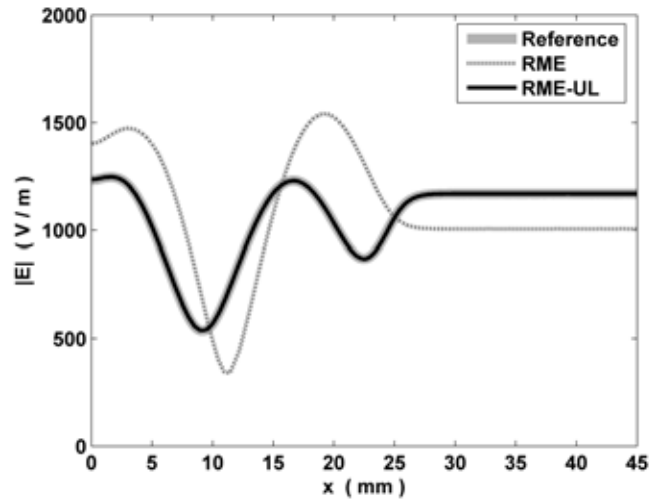


Figure 3.5: Modulus of the electric field along the x -direction at $y = 7.5$ mm in the parallel-plate waveguide configuration of fig. 3.3.

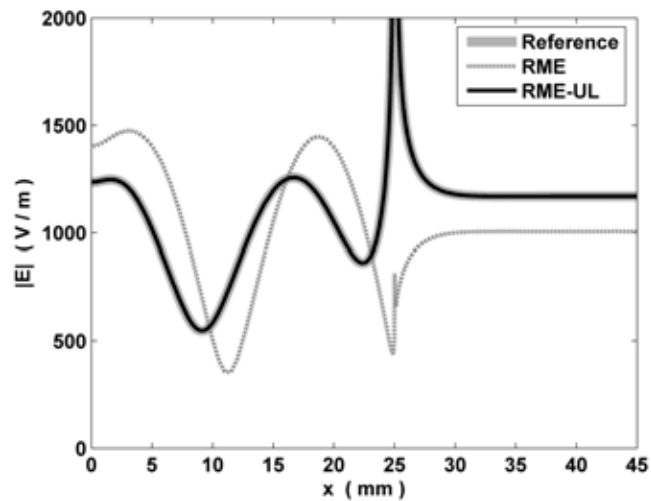


Figure 3.6: Modulus of the electric field along the x -direction at $y = 5$ mm in the parallel-plate waveguide configuration of fig. 3.3.

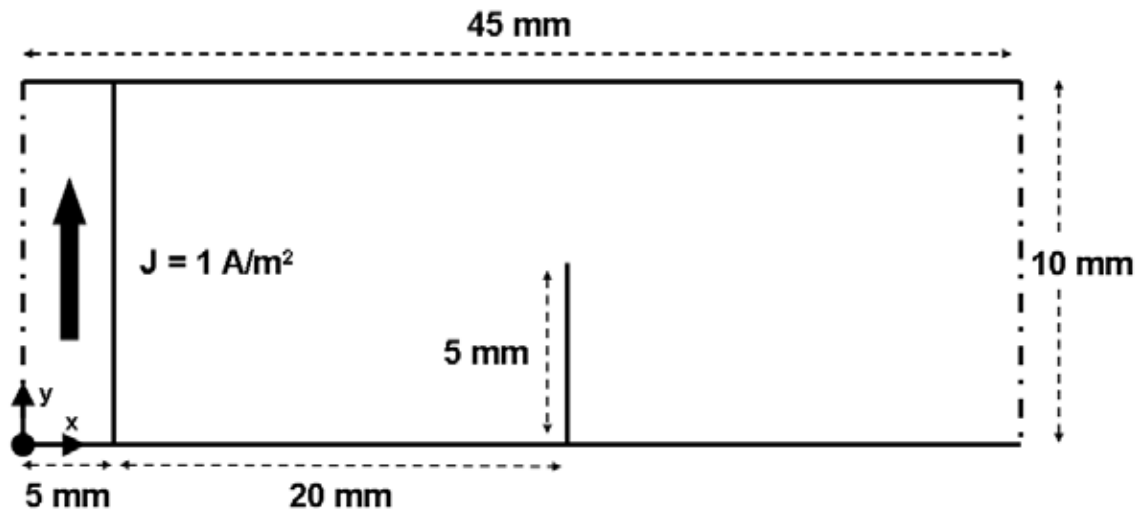


Figure 3.7: Sheet singularity in a parallel-plate waveguide.

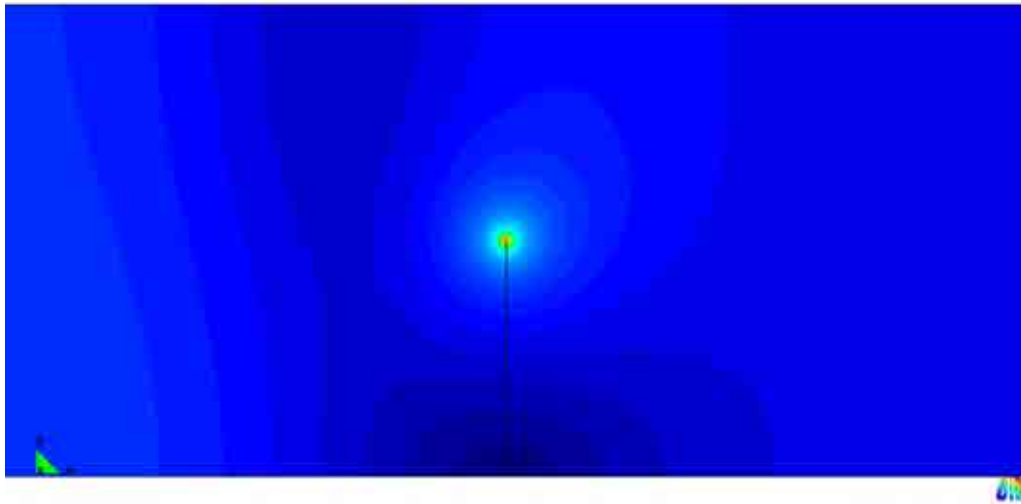


Figure 3.8: Modulus of the electric field in the parallel-plate waveguide configuration of fig. 3.7. Reference solution.

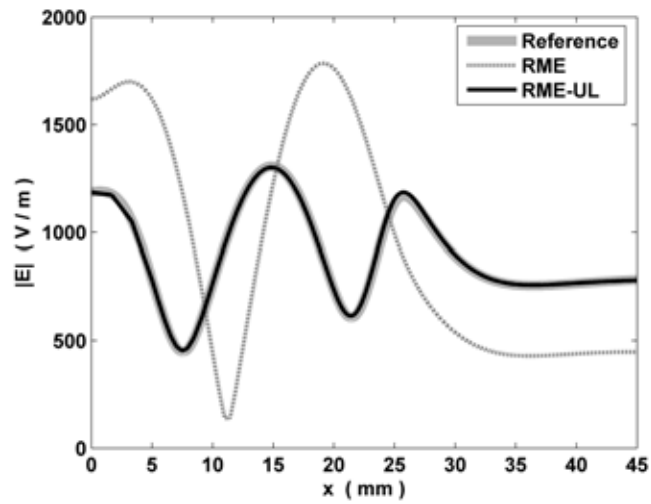


Figure 3.9: Modulus of the electric field along the x-direction at $y = 7.5$ mm in the parallel-plate waveguide configuration of fig. 3.7.

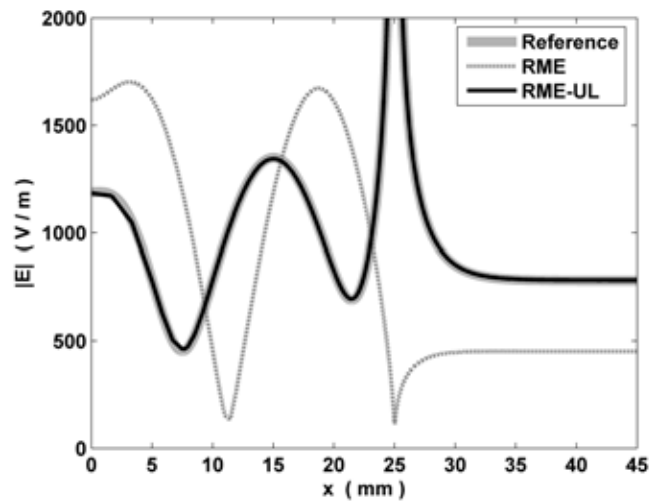


Figure 3.10: Modulus of the electric field along the x-direction at $y = 5$ mm in the parallel-plate waveguide configuration of fig. 3.7.

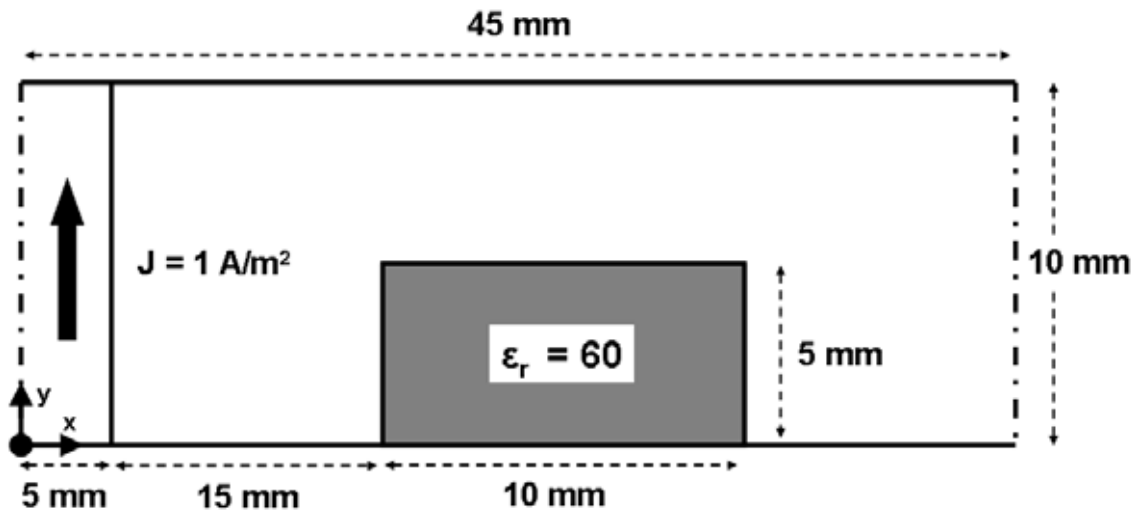


Figure 3.11: Dielectric ($\epsilon = 60\epsilon_0$, $\sigma = 0$ S/m) in a parallel-plate waveguide.

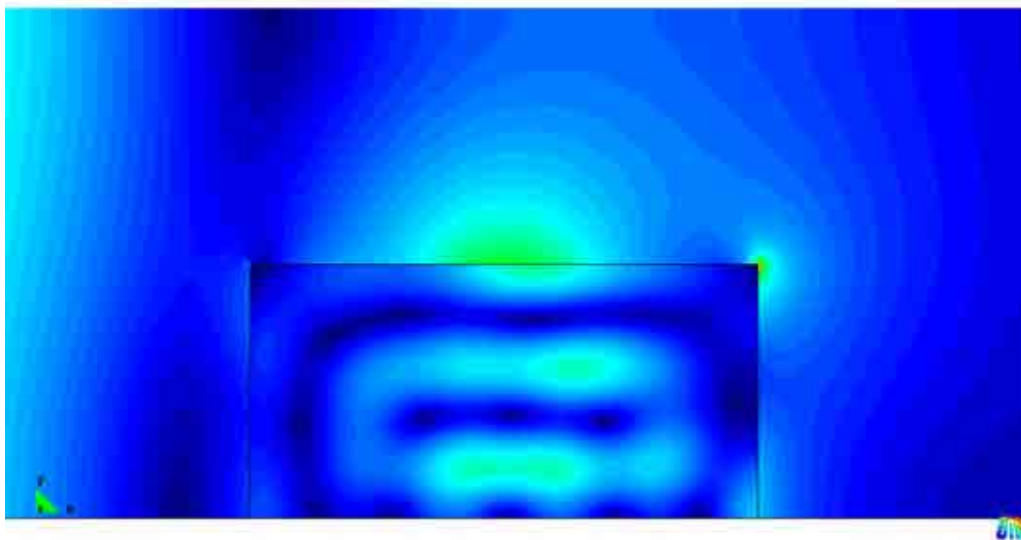


Figure 3.12: Modulus of the electric field in the parallel-plate waveguide configuration of fig. 3.11. Reference solution.

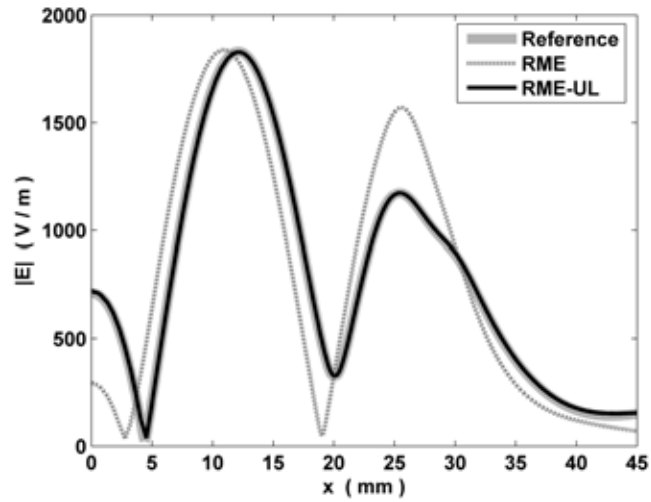


Figure 3.13: Modulus of the electric field along the x -direction at $y = 7.5$ mm in the parallel-plate waveguide configuration of fig. 3.11.

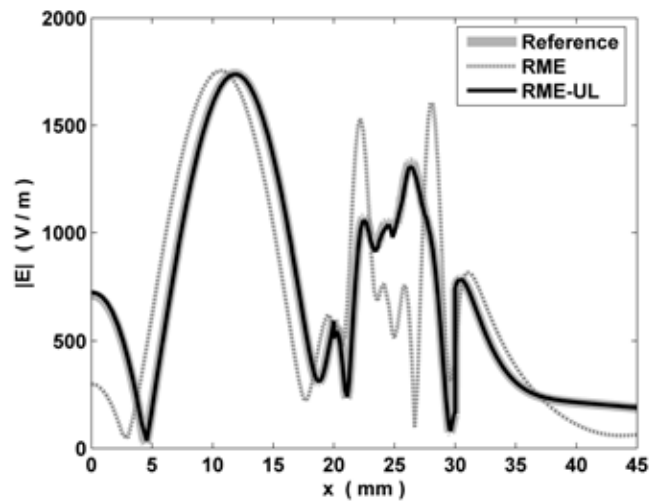


Figure 3.14: Modulus of the electric field along the x -direction at $y = 2.5$ mm in the parallel-plate waveguide configuration of fig. 3.11.

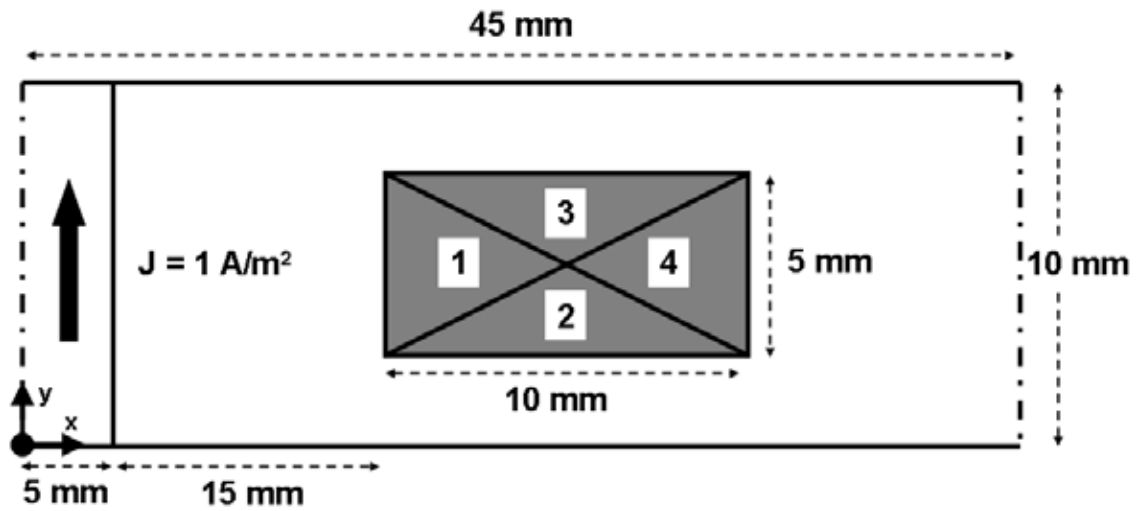


Figure 3.15: Intersection of dielectrics in a parallel-plate waveguide. Material 1: $\epsilon = 5\epsilon_0$, $\sigma = 0$ S/m. Material 2: $\epsilon = 10\epsilon_0$, $\sigma = 0$ S/m. Material 3: $\epsilon = 20\epsilon_0$, $\sigma = 1$ S/m. Material 4: $\epsilon = 30\epsilon_0$, $\sigma = 10$ S/m.

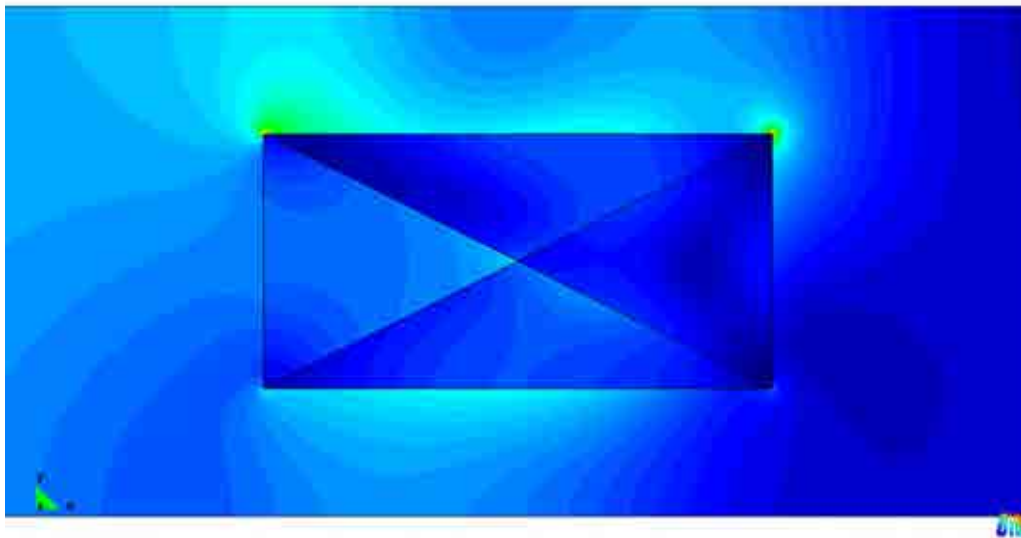


Figure 3.16: Modulus of the electric field in the parallel-plate waveguide configuration of fig. 3.15. Reference solution.

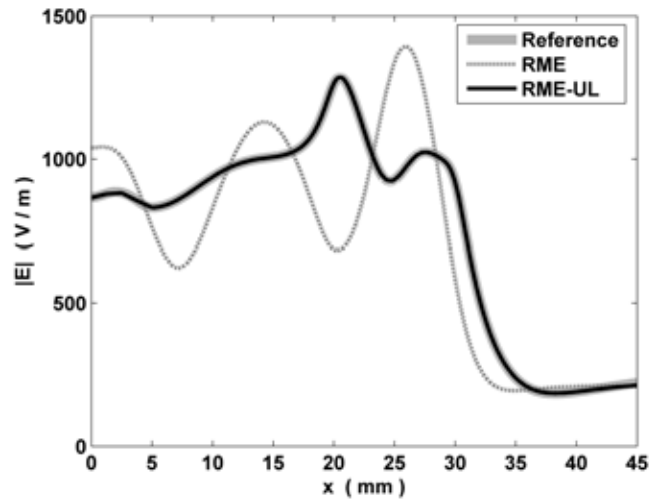


Figure 3.17: Modulus of the electric field along the x -direction at $y = 8.75$ mm in the parallel-plate waveguide configuration of fig. 3.15.

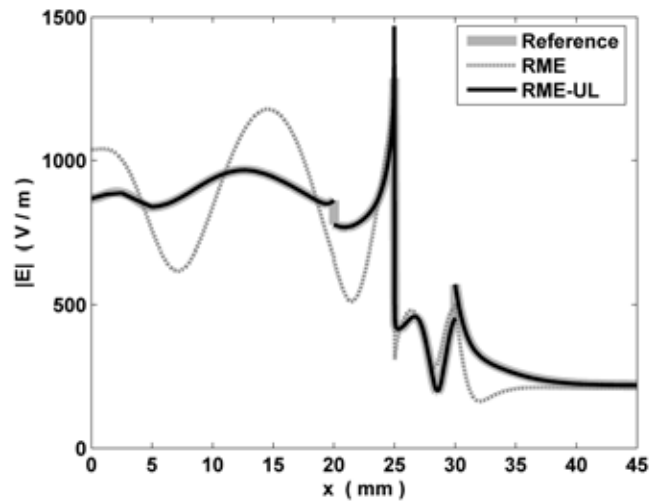


Figure 3.18: Modulus of the electric field along the x -direction at $y = 5$ mm in the parallel-plate waveguide configuration of fig. 3.15.

3.7 Validation examples in three dimensions

This section presents some 3D configurations solved with the RME-UL approach. Figures 3.19, 3.21 and 3.23 display three microwave filters taken from [64], [60] and [48]. We computed the scattering parameters of these microwave filters assuming that only the fundamental mode TE_{10} is propagating in the waveguide ports. We used the RME-UL method with the boundary condition (3.12) in the PEC walls and the condition (3.16) in the waveguide ports. Once the electric field \mathbf{E} was known, the scattering parameter S_{11} was obtained with [92]

$$S_{11} = \frac{\int_{\Gamma_1} (\mathbf{E} \times \mathbf{H}_{10}) \cdot \hat{\mathbf{n}} \, d\Gamma_1}{V_1^{imp}} - 1, \quad (3.27)$$

and the scattering parameter S_{21} with [92]

$$S_{21} = \frac{\int_{\Gamma_2} (\mathbf{E} \times \mathbf{H}_{10}) \cdot \hat{\mathbf{n}} \, d\Gamma_2}{V_1^{imp}}, \quad (3.28)$$

where Γ_1 is the input port, Γ_2 is the output port, \mathbf{H}_{10} is the magnetic field

$$\mathbf{H}_{10} = \frac{1}{i\omega\mu} (\nabla \times \mathbf{E}_{10}), \quad (3.29)$$

and V_1^{imp} is given by the expression

$$V_1^{imp} = \int_{\Gamma_1} (\mathbf{E}_{10} \times \mathbf{H}_{10}) \cdot \hat{\mathbf{n}} \, d\Gamma_1. \quad (3.30)$$

The electric field \mathbf{E}_{10} is the fundamental mode TE_{10} of a rectangular waveguide

$$\mathbf{E}_{10} = -\sqrt{\frac{2i\omega\mu}{ab\gamma}} \sin(k_c x) e^{\gamma z} \hat{\mathbf{y}}, \quad (3.31)$$

where a is the width of the rectangular waveguide, b is its height, $k_c = \pi/a$ and γ is the propagation constant of the mode TE_{10} , which is $\gamma = \pm i\sqrt{k_0^2 - k_c^2}$ when $k_0 > k_c$ and $\gamma = \mp\sqrt{k_c^2 - k_0^2}$ when $k_0 < k_c$. The sign of γ depends on the direction of propagation. We have considered that the x-axis is along the width of the rectangular waveguide, the y-axis is along its height and the z-axis is perpendicular to the xy-plane. For a more detailed information about rectangular waveguides and microwave engineering see [85, 2].

The RME-UL results shown in figures 3.20, 3.22 and 3.24 were obtained with second-order isoparametric tetrahedral nodal finite elements and 3 ULs. The same good results can also be obtained with third-order tetrahedral nodal elements and 1 UL, but the computational cost is higher. We were not able to obtain accurate and robust solutions with first-order elements, no matter the number of ULs employed (it was tested up to 6 ULs). All the examples were solved using a quasi-minimal residual (QMR) iterative solver [28] with a diagonal preconditioner. The convergence of the solver was excellent, proving the well-conditioning of the matrix. It took less than 0.1-0.5% of the total number of unknowns to reach a residual ($\|Ax - b\|/\|b\|$) of less than $1e-4$.

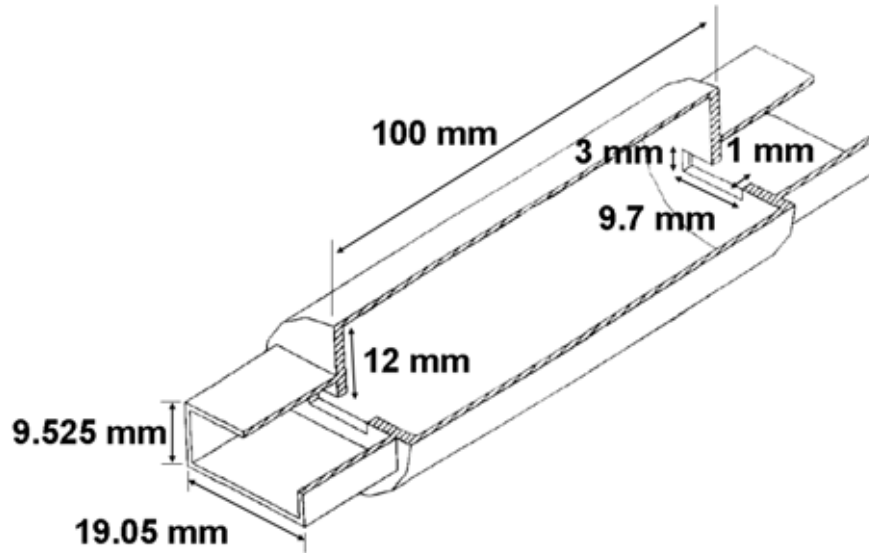


Figure 3.19: Cylindrical cavity filter from [64].

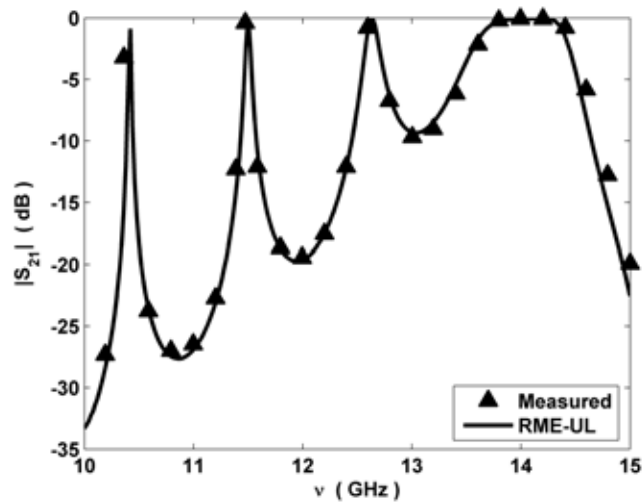


Figure 3.20: Modulus of the transmission coefficient S_{21} of the cylindrical cavity filter shown in fig. 3.19 as a function of the frequency ν . The results obtained with the RME-UL approach are compared with the measurements performed in [64].

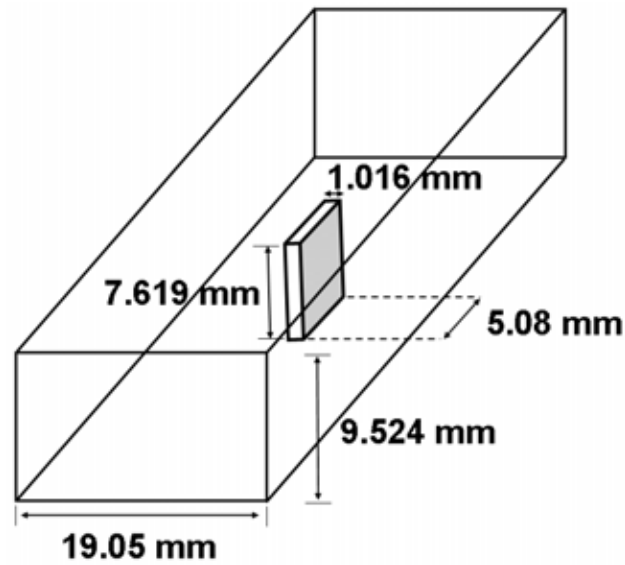


Figure 3.21: Ridge waveguide from [60].

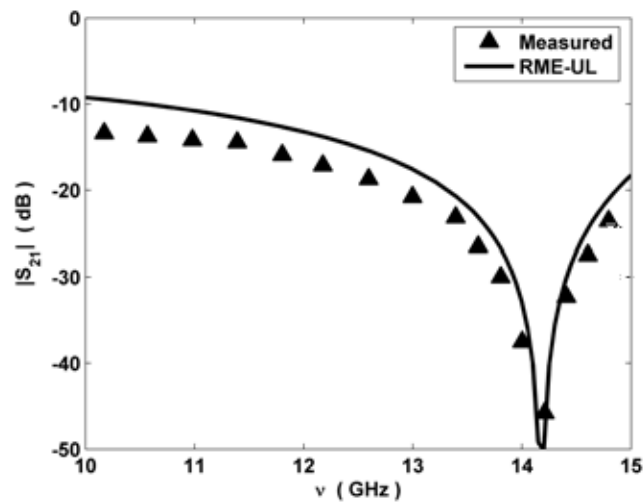


Figure 3.22: Modulus of the transmission coefficient S_{21} of the ridge waveguide shown in fig. 3.21 as a function of the frequency ν . The results obtained with the RME-UL approach are compared with the measurements performed in [60].

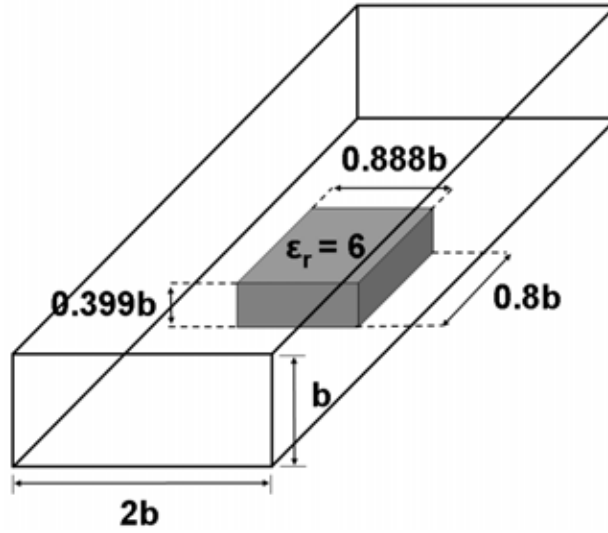


Figure 3.23: Dielectric in a rectangular waveguide from [48, 13].

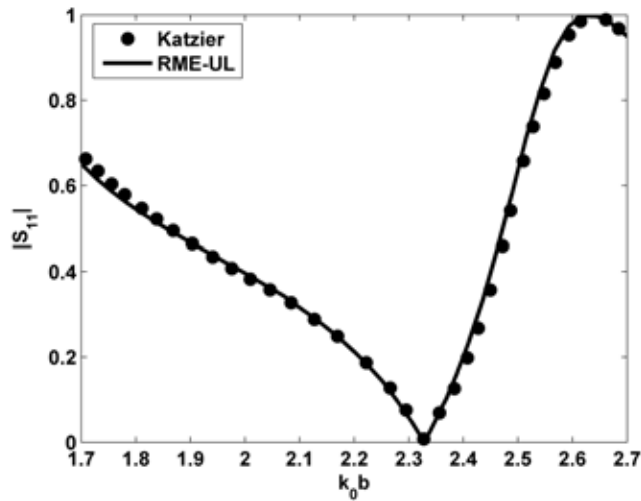


Figure 3.24: Modulus of the reflection coefficient S_{11} of the waveguide shown in fig. 3.23 as a function of $k_0 b$, where $k_0 = \omega\sqrt{\epsilon_0\mu_0}$ and b is the height of the rectangular waveguide. The RME-UL approach is compared with the method of orthogonal expansions of Katzier [48].

3.8 Summary

It is demonstrated in this chapter that an accurate solution can be obtained with nodal finite elements and the regularized formulation even in the presence of electromagnetic field singularities. To do so, a simplified version of the WRME method was used. This simplification consists of a weight equal to zero applied in the elements near a singularity and equal to one in the rest. The number of layers of elements whose weight is equal to zero depends on their size and order. For a given element order, this number is fixed, but if for some reason, it is meshed with very small elements near a singularity, this number must be increased to obtain a correct solution.

We tested several combinations of element order and ULs searching for accuracy and robustness. We reached to the conclusion that the best option is to use second-order elements and 3 ULs. It can also be obtained accurate solutions with higher order elements and 1 UL, but the computational cost is higher. On the other hand, it was not possible to attain a robust and accurate combination with first-order elements.

It is necessary to further study the relationship between the number of elements with a weight equal to zero and the element size, element order, and singularity order. Also, a deeper theoretical knowledge of how this simplification affects the well-conditioning and convergence of the regularized formulation is needed. In future work, a comparative performance of the RME-UL approach with other methods will be given.

Chapter 4

Specific absorption rate computations

The specific absorption rate is a measure of the rate at which electromagnetic energy is absorbed by a body when exposed to electromagnetic fields. The aim of this chapter is to validate the RME-UL method when applied to the computation of this quantity. We will explain, through examples, how to obtain the specific absorption rate with the RME-UL method and we will validate our approach by comparing the results with other numerical techniques. The work described here has been presented in [78, 77, 74, 75] and it is part of the project SANTTRA (Sistema de ANTenas para Transceptores de RAdio), Spanish MCIT PROFIT, ref.: FIT-330210-2006-44, framed in the project SMART (SMart Antennas system for Radio Transceivers), European Commission EU-REKA, ref.: PIDEA+ Project n°04-161. This work has also been partially founded by the project CaRDian (Cálculo de Radiación electromagnética en presencia de Dieléctricos mediante Análisis Numérico), Spanish MCI National R+D Plan 2008-2011, ref.: CIT-370000-2008-10.

4.1 Introduction

The specific absorption rate (SAR) is the power per unit mass absorbed by a body when illuminated by electromagnetic fields. This quantity is useful to determine, in combination with the heat equation, the temperature increase produced by an incident electromagnetic radiation inside a body. The SAR is also a quantity used for regulatory purposes. That is, before a mobile phone is available for sale to the general public, it must shown that the SAR is below some limits. In addition, a mobile phone with a high value of SAR imply that the energy is lost in unwanted heating instead of being used to transmit information.

The measurement of the SAR is performed in specialized test houses with complex and sophisticated systems. Besides, if you want your product complies with the government requirements, you have to send it to an accredited test house to obtain the certification. This process is expensive and time-consuming. Numerical simulations can save time and money predicting the value of the SAR before certification and improving the design of the product before manufacturing it. Also, in situations in which the measurement of the SAR is difficult, like in the measurement of the SAR in living creatures, the numerical simulations are of valuable help.

In the scenario present above, a volumetric, frequency domain, finite element formulation like the RME-UL approach seems to be a good choice for the numerical simulations. This is so, because it works naturally with complex geometries and materials and it can solve large problems thanks to the fact that it produces well-conditioned matrices easy to solve with iterative Krylov solvers.

The objective of this chapter is to validate the RME-UL method and assess its performance when applied to the computation of the SAR. In section 6.2 we define formally the SAR. In section 4.3 we present the numerical tool used for obtaining of the electromagnetic fields. In sections 4.4, 4.5 and 4.6 we calculate the SAR in different scenarios and compare the results with other numerical methods. In section 4.7, we make a numerical study of the the thermal effects induced by a RFID antenna in vials filled with blood plasma. Finally, in section 6.5, we present our conclusions.

4.2 Definitions

The Specific Absorption Rate (SAR) is defined as,

$$\text{SAR (W/kg)} = \frac{\sigma + \omega\epsilon''}{2\rho} |\mathbf{E}|^2 \quad (4.1)$$

where σ is the electrical conductivity, ϵ'' is the imaginary part of the electric permittivity (see section 2.3.1), ω is the frequency, ρ is the mass density and \mathbf{E} is the electric field. This definition comes from the expression (2.99) in chapter 2 and it represents the time-average power per unit mass dissipated as heat due to conductivity and dielectric losses. We assume that there is no magnetic losses ($\mu = \mu_0$).

When the SAR is employed for regulatory purposes it is usually averaged either over the whole body, or over a small sample volume (typically 1g or 10g of tissue). SAR limits for a radiating object depends of the country, for instance, in United States, the Federal Communications Commission (FCC) requires that phones sold for the general public have a SAR level at or below 1.6 W/kg taken over a volume of 1g of tissue with the shape of a cube. In the European Union, before a mobile phone is available for sale, it must show compliance with the European Radio & Telecommunication Terminal Equipment (R&TTE) directive 1999/5/EC. This directive limits the human exposure to radio frequency (RF) fields in accordance with the standard EN 50360:2001 (see table 4.1), developed by the European Committee for Electrotechnical Standardization (CENELEC).

User	SAR _{10g} (W/Kg)	SAR _{wb} (W/Kg)
General public	2	0.08
Occupational	10	0.40

Table 4.1: SAR limits specify by the CENELEC EN 50360:2001. SAR_{10g} is the average over 10 g of tissue with the shape of a cube. SAR_{wb} is the average over the whole body.

4.3 Numerical tool

The numerical tool used in this, and the following chapters, is called ERMES. ERMES stands for *Electric Regularized Maxwell Equations with Singularities* and it is the C++ implementation of the RME-UL method. ERMES uses GiD [29] for geometrical modeling, meshing and visualization of results. The user interface is detailed in appendix A.

The current version of ERMES is mono-processor and it runs in the operative system Windows XP 64-bit. ERMES uses a quasi-minimal residual (QMR) iterative solver [28] with a diagonal preconditioner to solve the linear systems resulting from the finite element discretization. The problems of this chapter were discretized with about $8e5-1e6$ tetrahedral second order nodal elements. The resulting linear systems had around $3e6-4e6$ unknowns. The RAM memory required was about 6-7 GB and the time needed to reach a residual ($\|Ax - b\| / \|b\|$) of less than $1e-3$ varies from 2 to 10 hours depending of the problem. These data are referred to a desktop computer with a CPU Intel Core 2 Quad Q9300 at 2.5 GHz and the operative system Microsoft Windows XP Professional x64 Edition v2003.

4.4 Ellipsoidal phantom in rectangular waveguide

In this validation example we compute the SAR in an ellipsoidal phantom placed inside a rectangular waveguide. The SAR values obtained with ERMES are compared with measurements and numerical simulations performed with the finite difference time domain method (FDTD).

4.4.1 Description of the problem

An ellipsoidal phantom, with a longer axis of 41 mm and a shorter axis of 30 mm, is filled with a substance of electrical properties $\epsilon = 43\epsilon_0$ and $\sigma = 0.97$ S/m. The phantom is placed at the center of a rectangular waveguide WR-975 (24.7625 cm x 12.3825 cm) and it is illuminated with the fundamental mode TE_{10} . The incident electric field has a frequency of $\nu = 900$ MHz, a maximum value of $|\mathbf{E}_{rms}| = |\mathbf{E}/\sqrt{2}| = 61.4$ V/m and a polarization parallel to the shorter axis of the ellipsoid. The weight of the phantom is $M = 20$ g. The weight and electrical properties of the phantom are comparable to those of a mouse. An outline of the problem is shown in fig. 4.1. The data for this example are taken from [52].

4.4.2 Finite element model

We computed the electric field inside the rectangular waveguide with the finite element model explained in section 3.7 of chapter 3. In this case we do not have any field singularity in the problem domain, then, we do not need to use any UL. The incident field \mathbf{E}_{10} (see equation (3.31)) is multiplied by the constant $\alpha = 61.4\sqrt{\gamma ab/i\omega\mu} = 0.4776$ to accomplish with the requirement that the maximum value of $|\mathbf{E}_{10}|$ must be $61.4\sqrt{2}$ V/m. Once the electric field is calculated, we obtain the SAR inside the ellipsoidal phantom with equation (4.1). The density $\rho = M/V$ is deduced using the formula $V = \pi AB^2/6$ for the volume of the ellipsoid, where A is the length of the mayor axis and B the length of the minor axis.

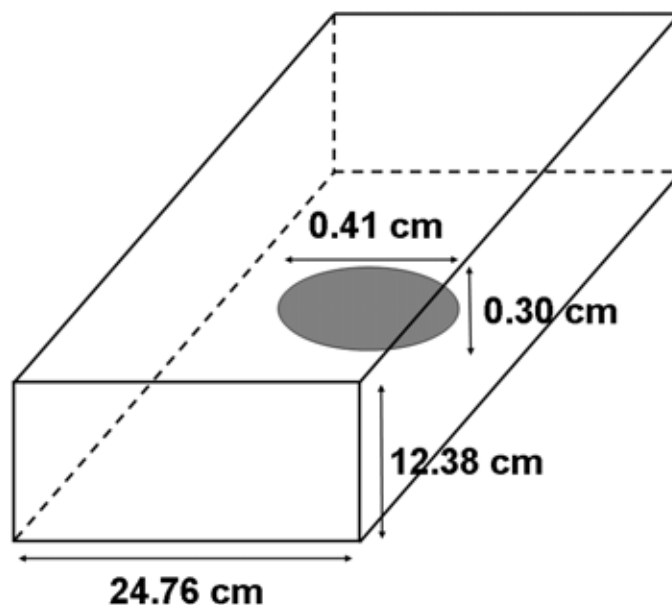


Figure 4.1: Ellipsoidal phantom inside rectangular waveguide. Data from [52].

4.4.3 Results

In table 4.2 is showed the SAR averaged over the whole volume of the ellipsoidal phantom (SAR_{avg}). This average SAR can be easily obtained experimentally by measuring the input and the output power in the waveguide ports [52]. On the other hand, the SAR distribution inside the phantom is more difficult to measure and this is where numerical simulations can be very helpful. In figures 4.2 and 4.3 is shown the SAR distribution inside the ellipsoidal phantom. The presence of "hot spots" where the SAR values are several times bigger than the average can be clearly observed with the help of the numerical simulation.

Method	SAR_{avg} (W/Kg)
Measured	0.06
FDTD	0.05
ERMES	0.05

Table 4.2: SAR averaged over the whole volume of the ellipsoidal phantom (SAR_{avg}). The SAR_{avg} value measured in [52] is compared with the FDTD simulation performed in [52] and the result obtained with ERMES.

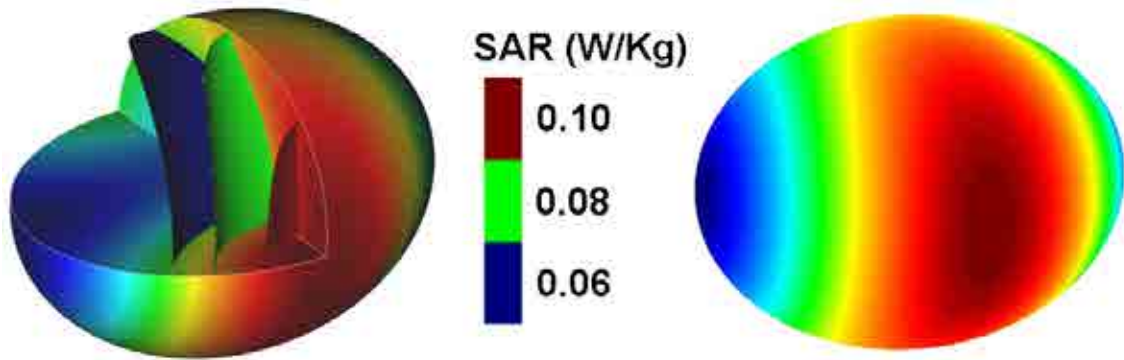


Figure 4.2: SAR (W/Kg) inside the ellipsoidal phantom. Iso-surfaces.

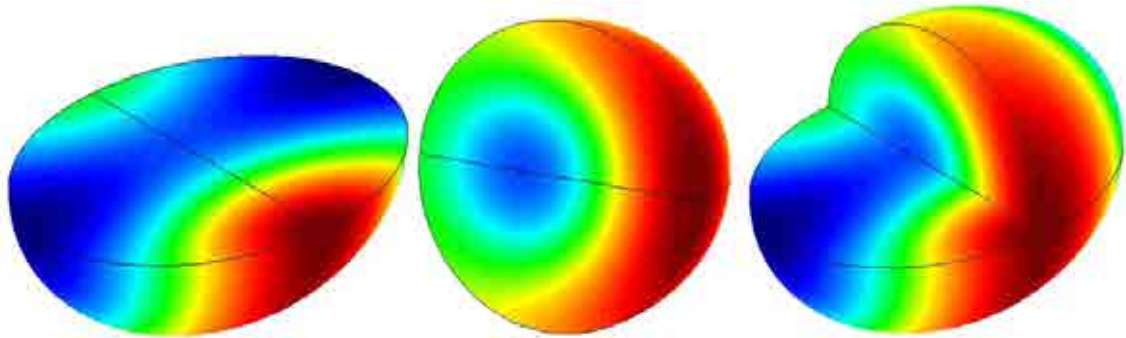


Figure 4.3: SAR (W/Kg) inside the ellipsoidal phantom.

4.5 PROCOM MU9-XP4 antenna installed on motorbike

The objective of this validation example is to calculate the SAR inside a body produced by an antenna installed on a motorbike. The results obtained with ERMES are compared with those provided by a commercial software which implements the method of moments.

4.5.1 Description of the problem

A body with a mass density $\rho = 1000 \text{ Kg/m}^3$ and electric properties $\epsilon = 41.3\epsilon_0$ and $\sigma = 0.58 \text{ S/m}$ is placed at a distance of 0.6 m from a PROCOM MU9-XP4 antenna (see figures 4.4 and 4.5). The antenna is fed by a 50Ω coaxial cable with $P_0 = 10 \text{ W}$ (40 dBm) at a frequency of $\nu = 406 \text{ MHz}$. The ground is located 1.22 m below the feeding point of the antenna and a luggage rack is placed 0.15 m below the same feeding point.

4.5.2 Finite element model

The finite element model used to solve numerically this problem is depicted in fig. 4.6. We applied the PEC boundary condition (3.12) to the ground, antenna and luggage rack, the first order absorbing boundary condition (3.15) to the exterior surface and the PMC boundary condition (3.13) to the symmetry plane. The antenna is fed by a coaxial line (see fig. 4.8), in where it is assumed that only the fundamental mode TEM is propagating. Then, we imposed the following boundary condition at the coaxial port

$$\begin{aligned}\hat{\mathbf{n}} \times \nabla \times \mathbf{E} &= \gamma (\hat{\mathbf{n}} \times \hat{\mathbf{n}} \times \mathbf{E}) + \mathbf{U}, \\ \hat{\mathbf{n}} \cdot \mathbf{E} &= 0\end{aligned}\quad (4.2)$$

where $\gamma = i\omega\sqrt{\varepsilon\mu}$ is the propagation constant of the fundamental mode and

$$\mathbf{U} = -2\gamma (\hat{\mathbf{n}} \times \hat{\mathbf{n}} \times \mathbf{E}_{\text{TEM}}). \quad (4.3)$$

The field \mathbf{E}_{TEM} is the incident field imposed in the input port:

$$\mathbf{E}_{\text{TEM}} = \sqrt{\frac{\eta}{2\pi \ln(b/a)}} \begin{pmatrix} e^{\gamma z} \\ \mathbf{r} \end{pmatrix} \hat{\mathbf{r}}, \quad (4.4)$$

being $\eta = \sqrt{\mu/\varepsilon}$, a the inner radius of the coaxial, b the exterior radius of the coaxial, $r = \sqrt{x^2 + y^2}$ and $\hat{\mathbf{r}} = (x/r, y/r)$. The port plane is in the xy -plane and the direction of propagation is along the z -axis. In this case, we have that $\eta = \sqrt{\mu_0/\varepsilon_0}$, $a = 1.25$ mm and $b = 2.88$ mm. Therefore, the characteristic impedance Z_0 of the coaxial line is

$$Z_0 = \frac{\eta}{2\pi} \ln(b/a) = 50 \Omega. \quad (4.5)$$

The geometry was meshed with 839360 tetrahedral second-order nodal elements (see fig. 4.7). We used 3 ULs in the edges of the luggage rack and in the edges of the base and tip of the antenna. Once the field \mathbf{E} was computed, we multiplied the result by the constant

$$\alpha = \sqrt{\frac{2P_0}{1 - |S_{11}|^2}}, \quad (4.6)$$

where $P_0 = 10$ W and S_{11} is the reflection coefficient of the coaxial. The parameter S_{11} is calculated as in (3.27), but with \mathbf{E}_{TEM} instead of \mathbf{E}_{10} . We multiply the fields by α to impose that all the power sent to antenna is radiated, which is the worst-case scenario.

4.5.3 Results

EADS Defense & Security [9] computed the problem described above in the frame of the project SMART. They used the commercial software FEKO [25], which implements the method of moments (MoM). They modeled the feeding of the antenna with an impedance matching coil at its base (see fig. 4.8). The results of the simulations performed with ERMES and FEKO are shown in figures 4.9, 4.10 and 4.11 and in table 4.3. The maximum SAR value obtained with ERMES was 0.06 W/Kg, located in the neck. The maximum SAR value obtained with FEKO was 0.07 W/Kg, also located in the neck. The SAR averaged over the 10g cube was 0.04 W/Kg in ERMES and 0.06 W/Kg in FEKO.

Method	SAR _{max} (W/Kg)	SAR _{10g} (W/Kg)
FEKO	0.07 (neck)	0.06
ERMES	0.06 (neck)	0.04

Table 4.3: Maximum SAR (SAR_{max}) and SAR averaged over the 10g cube (SAR_{10g}) obtained with FEKO and ERMES. The maximum SAR is located in the neck.



Figure 4.4: PROCOM MU9-XP4 antenna installed on a motorbike.

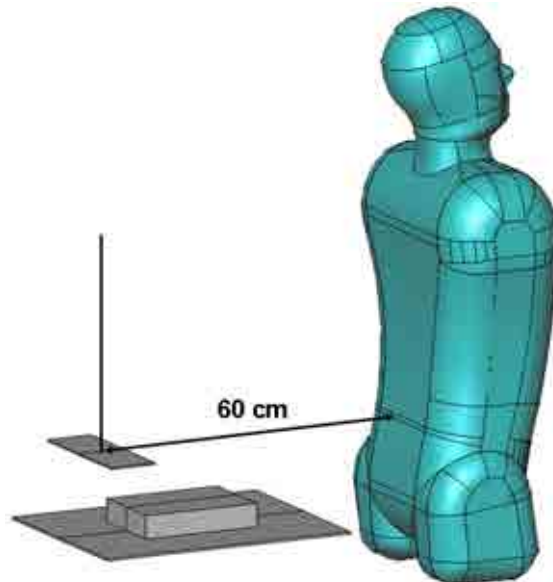


Figure 4.5: PROCOM MU9-XP4 antenna installed on a motorbike. CAD model.

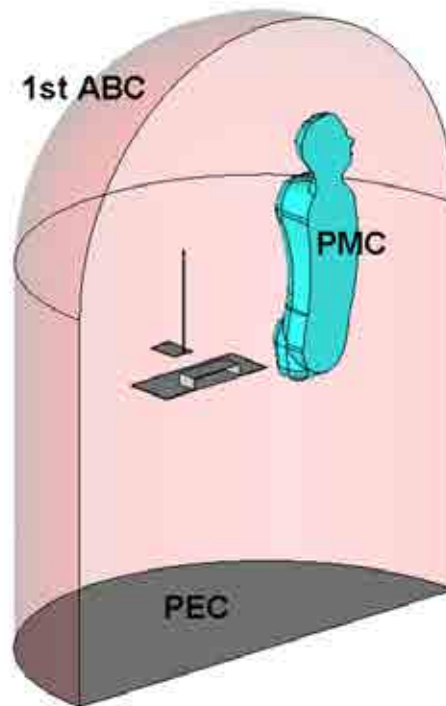


Figure 4.6: PROCOM MU9-XP4 antenna installed in a motorbike. FEM model.

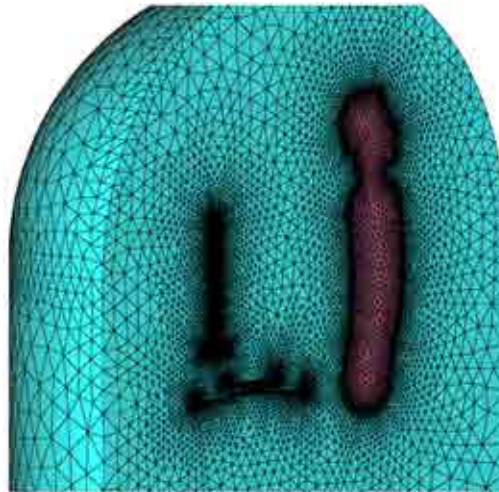


Figure 4.7: PROCOM MU9-XP4 antenna installed on a motorbike. FEM mesh. The mesh is composed of 839360 tetrahedral second-order nodal elements.

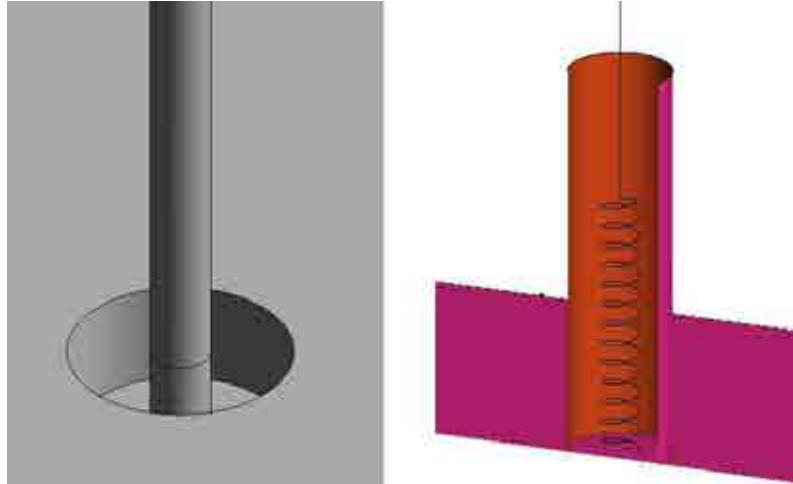


Figure 4.8: Coaxial feeding at the bottom of the PROCOM MU9-XP4 antenna. Left: Coaxial model used by ERMES. Right: Coaxial model used by FEKO.

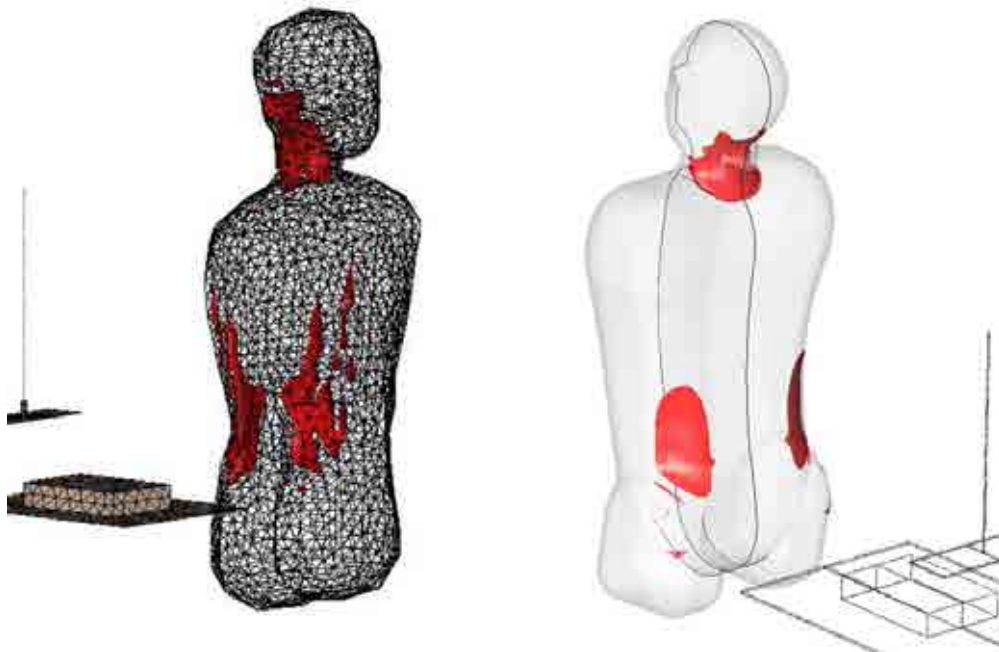


Figure 4.9: Iso-surfaces for SAR = 0.03 W/kg. Left: FEKO results. Right: ERMES results.

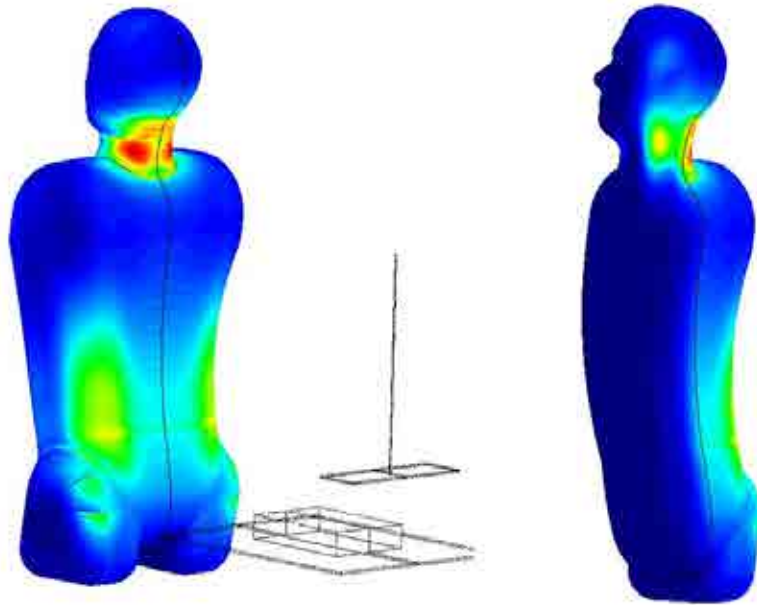


Figure 4.10: SAR distribution calculated by ERMES. Maximum value is 0.06 W/Kg, located in the neck.

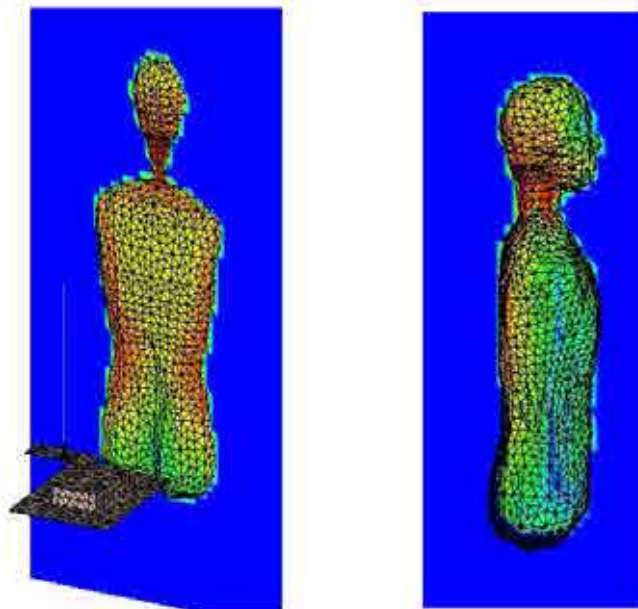


Figure 4.11: SAR distribution calculated by FEKO. Maximum value is 0.07 W/Kg, located in the neck.

4.6 PMR antenna near SAM head

In this validation example we compute the SAR produced by a professional mobile radio (PMR) antenna in a specific anthropomorphic mannequin (SAM) head. The results obtained with ERMES are compared with those provided by FEKO.

4.6.1 Description of the problem

A PMR antenna (see fig. 4.12) is placed near a SAM head as shown in fig. 4.13. The antenna is fed with $P_0 = 2$ W (33 dBm) at a frequency of $\nu = 400$ MHz. The mass density of the SAM head is $\rho = 1000$ Kg/m³ and its electrical properties are $\epsilon = 45.5\epsilon_0$ and $\sigma = 0.7$ S/m. The electrical permittivity of the GPS antenna substrate is $\epsilon = 3\epsilon_0$.



Figure 4.12: PMR antenna (with a GPS antenna at its base) installed on handset. Prototype designed and manufactured by Radiall [88].

4.6.2 Finite element model

We applied the PEC boundary condition (3.12) to the PMR antenna, GPS antenna and handset and the first order absorbing boundary condition (3.15) to a 70 cm diameter spherical surface centered at the feeding point of the antenna. We fed the antenna with a current probe located at its base (see fig. 4.14). The geometry was meshed with 838840 tetrahedral second-order nodal elements (see fig. 4.15). We used 3 ULs in the edges of the handset, tip of the PMR antenna, edges of the GPS antenna and edges of the dielectric substrate. We impose a radiated output power of $P_0 = 2$ W by multiplying the computed \mathbf{E} field by the constant

$$\alpha = \sqrt{\frac{2P_0}{-\int_s \text{Real} [\mathbf{E} \cdot \bar{\mathbf{J}}]}}, \quad (4.7)$$

where s is the volume of the current probe.

4.6.3 Results

EADS Defense & Security computed the problem described above with the commercial software FEKO in the frame of the project SMART. They modeled the feeding of the antenna with a voltage gap (see fig. 4.18). The results of the simulations performed with ERMES and FEKO are shown in figures 4.16, 4.17 and 4.19 and in table 4.4. The differences in the results can be attributed to the different geometries employed in the computations. We must take into account that the SAR is very sensitive to the positioning of the handset with respect to the SAM head. For instance, if we move the handset 0.4 cm closer to the surface of the SAM head then, the value of the SAR averaged over the 10g cube obtained with ERMES rises to 3.36 W/Kg.

Method	SAR _{10g} (W/Kg)
FEKO	3.00
ERMES	2.82

Table 4.4: SAR averaged over the 10g cube (SAR_{10g}) obtained with FEKO and ERMES.

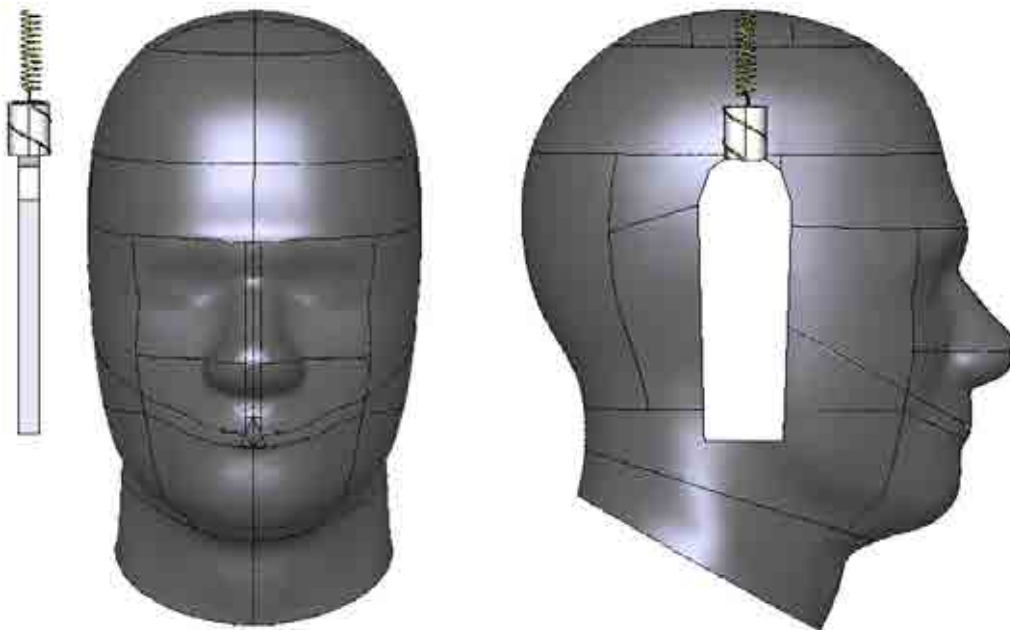


Figure 4.13: Positioning of the PMR antenna. Left: Frontal view. Right: Lateral view. The distance between handset and SAM head is 2 cm.

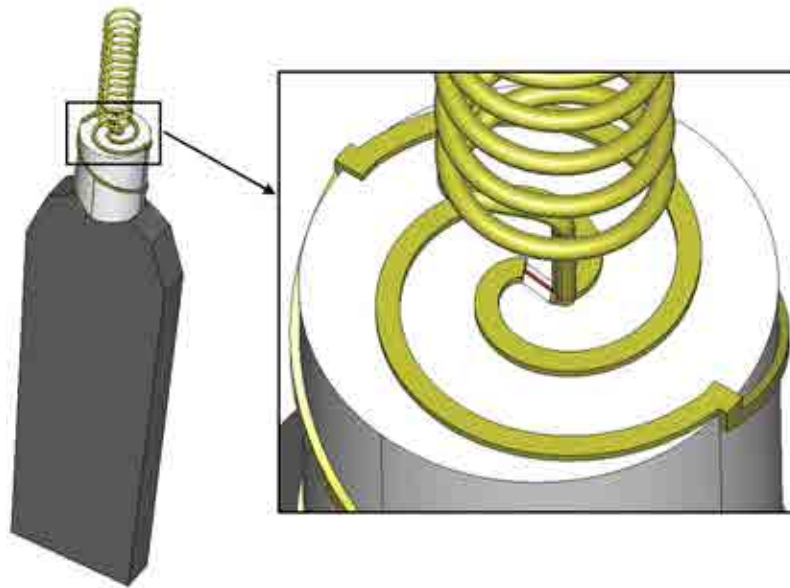


Figure 4.14: Current probe used by ERMES to feed the PMR antenna.

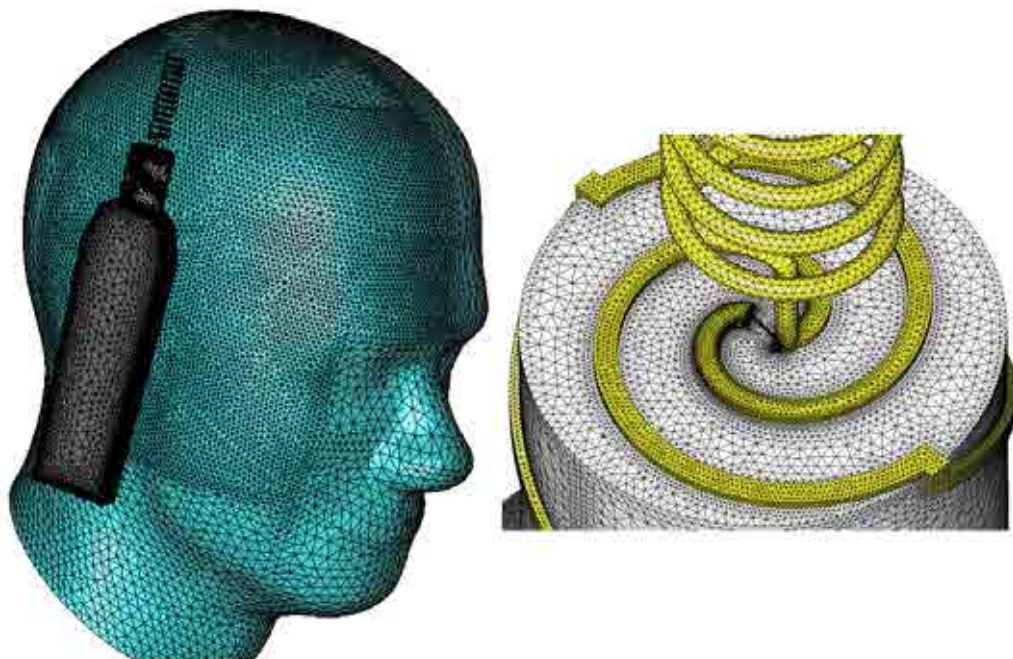


Figure 4.15: Details of the FEM mesh used by ERMES.

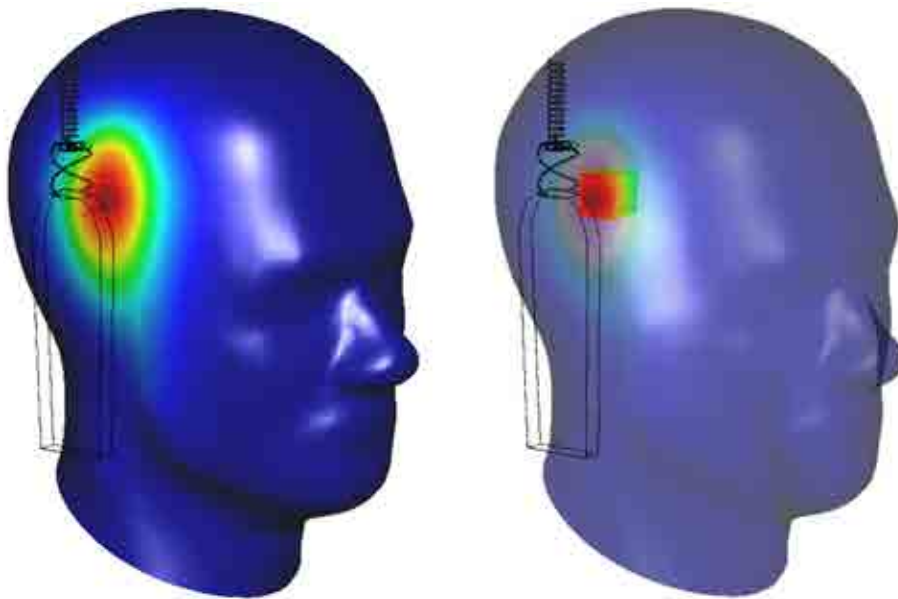


Figure 4.16: SAR distribution calculated by ERMES and location of the 10g cube. The maximum SAR is 4.92 W/Kg. The SAR averaged over the 10g cube is 2.82 W/Kg.

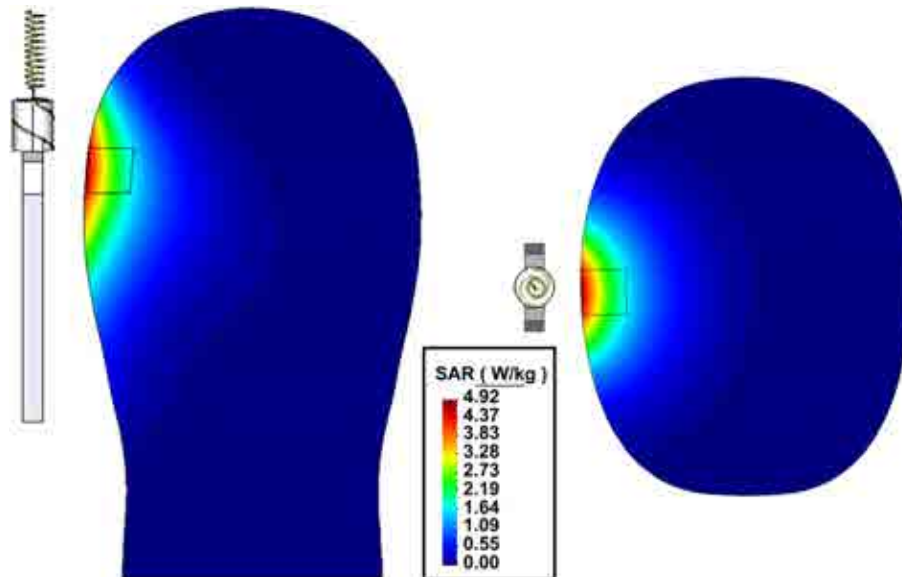


Figure 4.17: SAR distribution calculated by ERMES. Sections of the SAM head. Left: Frontal view. Right: Upper view.

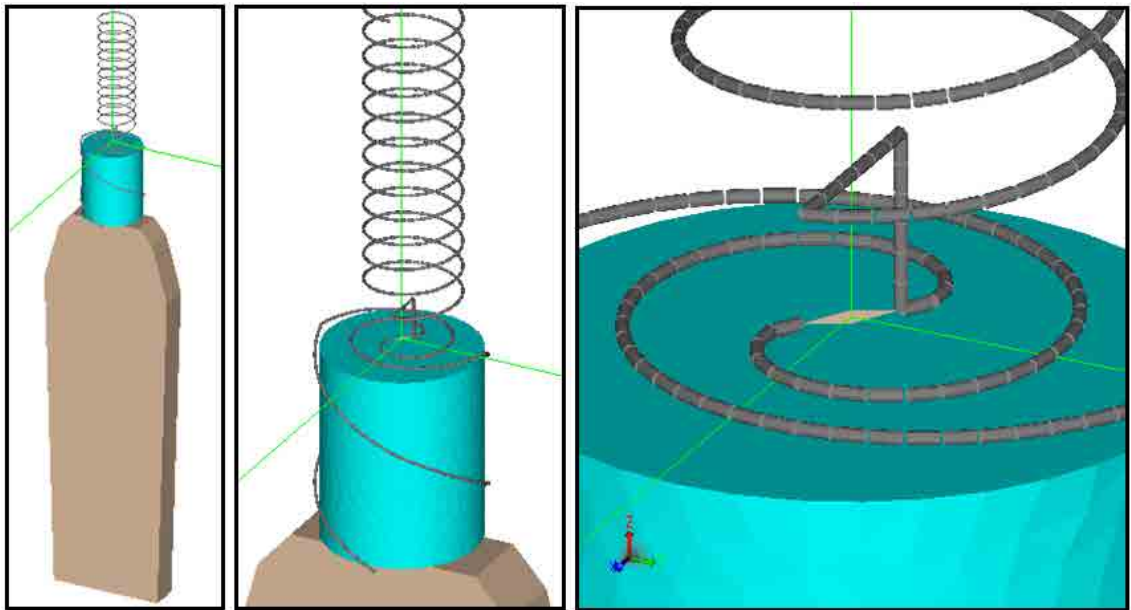


Figure 4.18: Details of the geometry used by FEKO to model the PMR antenna. The antenna is fed by a voltage gap.

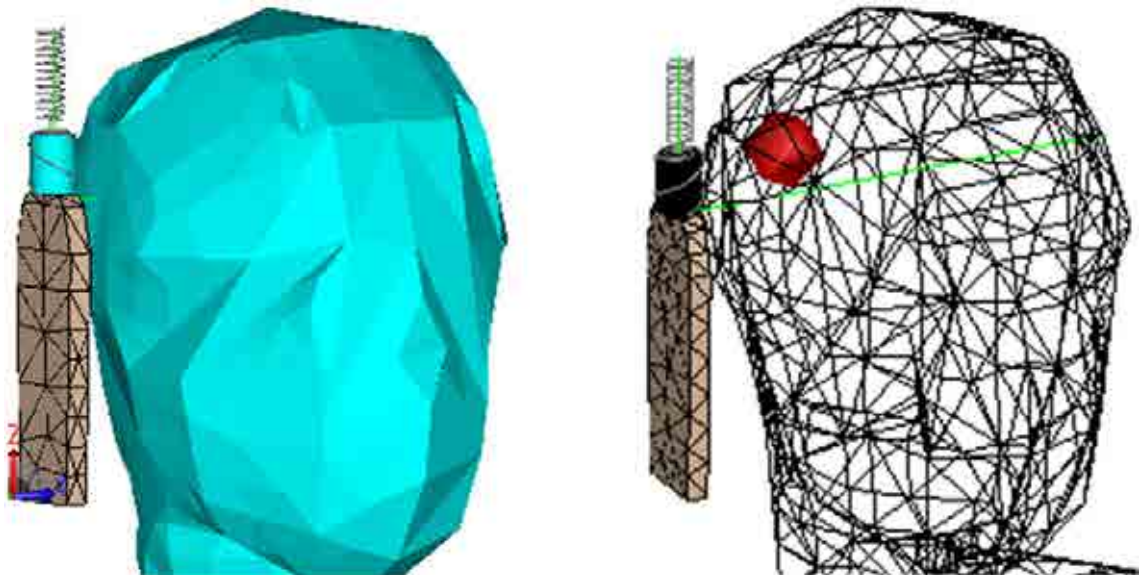


Figure 4.19: Location of the 10g cube by FEKO. The SAR averaged over the 10g cube is 3.00 W/Kg.

4.7 RFID antenna near vials of blood plasma

This section contains a numerical study of the thermal effects induced by a commercial RFID antenna in vials filled with blood plasma. The antenna is located under a conveyor belt which transports cardboard boxes bearing test tubes or pooling bottles filled with blood plasma. The aim of this study is to evaluate the worst-case scenario temperature increase produced by the RFID antenna in the blood plasma contained in the vials. This study has been fostered by GRIFOLS [31].

4.7.1 Description of the problem

RFID stands for Radio Frequency IDentification and it consists in the use of a tag incorporated into a product, animal, or person for the purpose of identification using radio waves. There are basically two types of RFID tags: active tags, which can transmit signals autonomously, and passive tags, which require an external energy source to transmit signals. In this study we are only interested in passive tags. The RFID process with passive tags is as follows. First, the tag receives electromagnetic energy from the RFID reader. Then, the tag uses this energy to send back the data stored in it. Finally, the reader receives the tag's radio waves and interprets the signals. Part of the electromagnetic energy that reaches the tag also penetrates into the object where the tag is incorporated. The aim of this work is to study numerically the thermal effects induced in these objects.

In our case, we have a RFID antenna under a conveyor belt. Cardboard boxes bearing test tubes or pooling bottles filled with blood plasma are moved along the conveyor belt and pass above the antenna. When the boxes are above the antenna, some of the electromagnetic radiation that is used to read the tags is absorbed by the blood plasma contained in the vials. The absorbed radiation heats the blood plasma and increases its temperature. The question we try to answer here is how fast the temperature increases in the worst-case scenario. More specifically, we calculate the time required to increase the temperature 0.1°C , at the point of maximum SAR, and under the supposition that no mechanism of heat dissipation is acting during the excitation.

The heating induced by the RFID antenna was computed for blood plasma at room temperature ($+25^{\circ}\text{C}$) and frozen (-30°C). The physical properties of the blood plasma at both temperatures are summarized in table 4.5. The plasma is contained in test tubes or pooling bottles (see figures 4.20 and 4.26). These vials are carried inside cardboard boxes containing 96 test tubes or 15 pooling bottles (see fig. 4.20). The cardboard boxes are transported by a conveyor belt passing above the RFID antenna. The commercial RFID antenna used for tag identification is a CS-777 Bricyard operating at a frequency of $\nu = 915\text{ MHz}$ and with an input power of $P_0 = 1\text{ W}$.

4.7.2 Finite element model

The finite element model used in this study is depicted in figures 4.21 and 4.27. We applied the PEC boundary condition (3.12) to the ground, the first order absorbing boundary condition (3.15) to the exterior surface and the PMC boundary condition (3.13) to the symmetry planes. We do not have any field singularity in the problem domain, then, we do not need to use ULs.

The antenna CS-777 Bricyard is a segmented loop antenna [21, 87] designed for UHF near-field RFID applications. This type of antenna produce a strong and uniform magnetic field distribution in the near-field region, which ensures a good inductive coupling between the tag and the antenna. Such a coupling system is the most appropriate to operate in the vicinity of liquids and metals with low magnetic permeability. The characteristic field distribution of a segmented loop antenna is achieved with an electrical current which is in-phase and has the same magnitude along the loop. Therefore, we have modeled the CS-777 Bricyard as a circular current loop of constant phase and magnitude. The loop has an internal diameter of 20 cm and a rectangular section which is 0.6 cm wide and 0.2 cm high. The current loop is enclosed in a metallic case with a plastic cover in the front. To model the casing of the antenna, we placed the current loop on a PEC plane separated 2 cm from the bottom of the cardboard boxes. We impose a radiated output power of $P_0 = 1$ W by multiplying the computed \mathbf{E} field by the constant

$$\alpha = \sqrt{\frac{2P_0}{-\int_s \text{Real} [\mathbf{E} \cdot \bar{\mathbf{J}}]}}, \quad (4.8)$$

where s is the volume of the current loop.

In fig. 4.21 is shown a quarter of the cardboard box containing 96 test tubes. The dimensions of the box are detailed in fig. 4.20. Inside the box there are 8 rows of 12 test tubes. The distance between tubes in the same row is 0.24 cm. The distance between rows is 0.35 cm. The box is positioned 2 cm above the RFID antenna.

In fig. 4.27 is shown a quarter of the cardboard box containing 15 poling bottles. Inside the box there are 3 rows of 5 plasma pooling bottles. The distance between bottles in the same row is 0.5 cm. The distance between rows is also 0.5 cm. The box is positioned 2 cm above the RFID antenna.

T (°C)	ϵ'_r (ϵ'/ϵ_0)	ϵ''_r (ϵ''/ϵ_0)	σ (S/m)	ρ (Kg/m ³)	c (J/Kg°C)
+25	70	0	1.7	1025	3780
-30	3	0.3	0	920	2050

Table 4.5: Physical properties of the blood plasma at room temperature (+25°C) and frozen (-30°C), being ϵ'_r the real part of the relative electric permittivity, ϵ''_r the imaginary part of the relative electric permittivity, σ the electrical conductivity, ρ the mass density and c the specific heat capacity at constant pressure. Data extrapolated from [43, 24, 47, 38].

4.7.3 Results

The results of the simulations are shown in figures 4.22,4.23,4.24, 4.25,4.28 and 4.29. We can see that the higher SAR is found in the vials positioned just atop the current loop of the antenna. The values of the maximum SAR (SAR_{\max}) obtained in each case are summarized in table 4.6.

Once the SAR is known, we can estimate the time needed to increment of temperature of the blood plasma $\Delta T = 0.1^\circ\text{C}$. The relation of SAR with the temperature can be very complex if we take into account heat dissipation processes as conduction or convection. However, if we want to calculate the increase of temperature in the worst-case scenario possible, where all the electromagnetic energy is used to increase temperature, this relation is very simple,

$$\Delta T \approx \frac{\text{SAR} \Delta t}{c}, \quad (4.9)$$

where ΔT is the temperature increase, c is the specific heat capacity and Δt is the duration of the electromagnetic radiation excitation. In table 4.7 is shown the time (Δt) needed to increase the temperature of the blood plasma $\Delta T = 0.1^\circ\text{C}$, at the point of maximum SAR, and assuming that no mechanism of heat dissipation is present. As can be seen in the table 4.7, the shorter time is $\Delta t = 75$ s for the pooling bottle at room temperature ($+25^\circ\text{C}$). Then, since a typical read cycle lasts 100 ms, it would take 750 continuous reading cycles to produce an increase 0.1°C in the worst-case scenario. So, we can conclude that, the RFID technology analyzed in this work, do not alter the quality of the blood plasma in a standard situation of a few readings cycles, when the vials are carried by a conveyor belt equipped with RFID antennas. The only scenario that would present a problem would be a box left forgotten just above a RFID reader in continuous operation. However, this situation is very unlikely because motion detectors are usually placed in the conveyor belt and the RFID readers are only activated when the belt is moving.

	Test tube	Pooling bottle
T ($^\circ\text{C}$)	SAR _{max} (W/Kg)	SAR _{max} (W/Kg)
+25	2.63	5.04
-30	0.43	0.52

Table 4.6: Maximum SAR (SAR_{max}).

	Test tube	Pooling bottle
T ($^\circ\text{C}$)	Δt (s)	Δt (s)
+25	144	75
-30	477	394

Table 4.7: Time (Δt) needed to increase the temperature of the blood plasma $\Delta T = 0.1^\circ\text{C}$, at the point of maximum SAR, and assuming that no mechanism of heat dissipation is present.

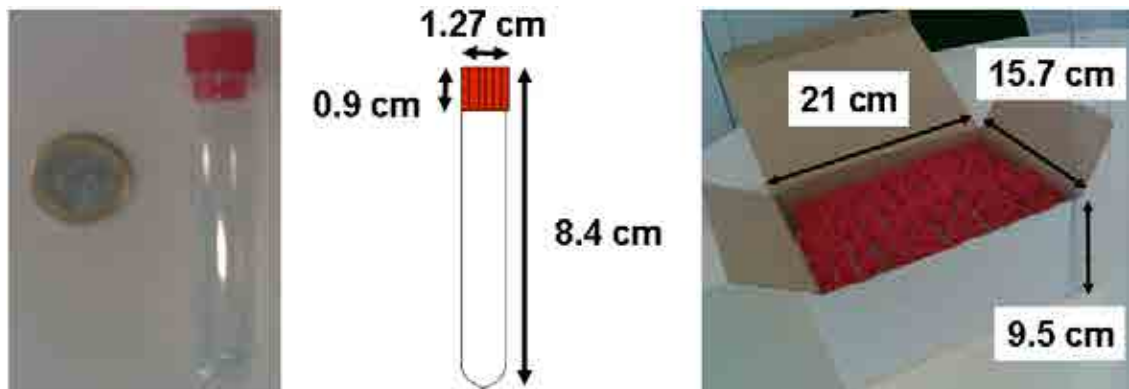


Figure 4.20: Left: Dimensions of a test tube. Right: Dimensions of the cardboard box containing 96 test tubes.

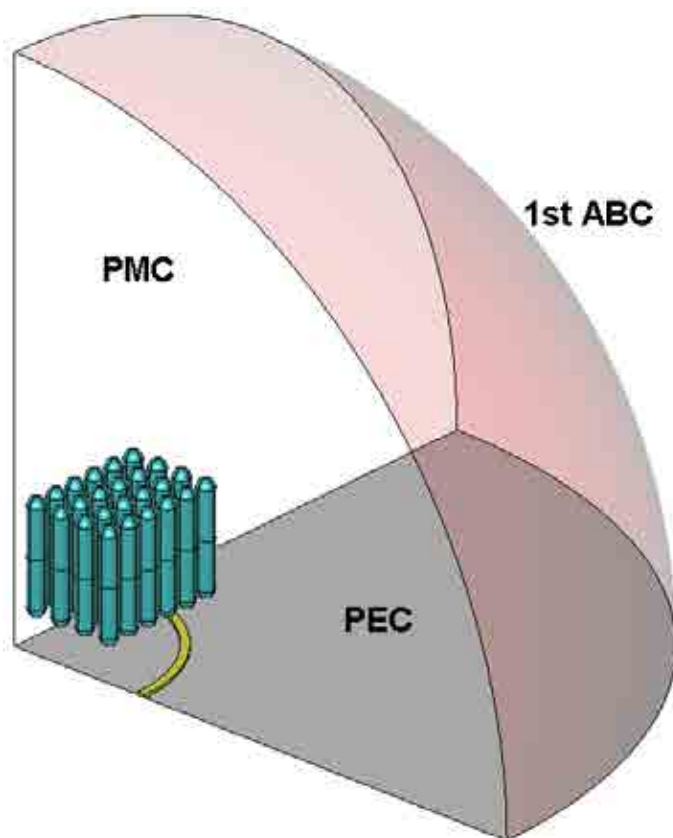


Figure 4.21: FEM model of the cardboard box containing 96 test tubes.

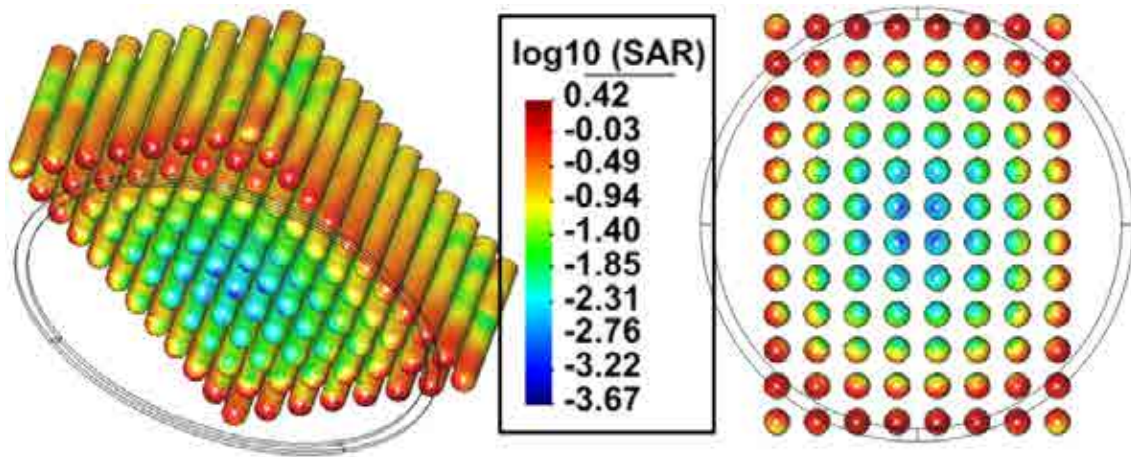


Figure 4.22: SAR distribution in the box containing 96 test tubes with blood plasma at room temperature (+25°C). Logarithmic scale.

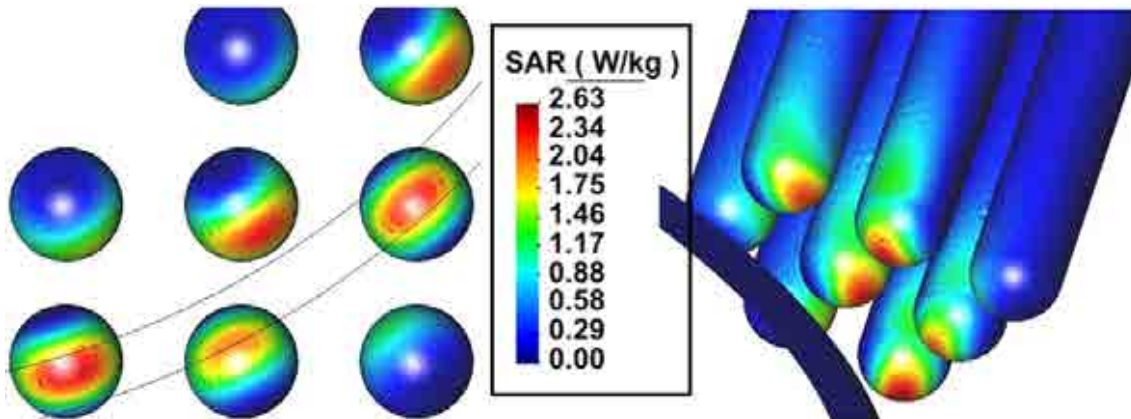


Figure 4.23: SAR distribution in the box containing 96 test tubes with blood plasma at room temperature (+25°C). Detail.

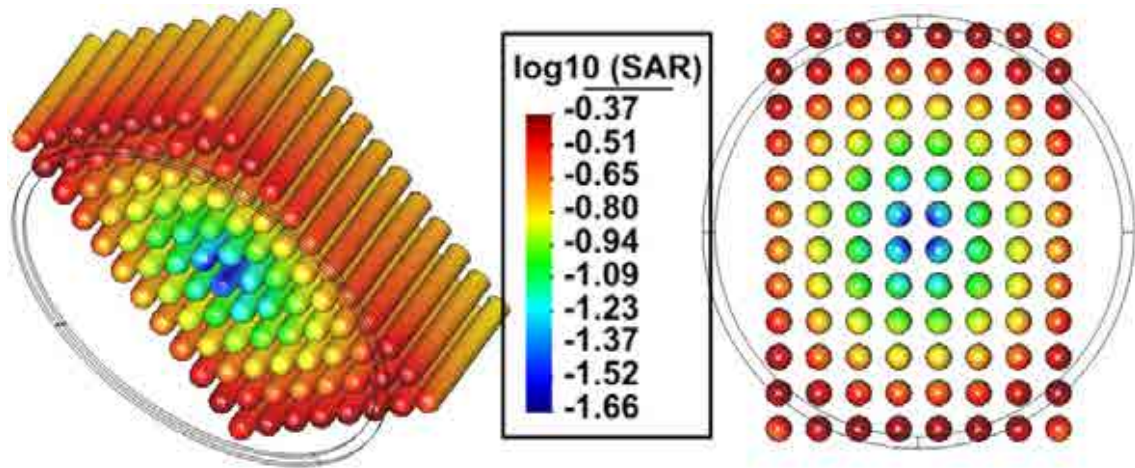


Figure 4.24: SAR distribution in the box containing 96 test tubes with frozen blood plasma (-30°C). Logarithmic scale.

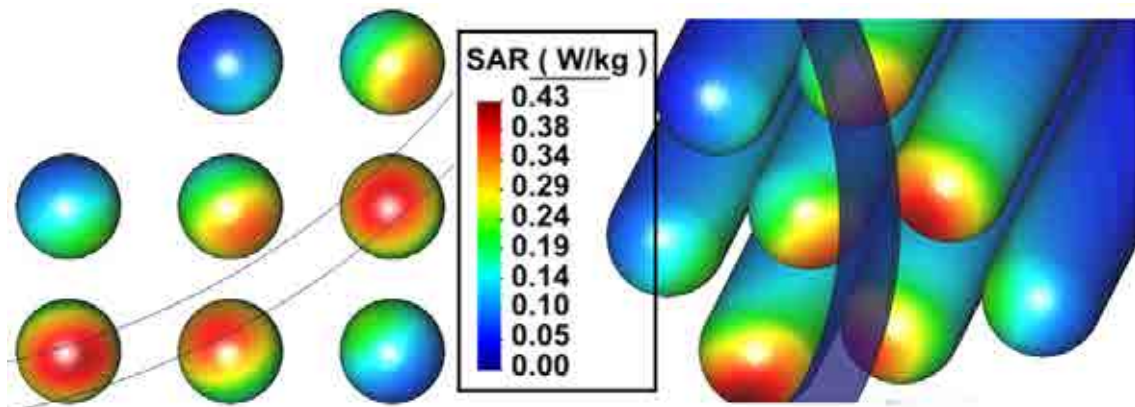


Figure 4.25: SAR distribution in the box containing 96 test tubes with frozen blood plasma (-30°C). Detail.



Figure 4.26: Dimensions of a pooling bottle.

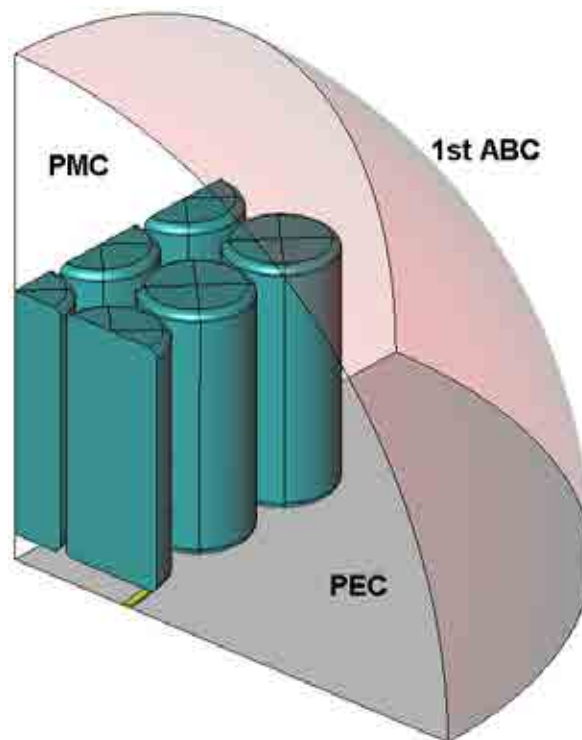


Figure 4.27: FEM model of the cardboard box containing 15 pooling bottles.

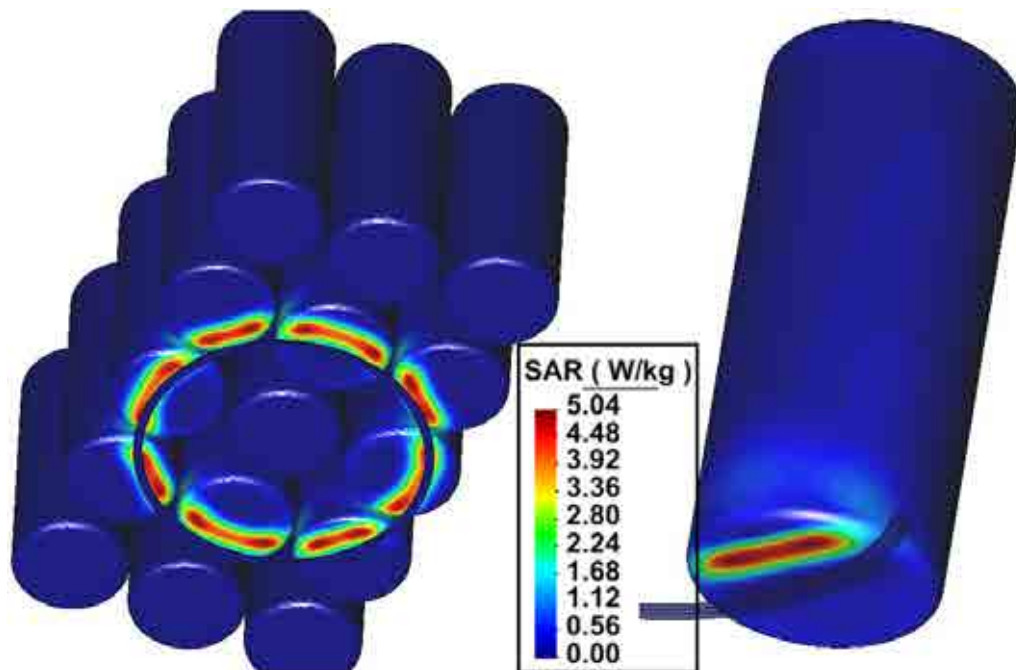


Figure 4.28: SAR distribution in the box containing 15 pooling bottles with blood plasma at room temperature (+25°C).

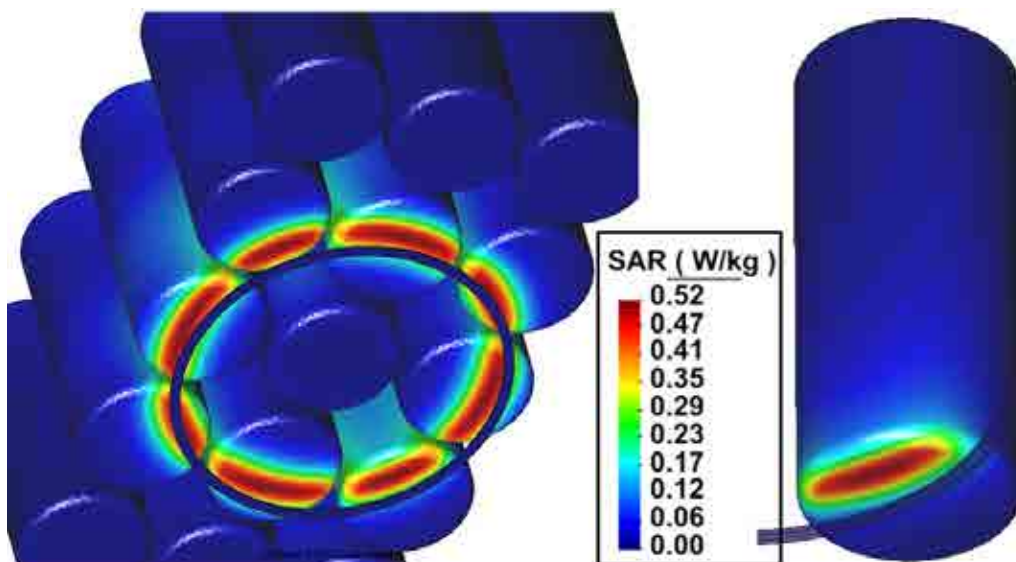


Figure 4.29: SAR distribution in the box containing 15 pooling bottles with frozen blood plasma (-30°C).

4.8 Summary

In this chapter we have applied the RME-UL method to the computation of the SAR and we have validated our approach by comparing the results with those obtained with other numerical methods. Although the RME-UL method is appropriate for solving SAR related problems there are some scenarios in where its efficiency can be put in jeopardy: when there are too many reentrant metallic or dielectric edges in the problem domain and when the source and the target are far away from each other.

In the vicinity of reentrant metallic or dielectric edges we need to mesh with small elements to catch the singular behavior of the fields. This fine meshing increases dramatically the number of unknowns and, in consequence, the computational cost. Moreover, the presence of field singularities in these edges worsen the condition number of the FEM matrix and we need more iterations of the Krylov solvers to reach the solution. Therefore, we must improve the treatment of the field singularities to make the RME-UL approach more efficient.

Another problem of the RME-UL approach is that it needs to calculate the electric field in the space surrounding source (antenna) and target (dielectric body). Then, if the distance between them is large, the volume needed to run the simulation is large and, as a result, the computational cost is high. A possible solution in these cases is the implementation of hybrid methods (e.g. FEM-MoM). Therefore, we must research how to hybridize the RME-UL approach with MoM or asymptotic methods to improve its performance in electrically large problems.

Chapter 5

Electromagnetic metal forming

This chapter presents a numerical model for computing the Lorentz force that drives an electromagnetic forming process. This model is also able to estimate the optimum capacitance at which it is attained the maximum workpiece deformation. The input data required are the geometry and material properties of the system coil-workpiece and the electrical parameters of the capacitor bank. The output data are the optimum capacitance, the current flowing through the coil and the Lorentz force acting on the workpiece. The main advantage of our approach is that it provides an explicit relation between the capacitance of the capacitor bank and the frequency of the discharge, which is a key parameter in the design of an electromagnetic forming system. The model is applied to different forming processes and the results compared with theoretical predictions and measurements of other authors. The work described in this chapter has been presented in [79, 80] and it is part of the project SICEM (SIMulación multifísica para el diseño de Conformado ElectroMagnético), Spanish MEC National R+D Plan 2004-2007, ref.: DPI2006-15677-C02-01.

5.1 Introduction

Electromagnetic forming (EMF) is a high velocity forming technique that uses electromagnetic forces to shape metallic workpieces. The process starts when a capacitor bank is discharged through a coil. The transient electric current which flows through the coil generates a time-varying magnetic field around it. By Faraday's law of induction, the time-varying magnetic field induces electric currents in any nearby conductive material. According to Lenz's law, these induced currents flow in the opposite direction to the primary currents in the coil. Then, by Ampere's force law, a repulsive force arises between the coil and the conductive material. If this repulsive force is strong enough to stress the workpiece beyond its yield point then it can shape it with the help of a die or a mandrel.

Although low-conductive, non-symmetrical, small diameter or heavy gauge workpieces can not be suitable for EMF, this technique presents several advantages. For example: no tool marks are produced on the surfaces of the workpieces, no lubricant is required, improved formability, less wrinkling, controlled springback, reduced number of operations and lower energy cost. In order to successfully design sophisticated EMF systems and control their performance, it is necessary to

advance in the development of theoretical and numerical models of the EMF process. This is the objective of the present work. More specifically, we focus our attention on the numerical analysis of the electromagnetic part of the EMF process. For a review on the state-of-the-art of EMF see [22, 27, 58] or the introductory chapters in [65, 99, 19, 100], where it is given a general overview about the EMF process and also abundant bibliography.

In this chapter we present a method to compute numerically the Lorentz force that drives an EMF process. We also estimate the optimum frequency and capacitance at which it is attained the maximum workpiece deformation for a given initial energy and a given set of coil and workpiece. The input data required are the geometry and material properties of the system coil-workpiece and the electrical parameters of the capacitor bank. With these data and the time-harmonic Maxwell's equations we are able to calculate the optimum capacitance, the current flowing through the coil and the electromagnetic forces acting on the workpiece. The main advantage of this method is that it provides an explicit relation between the capacitance of the capacitor bank and the frequency of the discharge which, as it is shown in [41, 117, 34], is a key parameter in the design of an EMF system. Also, our frequency domain approach is computationally efficient and it offers an alternative to the more extended time domain methods.

In section 5.2 we summarize the coupling strategies which connect the electromagnetic equations with the other physical phenomena involved in an EMF process.

In section 5.3 we explain in detail the electromagnetic model employed in this work. We show the general formulas and the assumptions we made to compute the intensity flowing through the coil and the Lorentz force acting on the workpiece.

In section 5.4 we describe the numerical tools used to obtain the electromagnetic fields and the deformation of the workpiece.

In section 5.5 and 5.6 we apply the method detailed in section 5.3 to the bulging of a metal sheet and the bulging of a cylindrical tube. Our results are compared with theoretical predictions and measurements found in the literature.

In section 5.7 we explain how to estimate the optimum frequency and capacitance at which it is attained the maximum workpiece deformation for a given initial energy and a given set of coil and workpiece.

Finally, in section 5.8 we apply the techniques detailed in section 5.7 to a tube bulging process and to a tube compression process.

5.2 Coupling strategies

EMF is fundamentally an electro-thermo-mechanical process. Different coupling strategies have been proposed to solve numerically this multi-physics problem, but they can be reduced to these three categories: direct or monolithic coupling, sequential coupling and loose coupling.

The direct or monolithic coupling [104, 57] consists in solving the full set of field equations every time step. This approach is the most accurate but it does not take advantage of the different time scales characterizing electromagnetic, mechanical and thermal transients. Moreover, the linear system resulting from the numerical discretization leads to large non-symmetric matrices which are computationally expensive to solve and made this approach unpractical.

In the sequential coupling strategy [27, 71, 110, 100, 34] the EMF process is divided into three sub-problems (electromagnetic, thermal and mechanical) and each field is evolved keeping the others fixed. Usually the process is considered adiabatic and it only alternates the solution of the electromagnetic and the mechanical equations. That is, the Lorentz forces are first calculated and then automatically transferred as input load to the mechanical model. The mechanical model deforms the workpiece and, thereafter, the geometry of the electromagnetic model is updated and so on. These iterations are repeated until the end of the EMF process. The advantages of this method is that it is very accurate and it can be made computationally efficient.

In the loose coupling strategy [58] the Lorentz forces are calculated neglecting the workpiece deformation. Then, they are transferred to the mechanical model which uses them as a driven force to deform the workpiece. This approach is less accurate than the former methods but it is computationally the most efficient and it can be very useful for estimating the order of magnitude of the parameters of an EMF process, for experimentation on modeling conditions or for modeling complex geometries. Also, it provides results as accurate as the other strategies when applied to small deformations or abrupt magnetic pressure pulses. In [3, 109, 50] it is shown a comparative performance of this approach with the sequential coupling strategy.

In this work we perform all the electromagnetic computations neglecting the workpiece deformation. This is done for clarity reasons and also because the results obtained with a static, un-deformed workpiece are useful for a rough estimation of the parameters involved in an EMF process. Moreover, the usual uncertainties in the knowledge of some parameters (mechanical properties of the workpiece, electrical properties of the RLC circuit, etc) can overshadow any improvement generated by the computationally more expensive sequential coupling.

On the other hand, if we have a precise knowledge of all the EMF parameters and we want to improve the accuracy of the simulations then, we can consider our results as the first step of a sequential coupling strategy. That is, we transfer the force calculated on the un-deformed workpiece to the mechanical model. The mechanical model deforms the workpiece until it reaches some prefixed value. Then, we input the new geometry into the electromagnetic model and so on.

In this sequential strategy is not necessary to solve the electromagnetic equations each time step. It is only necessary to solve them when the deformation of the workpiece produces appreciable changes in the electromagnetic parameters of the system coil-workpiece (inductance, resistance and Lorentz force). Therefore, we do not have to worry about numerical instabilities caused by a wrong choice of the time step.

5.3 Electromagnetic model

The electromagnetic model followed in the present work starts by solving the time-harmonic Maxwell's equations in a frequency interval. For each frequency ω we compute the electromagnetic fields inside a volume v containing the coil and the workpiece. With $\mathbf{E}(\mathbf{r}, \omega)$ and $\mathbf{H}(\mathbf{r}, \omega)$ we compute the inductance $L_{cw}(\omega)$ and the resistance $R_{cw}(\omega)$ of the system coil-workpiece. With $L_{cw}(\omega)$ and $R_{cw}(\omega)$ we obtain the intensity $I(t)$ flowing through the coil. Finally, with $I(t)$ and the magnetic field $\mathbf{H}(\mathbf{r}, \omega)$ on the surfaces of the workpiece we can calculate the Lorentz force that drives the EMF process.

In section 5.3.2 we explain how to compute the inductance $L_{cw}(\omega)$ and the resistance $R_{cw}(\omega)$ with the electromagnetic fields $\mathbf{E}(\mathbf{r}, \omega)$ and $\mathbf{H}(\mathbf{r}, \omega)$.

In section 5.3.4 we show how to obtain the intensity $I(t)$ with the calculated values of $L_{cw}(\omega)$ and $R_{cw}(\omega)$.

Finally, in sections 5.3.5 and 5.3.6 we compute the Lorentz force acting on the workpiece with the Fourier transform of $I(t)$ and $\mathbf{H}(\mathbf{r}, \omega)$.

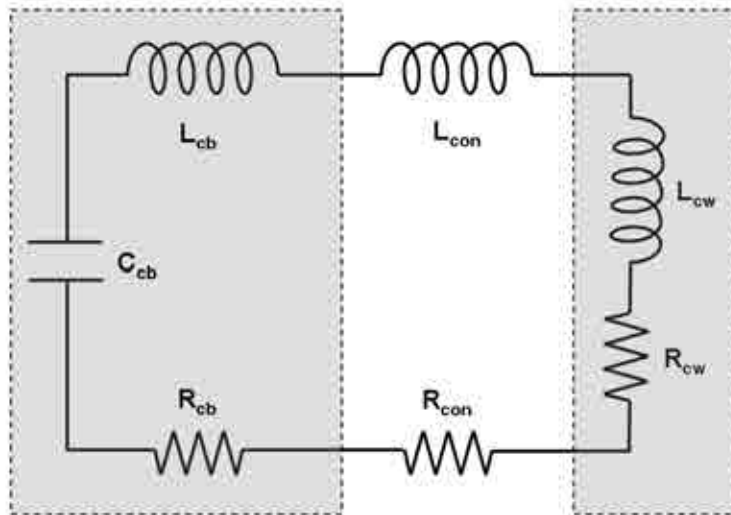


Figure 5.1: RLC circuit used to produce the discharge current. In the shadowed rectangle at the left is represented the capacitor bank with capacitance C_{cb} , inductance L_{cb} and resistance R_{cb} . In the shadowed rectangle at the right is represented the system formed by the coil and the metal workpiece. This system has an inductance L_{cw} and a resistance R_{cw} . Between both rectangles are represented the cables connecting the capacitor bank with the coil. These cables have an inductance L_{con} and a resistance R_{con} .

5.3.1 Input data

The input data required for computing the Lorentz force are:

- Geometry and material properties of the coil and the workpiece.
- Electrical parameters of the capacitor bank (capacitance C_{cb} , inductance L_{cb} , resistance R_{cb} and initial voltage V_0).
- Electrical parameters of the cables connecting the coil with the capacitor bank (inductance L_{con} and resistance R_{con}).

From the data in a) we calculate the inductance L_{cw} and the resistance R_{cw} of the system coil-workpiece as a function of the frequency ω . With $L_{cw}(\omega)$ and $R_{cw}(\omega)$ and the data in b) and c)

we find the intensity $I(t)$ flowing through the RLC circuit of fig. 5.1. Finally, with $I(t)$ and the magnetic field calculated with the data in a) we obtain the Lorentz force acting on the workpiece. In the following we analyze these steps in more detail.

5.3.2 Inductance and resistance of the system coil-workpiece

The repulsive force between the coil and the workpiece is a consequence of the time varying current $I(t)$ generated in the RLC circuit of fig. 5.1. To calculate $I(t)$ we first need the values of the inductance L_{cw} and the resistance R_{cw} . We do not take into account the capacitance of the system coil-workpiece because it is negligible in the geometries and at the frequencies usually involved in electromagnetic forming. The same is applicable to the capacitance of the cables connecting the coil with the capacitor bank.

We consider the set coil-workpiece as a generic, two-terminal, linear, passive electromagnetic system operating at low frequencies. We can imagine the coil and the workpiece inside a volume v with only its input terminals protruding. Under these assumptions, the inductance L_{cw} and the resistance R_{cw} at the frequency ω can be calculated with [42]

$$L_{cw}(\omega) = \frac{1}{|I_n|^2} \int_v \mu |\mathbf{H}(\mathbf{r}, \omega)|^2 dv, \quad (5.1)$$

$$R_{cw}(\omega) = \frac{1}{|I_n|^2} \int_v \sigma |\mathbf{E}(\mathbf{r}, \omega)|^2 dv \quad (5.2)$$

where I_n is the current injected into the system through the input terminals, μ is the magnetic permeability, $\mathbf{H}(\mathbf{r}, \omega)$ is the magnetic field, σ is the electrical conductivity and $\mathbf{E}(\mathbf{r}, \omega)$ is the electric field. The fields $\mathbf{E}(\mathbf{r}, \omega)$ and $\mathbf{H}(\mathbf{r}, \omega)$ are obtained after solving the time-harmonic Maxwell's equations at a given frequency ω . For each frequency ω we have a different value of L_{cw} and R_{cw} . The injected current I_n is a dummy variable that is only used to drive the problem. It can take any value without affecting the final result of (5.1) and (5.2).

5.3.3 Intensity in the RLC circuit

In fig. 5.1 is shown a typical RLC circuit used in electromagnetic forming. This circuit has a resistance R , an inductance L and a capacitance C given by

$$\begin{aligned} R &= R_{cb} + R_{con} + R_{cw}, \\ L &= L_{cb} + L_{con} + L_{cw}, \\ C &= C_{cb}. \end{aligned} \quad (5.3)$$

The values of R and L vary with time because of the deformation of the workpiece. In contrast, the capacitance C remain constant during all the forming process. The intensity $I(t)$ for all $t \in [0, \infty]$ flowing through the circuit of fig. 5.1 satisfies the differential equation

$$0 = \frac{d}{dt}(RI) + \frac{d}{dt}\left(L\frac{dI}{dt}\right) + \frac{1}{C}I, \quad (5.4)$$

with initial conditions $V(t_0) = V_0$ and $I(t_0) = 0$. The initial value V_0 represents the voltage at the terminals of the capacitor. This voltage is related with the energy of the discharge U_0 by

$$U_0 = \frac{1}{2}CV_0^2. \quad (5.5)$$

To find $I(t)$ with (5.4) we have to know first $R(t)$ and $L(t)$ for all $t \in [0, \infty]$.

If we consider a loose coupling strategy, the functions $R(t)$ and $L(t)$ are constants and equal to the values R_0 and L_0 calculated at the initial position with an un-deformed workpiece. Therefore, we have that $R(t) = R_0$ and $L(t) = L_0$ for all $t \in [0, \infty]$. Under these circumstances, the solution of (5.4) is given by

$$I(t) = \frac{V_0}{\omega_0 L_0} e^{-\gamma_0 t} \sin(\omega_0 t), \quad (5.6)$$

where

$$\omega_0 = 2\pi\nu_0 = \sqrt{\frac{1}{L_0 C} - \left(\frac{R_0}{2L_0}\right)^2} \quad (5.7)$$

and

$$\gamma_0 = \frac{R_0}{2L_0}. \quad (5.8)$$

If we consider a sequential coupling strategy then we solve (5.4) in time intervals $[t_i, t_{i+1}]$. This time intervals correspond with the time periods between two successive calls to the electromagnetic equations. We can assume that $L(t)$ and $R(t)$ are constants inside each $[t_i, t_{i+1}]$ and equal to the values R_i and L_i calculated with the deformed workpiece at t_i . In a sequential coupling strategy, the expression (5.6) is the solution of the first time interval $[t_0, t_1]$.

5.3.4 Capacitance and frequency

Equation (5.6) shows that if we want to know the intensity $I(t)$ we have to know first the values of ω_0 , C , V_0 , L_0 and R_0 . The capacitance C and the voltage V_0 are given data. The inductance L_0 and the resistance R_0 can be obtained with the help of (5.1), (5.2) and (5.3). The only value that remains unknown is ω_0 .

The frequency ω_0 is determined by the capacitance C_{cb} for a given set of coil, workpiece and connectors. The frequency ω_0 is the solution of the implicit equation

$$C_0(\omega) - C_{cb} = 0, \quad (5.9)$$

where the relation $C_0(\omega)$ is obtained after reordering expression (5.7)

$$C_0(\omega) = \frac{4L_0(\omega)}{4\omega^2 L_0(\omega)^2 + R_0(\omega)^2}. \quad (5.10)$$

In the case of using a sequential coupling strategy, we must take into account that the functions $L_i(\omega)$ and $R_i(\omega)$ are different in each $[t_i, t_{i+1}]$ and, as a consequence, the frequency ω_i is also different in each time interval.

5.3.5 Lorentz force on the workpiece

To calculate the electromagnetic force acting on the workpiece we made the following assumptions:

- i) The dimensions of the system coil-workpiece are small compared with the wavelength of the prescribed fields. The wavelengths involved in EMF are in the order of $\lambda \approx 10^3 - 10^5$ m with frequencies in the order of $\nu \approx 10^3 - 10^4$ Hz. As a consequence of this, we can consider the displacement current negligible $\partial \mathbf{D} / \partial t \approx 0$ and to treat the fields as if they propagated instantaneously with no appreciable radiation [103, 42].
- ii) The workpiece is linear, isotropic, homogeneous and non-magnetic ($\mu = \mu_0$). These properties represent all the workpieces used in this work (aluminium alloys). If we want to consider more complex materials, we must add to (5.11) the surface and volumetric integrals described in [103].
- iii) The modulus of the velocity at any point in the workpiece is always much less than $|\mathbf{v}| \ll 10^7$ m/s. In fact, the velocities involved in EMF are in the order of $|\mathbf{v}| \approx 10^2 - 10^3$ m/s. This circumstance allows us to neglect the velocity terms that appear in the Maxwell's equations when working with moving media [59].

Under hypothesis i)-iii) we can express the total force acting on the workpiece by [65]

$$\mathbf{F} = \int_v \mathbf{f}_v dv = \int_v (\mathbf{J} \times \mathbf{B}) dv, \quad (5.11)$$

where \mathbf{f}_v is a volumetric force density, $\mathbf{J} = \sigma \mathbf{E}$ is the current density induced in the workpiece and $\mathbf{B} = \mu_0 \mathbf{H}$ is the magnetic flux density. If we use the vector identity

$$\mathbf{B} \times \nabla \times \mathbf{B} = \nabla \left(\frac{1}{2} |\mathbf{B}|^2 \right) - (\mathbf{B} \cdot \nabla) \mathbf{B}, \quad (5.12)$$

and recalling that, by hypothesis i) and ii), the Ampere's circuital law is

$$\nabla \times \mathbf{B} = \mu_0 \mathbf{J}, \quad (5.13)$$

we can write the force density \mathbf{f}_v as

$$\mathbf{f}_v = -\nabla \left(\frac{1}{2\mu_0} |\mathbf{B}|^2 \right) + \frac{1}{\mu_0} (\mathbf{B} \cdot \nabla) \mathbf{B}. \quad (5.14)$$

In EMF the last term of the right hand side is usually negligible compared with the first. This is so because the field \mathbf{B} is almost unidirectional in the area of the workpiece just in front of the coil. In this area is where the main contribution to the total force is produced and also where the higher values of the Lorentz force are found. If a field \mathbf{B} is unidirectional then, by the Gauss law for magnetism ($\nabla \cdot \mathbf{B} = 0$), it will not change in the direction of \mathbf{B} . If a field \mathbf{B} only changes in the directions perpendiculars to \mathbf{B} then we have that $(\mathbf{B} \cdot \nabla) \mathbf{B} = 0$. In other words, to neglect the

last term of (5.14) is equivalent to neglect the compressive and expansive forces parallels to the workpiece surface and to state that, in EMF, the Lorentz force is due to the change in magnitude of the magnetic field along the thickness of the workpiece. Therefore, in EMF, we can simplify (5.14) to

$$\mathbf{f}_v \approx -\nabla \left(\frac{1}{2\mu_0} |\mathbf{B}|^2 \right). \quad (5.15)$$

Sometimes, the computational codes that solve the mechanical equations work more easily with pressures than with volumetric forces densities. In such cases, it is advantageous to express the force acting on the workpiece as a magnetic pressure applied on its surface. This magnetic pressure is the line integral of (5.15) from a point \mathbf{r}_0 placed on the workpiece surface nearest to the coil to a point \mathbf{r}_τ placed on the opposite side of the workpiece. The path to follow is a straight line with a direction defined by the surface normal at \mathbf{r}_0 . The magnetic pressure is then given by

$$P(\mathbf{r}_0, t) = \int_{\mathbf{r}_0}^{\mathbf{r}_\tau} \mathbf{f}_v \, ds = \frac{1}{2\mu_0} (|\mathbf{B}(\mathbf{r}_0, t)|^2 - |\mathbf{B}(\mathbf{r}_\tau, t)|^2), \quad (5.16)$$

which it can be also expressed as a function of \mathbf{H} recalling that, by hypothesis (ii), $\mathbf{B} = \mu_0 \mathbf{H}$

$$P(\mathbf{r}_0, t) = \frac{1}{2} \mu_0 (|\mathbf{H}(\mathbf{r}_0, t)|^2 - |\mathbf{H}(\mathbf{r}_\tau, t)|^2). \quad (5.17)$$

We can conclude from equation (5.17) that, under hypothesis i)-iii), we only need to know $|\mathbf{H}(\mathbf{r}, t)|$ on the surfaces of the workpiece to characterize electromagnetically the EMF process.

5.3.6 Lorentz force in frequency domain

The fields $\mathbf{H}(\mathbf{r}, t)$ of (5.17) can be represented in frequency domain using the inverse Fourier transform as follows

$$\mathbf{H}(\mathbf{r}, t) = \frac{1}{2\pi} \int_{-\infty}^{\infty} [\mathbf{H}_n(\mathbf{r}, \omega) I(\omega)] e^{i\omega t} d\omega, \quad (5.18)$$

where $i = \sqrt{-1}$ is the imaginary unit, $\mathbf{H}_n(\mathbf{r}, \omega)$ is the magnetic field per unit intensity at the frequency ω and $I(\omega)$ is the Fourier transform of the intensity $I(t)$ flowing through the RLC circuit

$$I(\omega) = \int_{-\infty}^{\infty} I(t) e^{-i\omega t} dt. \quad (5.19)$$

If the intensity $I(t)$ is given by (5.6) then the analytical expression of $I(\omega)$ is

$$I(\omega) = \frac{1}{2} \left(\frac{1}{\omega + \omega_0 - i\gamma_0} - \frac{1}{\omega - \omega_0 - i\gamma_0} \right), \quad (5.20)$$

where ω_0 is the frequency (5.7) and γ_0 is defined in (5.8). The magnetic field per unit intensity $\mathbf{H}_n(\mathbf{r}, \omega)$ is defined by

$$\mathbf{H}_n(\mathbf{r}, \omega) = \frac{\mathbf{H}(\mathbf{r}, \omega)}{I_n}, \quad (5.21)$$

where $\mathbf{H}(\mathbf{r}, \omega)$ and I_n are the same magnetic field and intensity as the ones appearing in (5.1).

We can write the Fourier transform of $\mathbf{H}(\mathbf{r}, t)$ as it is shown in (5.18) because, by hypothesis i) and ii), we are in the quasi-static regime and in the presence of linear materials. This implies that the magnetic field has almost a constant phase inside the system coil-workpiece and that it is linearly related with the current intensity. Also, it implies that the magnetic field and the current are in phase and, as a consequence, $\mathbf{H}_n(\mathbf{r}, \omega)$ is approximately a real number $\mathbf{H}_n(\mathbf{r}, \omega) \approx \text{Real}[\mathbf{H}_n(\mathbf{r}, \omega)]$. The advantage of using $\mathbf{H}_n(\mathbf{r}, \omega)$ is that we can know the magnetic field inside the system coil-workpiece for any value of the current intensity $I(\omega)$ once it is known for I_n .

5.4 Numerical analysis tools

Two different numerical tools are used to simulate the electromagnetic forming process. One solves the electromagnetic equations and the other solves the mechanical equations. The input data a)-c) (section 5.3.1) are provided to the electromagnetic code to obtain the magnetic pressure (5.17) on the surfaces of the workpiece. Afterwards, this magnetic pressure is provided to the mechanical code to obtain the deformation workpiece.

The electromagnetic equations are solved with the in-house code ERMES. The numerical formulation behind ERMES is explained in detail in chapter 3. Its main features and user manual are the objective of appendix A.

The mechanical equations are solved with the commercial software STAMPAK [102]. This numerical tool has been applied to processes such as ironing, necking, embossing, stretch-forming, forming of thick sheets, flex-forming, hydro-forming, stretch-bending of profiles, etc. It can solve dynamic problems with high speeds and large strains rates, obtaining explicitly accelerations, velocities and deformations. In this work, our emphasis is on the electromagnetic part of the EMF process, then, we do not go further into the numerical formulation behind STAMPAK. For a detailed information about this formulation see [11].

5.5 Application example I. Sheet bulging.

In this section we apply the electromagnetic model explained above to the EMF process presented in [105]. This process consists in the free bulging of a thin metal sheet by a spiral flat coil. Our objective is to find the magnetic pressure acting on the workpiece for the given value of the capacitance $C_{cb} = 40 \mu\text{F}$ and the initial voltage $V_0 = 6 \text{ kV}$.

5.5.1 Description of the system coil-workpiece

The spiral flat coil appearing in [105] can be approximated by coaxial loop currents in a plane. Thus, the problem can be considered axis symmetric. The dimensions of the coil and the workpiece are shown in fig. 5.2. The diameter of the wire, material properties and horizontal positioning of the coil are missed in [105]. We used the values given in [27], where the same problem is treated and it is provided a complete description of the geometry.

The coil is made of copper with an electrical conductivity of $\sigma = 58e6$ S/m. The workpiece is a circular plate of annealed aluminum JIS A 1050 with an electrical conductivity of $\sigma = 36e6$ S/m. It is assumed $\epsilon = \epsilon_0$ and $\mu = \mu_0$ in the coil and in the workpiece.

The RLC circuit has an inductance $L_{cb} + L_{con} = 2.0$ μ H, a resistance $R_{cb} + R_{con} = 25.5$ m Ω and a capacitance $C_{cb} = 40$ μ F. The capacitor bank was initially charged with a voltage of $V_0 = 6$ kV.

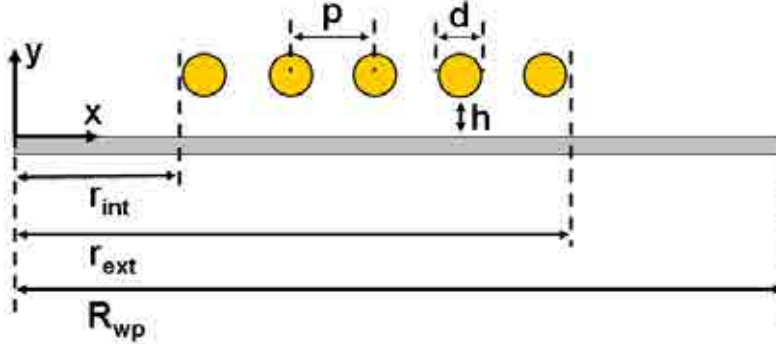


Figure 5.2: Dimensions of the system coil-workpiece. Data taken from [105, 27]. Number of turns of the coil $N = 5$. Pitch or coil separation $p = 5.5$ mm. Diameter of the coil wires $d = 1.29$ mm (16 AWG). Maximum coil radius $r_{ext} = 32$ mm. Minimum coil radius $r_{int} = 8.71$ mm. Separation distance between coil and metal sheet $h = 1.6$ mm. Thickness of the sheet $\tau = 0.5$ mm. Radius of the workpiece $R_{wp} = 55$ mm.

5.5.2 Finite element model

Although, undoubtedly, in this case the best option is to perform the computations with an axis symmetric two-dimensional computational tool, we used the in-house three-dimensional code ERMES. The advantages are that we do not need to build a new tool and that we can solve more general situations with the same software and the same file exchange interface between ERMES and STAMPAK. On the other hand, for this specific problem, our tools are computationally less efficient.

We employed the geometry shown in fig. 5.3 to compute the electromagnetic fields with ERMES. The geometry is a truncated portion of a sphere with an angle of 20° . We drive the problem with a current density \mathbf{J} uniformly distributed in the volume of the coil wires. In the colored surfaces of fig. 5.3 we imposed the regularized perfect electric conductor (PEC) boundary conditions (see chapter 3)

$$\begin{aligned}\nabla \cdot (\epsilon \mathbf{E}) &= 0, \\ \hat{\mathbf{n}} \times \mathbf{E} &= 0.\end{aligned}\tag{5.22}$$

It is not necessary to impose more boundary condition if we apply in all the FEM nodes of the domain a change of coordinates from cartesian (E_x, E_y, E_z) to axis symmetric around the Y axis

(E_ρ, E_φ, E_y) . That is, at the same time we are building the matrix, we enforce at each node of the FEM mesh the following

$$\begin{pmatrix} E_\rho \\ E_\varphi \\ E_y \end{pmatrix} = \begin{pmatrix} x/\rho & 0 & z/\rho \\ -z/\rho & 0 & x/\rho \\ 0 & 1 & 0 \end{pmatrix} \begin{pmatrix} E_x \\ E_y \\ E_z \end{pmatrix} \quad (5.23)$$

where x and z are the cartesian coordinates of the node and $\rho = \sqrt{x^2 + z^2}$. We preserve the symmetry of the final FEM matrix applying (5.23) and its transpose as it is explained in [7].

The advantage of using (5.23) is that $E_\rho = 0$ and $E_y = 0$ in axis symmetric problems. This fact reduces by a factor of three the size of the final matrix and also the time required to solve it. Therefore, we can improved noticeably the computational performance of ERMES in axis symmetric problems with a simple modification of its matrix building procedure. In a desktop computer with a CPU Intel Core 2 Quad Q9300 at 2.5 GHz and the operative system Microsoft Windows XP, ERMES requires less than 30 s and less than 500 MB of memory RAM to solve each frequency.

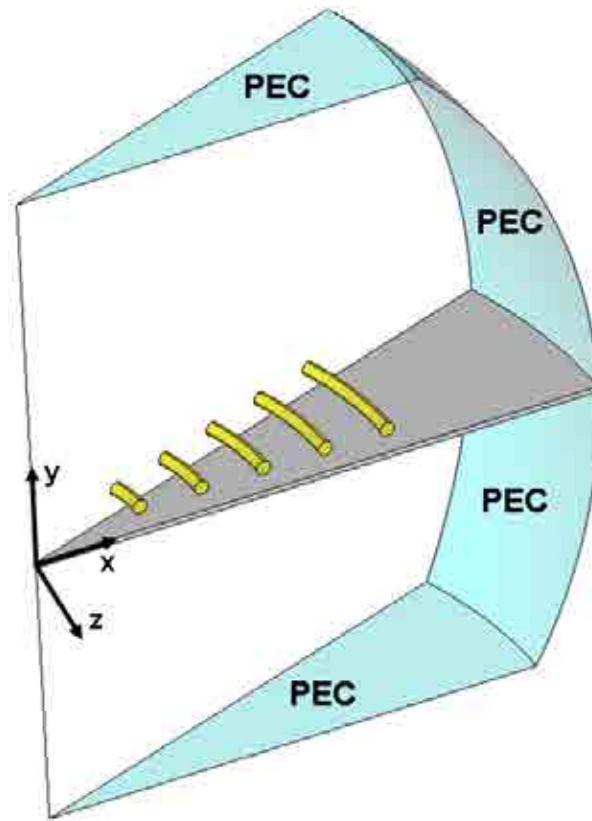


Figure 5.3: Geometry used in ERMES to compute the electromagnetic fields in the free bulging process of a thin metal sheet by a spiral flat coil.

5.5.3 Intensity through the RLC circuit

Once the initial geometry of system coil-workpiece is properly characterized, we have to find the intensity $I(t)$ flowing through the RLC circuit. As it is mentioned in section 5.3.4, if we want to know $I(t)$ we have to calculate first the frequency ω_0 . This frequency ω_0 is the solution of equation (5.9) with $C_{cb} = 40 \mu\text{F}$. We solved (5.9) using the following iterative procedure:

- 1) We replace in $C_0(\omega)$ the frequency which satisfies $\delta = \tau$, where τ is the thickness of the workpiece and δ is the skin depth

$$\delta = \sqrt{\frac{1}{\pi\nu\mu\sigma}}. \quad (5.24)$$

- 2) We compare $C_0(\omega)$ with C_{cb} . If $C_0(\omega) > C_{cb}$ then we must increase the value of ω . If $C_0(\omega) < C_{cb}$ then we must decrease the value of ω . If $C_0(\omega) = C_{cb}$ then we have found the solution ω_0 .
- 3) If the solution is not achieved then we replace in $C_0(\omega)$ the new incremented/decremented value of ω and go to step 2). The procedure is repeated until the solution is achieved.

In fig. 5.4 is shown the capacitance C_0 as a function of the frequency ν and the solution $\nu_0 = 16.35 \text{ kHz}$ for the given capacitance $C_{cb} = 40 \mu\text{F}$. We have choose an initial frequency satisfying $\delta = \tau$ because we have observed in the literature that the typical frequencies employed in EMF lay in the interval

$$0.5 < \frac{\delta}{\tau} < 1.5. \quad (5.25)$$

In the present case, we have that the skin depth is $\delta = 1.3 \tau$.

As it is indicated in equation (5.10), we need to know $L_0(\omega)$ and $R_0(\omega)$ to calculate $C_0(\omega)$. These functions are defined in (5.3) and they represent the total inductance and the total resistance of the RLC circuit of fig. 5.1. We assume that the given values $L_{cb} + L_{con} = 2.0 \mu\text{H}$ and $R_{cb} + R_{con} = 25.5 \text{ m}\Omega$ do not change with the frequency. On the other hand, L_{wp} and R_{wp} are frequency dependant and they have to be calculated with the help of (5.1) and (5.2). In the volume of the coil, equation (5.2) is replaced by

$$R_{cw}(\omega) = \frac{1}{|I_n|^2} \int_v \frac{|\mathbf{J}|^2}{\sigma} dv \quad (5.26)$$

where \mathbf{J} is the imposed current density and σ is the conductivity of the coil. We recall that if we want to obtain a volume integral for all the space then we must multiply by 18 ($=360^\circ/20^\circ$) any volume integral calculated in the portion of truncated sphere of fig. 5.3. The values of the total inductance L_0 and the total resistance R_0 as a function of the frequency ν are shown in fig. 5.5 and in fig. 5.6.

If we substitute in equation (5.6) the calculated values of $\omega_0 = 2\pi\nu_0$, $L_0(\omega_0) = 2.35 \mu\text{H}$ and $R_0(\omega_0) = 38.1 \text{ m}\Omega$ and the given values of C_{cb} and V_0 then we obtain the intensity $I(t)$ flowing through the coil. In fig. 5.7 we compare the intensity calculated in [105] with the intensity calculated in this work.

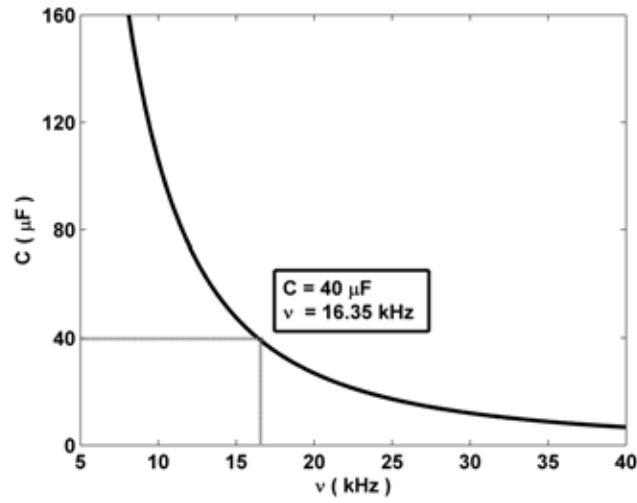


Figure 5.4: Capacitance C_0 as a function of the frequency ν for the un-deformed workpiece placed in its initial position. The function $C_0(\nu)$ is obtained from equation (5.10). If the capacitor bank has a $C_{cb} = 40 \mu\text{F}$ the oscillation frequency of the RLC circuit is $\nu_0 = 16.35 \text{ kHz}$.

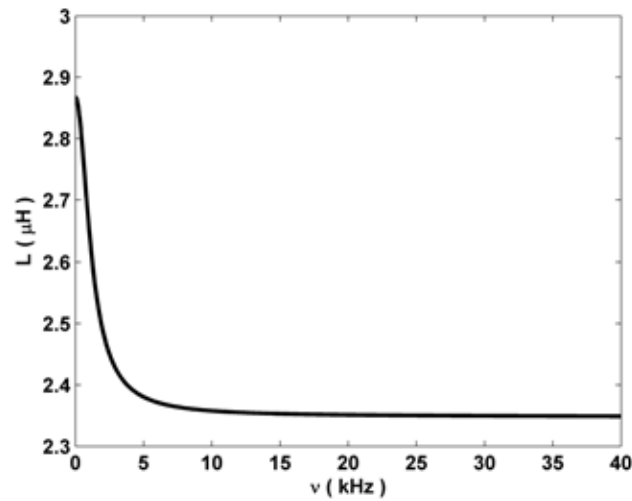


Figure 5.5: Total inductance $L_0 = L_{cb} + L_{con} + L_{cw}$ as a function of the frequency ν for the un-deformed workpiece placed in its initial position. The inductance of the system coil-workpiece L_{cw} is calculated with the equation (5.1). The value of L_{cw} varies from $0.86 \mu\text{H}$ at the lower frequencies to $0.35 \mu\text{H}$ at the higher frequencies. We assumed that the inductance of the exterior circuit $L_{cb} + L_{con} = 2.0 \mu\text{H}$ remains constant in this frequency band.

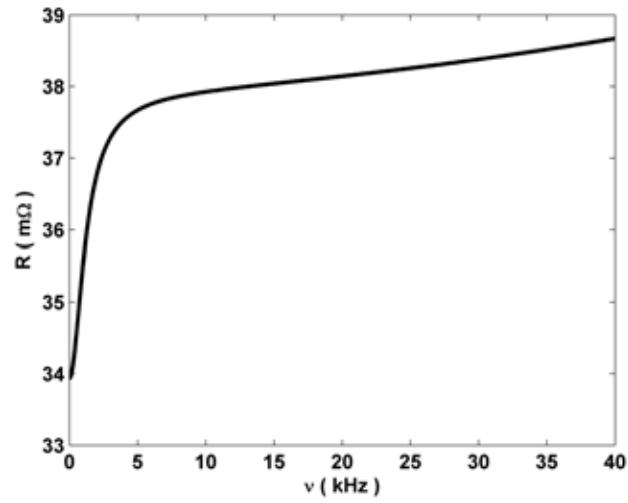


Figure 5.6: Total resistance $R_0 = R_{cb} + R_{con} + R_{cw}$ as a function of the frequency ν for the un-deformed workpiece placed in its initial position. The resistance of the system coil-workpiece R_{cw} is calculated with equation (5.2) in the volume of the workpiece and with equation (5.26) in the volume of the coil. The value of R_{cw} varies from 8.4 m Ω at the lower frequencies to 13.2 m Ω at the higher frequencies. We assumed that the resistance of the exterior circuit $R_{cb} + R_{con} = 25.5$ m Ω remains constant in this frequency band.

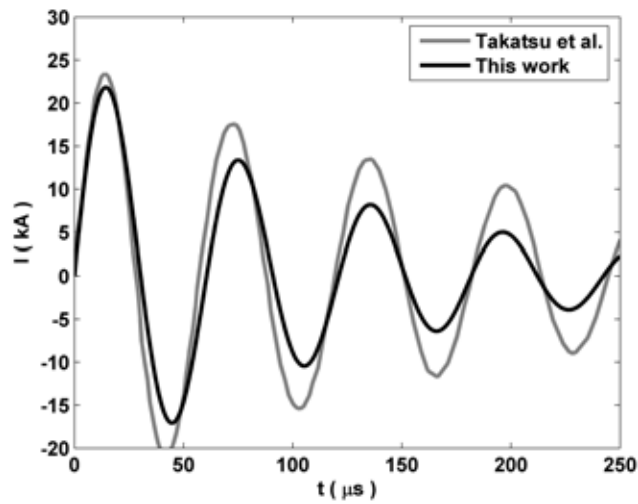


Figure 5.7: Intensity calculated in Takatsu et al. [105] compared with the intensity calculated in this work. We have graphed expression (5.6) with $V_0 = 6$ kV, $C_{cb} = 40$ μ F, $\nu_0 = 16.35$ kHz, $\omega_0 = 2\pi\nu_0$, $L_0 = 2.35$ μ H and $R_0 = 38.1$ m Ω .

5.5.4 Magnetic pressure on the workpiece

If we want to calculate the magnetic pressure (5.17) acting on the workpiece then we need the fields $\mathbf{H}(\mathbf{r}_0, t)$ and $\mathbf{H}(\mathbf{r}_\tau, t)$, where \mathbf{r}_0 is located on the surface of the workpiece nearest to the coil (S_0) and \mathbf{r}_τ is located on the surface of the workpiece farthest to the coil (S_τ). The fields $\mathbf{H}(\mathbf{r}_0, t)$ and $\mathbf{H}(\mathbf{r}_\tau, t)$ are obtained from (5.18) with the Fourier transform of $I(t)$ and the magnetic fields per unit intensity $\mathbf{H}_n(\mathbf{r}_0, \omega)$ and $\mathbf{H}_n(\mathbf{r}_\tau, \omega)$. In fig. 5.8 are shown $|\mathbf{H}_n(\mathbf{r}_0, \omega)|$ and $|\mathbf{H}_n(\mathbf{r}_\tau, \omega)|$ as a function of the frequency ν . In fig. 5.9 are shown $|\mathbf{H}_n(\mathbf{r}_0, \omega) I(\omega)|$, $|\mathbf{H}_n(\mathbf{r}_0, \omega) I(\omega)|$ and $|\mathbf{H}_n(\mathbf{r}_\tau, \omega) I(\omega)|$ as a function of the frequency ν . It can be shown (see fig. 5.9) that, in this EMF process, we have

$$\begin{aligned} \mathbf{H}_n(\mathbf{r}_0, \omega) I(\omega) &\approx \mathbf{H}_n(\mathbf{r}_0, \omega) I(\omega), \\ |\mathbf{H}_n(\mathbf{r}_0, \omega) I(\omega)| &\gg |\mathbf{H}_n(\mathbf{r}_\tau, \omega) I(\omega)|. \end{aligned} \quad (5.27)$$

If we use (5.27) in (5.18) and (5.17) then we can write the magnetic pressure $P(\mathbf{r}_0, t)$ as

$$P(\mathbf{r}_0, t) = \frac{1}{2} \mu_0 |\mathbf{H}_n(\mathbf{r}_0, \omega) I(t)|^2. \quad (5.28)$$

This simplification of (5.17), which is possible when (5.27) is accomplished, is very useful in a sequential coupling strategy. This is so because, in the next calls to the electromagnetic model, we will only need to find the magnetic field for one frequency, which makes the computations more efficient.

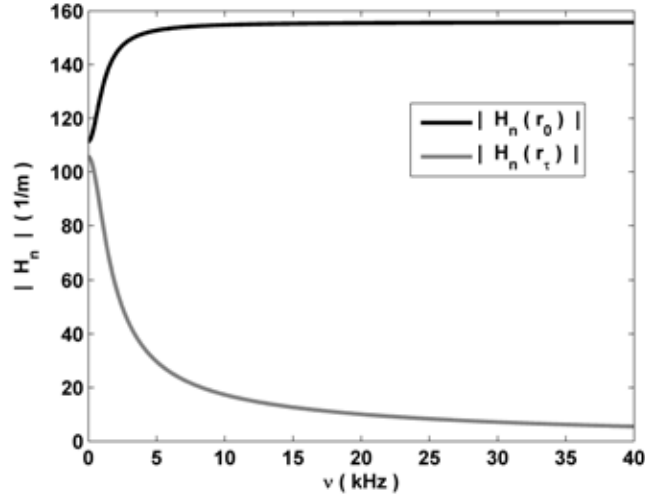


Figure 5.8: Modulus of the magnetic fields per unit intensity $|\mathbf{H}_n(\mathbf{r}_0, \omega)|$ and $|\mathbf{H}_n(\mathbf{r}_\tau, \omega)|$ as a function of the frequency ν . The point \mathbf{r}_0 is located on S_0 . The point \mathbf{r}_τ is located on S_τ , on the opposite side of where \mathbf{r}_0 is placed.

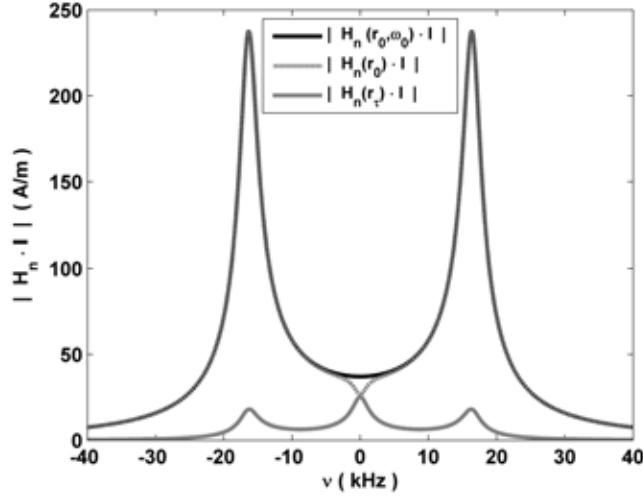


Figure 5.9: Modulus of the magnetic fields $|\mathbf{H}_n(\mathbf{r}_0, \omega_0) I(\omega)|$, $|\mathbf{H}_n(\mathbf{r}_0, \omega) I(\omega)|$ and $|\mathbf{H}_n(\mathbf{r}_\tau, \omega) I(\omega)|$ as a function of the frequency ν . The constant $\mathbf{H}_n(\mathbf{r}_0, \omega_0)$ is the magnetic field per unit intensity at the frequency ω_0 in the point \mathbf{r}_0 . The point \mathbf{r}_0 is located on S_0 . The function $I(\omega)$ is the Fourier transform of the intensity $I(t)$. The analytical expression of $I(\omega)$ is given by (5.20). The function $\mathbf{H}_n(\mathbf{r}_0, \omega)$ is the magnetic field per unit intensity at the point \mathbf{r}_0 . The function $\mathbf{H}_n(\mathbf{r}_\tau, \omega)$ is the magnetic field per unit intensity at the point \mathbf{r}_τ . The point \mathbf{r}_τ is located on S_τ , on the opposite side of where \mathbf{r}_0 is placed. In this graph we can see that $|\mathbf{H}_n(\mathbf{r}_0, \omega_0) I(\omega)| \approx |\mathbf{H}_n(\mathbf{r}_0, \omega) I(\omega)|$ and $|\mathbf{H}_n(\mathbf{r}_0, \omega_0) I(\omega)| \gg |\mathbf{H}_n(\mathbf{r}_\tau, \omega) I(\omega)|$.

In fig. 5.10 is shown the total magnetic force acting on the workpiece as a function of time. The total magnetic force is the integral of the function (5.28) over the whole surface S_0 . We computed the total force using (5.28) with $\mathbf{H}_n(\mathbf{r}_0, \omega_0)$ and $I(t)$ calculated for the un-deformed workpiece placed in its initial position.

In fig. 5.11 is shown the radial distribution of the magnetic pressure (5.28) when the coil current reaches its maximum $I_{max} = 21.83 \text{ kA}$ at $t = 14.5 \mu\text{s}$. In fig. 5.11 is also shown the magnetic pressure obtained in [105] when the coil current calculated there reaches its maximum at $t = 15.4 \mu\text{s}$. In fig. 5.11 we see that, apart from a difference in the positioning of the coil, there is a difference in the magnitude of the magnetic pressure. The same difference is also observed in [101, 100], where this EMF process is simulated using two different approaches. One is based on FDTD (Finite Difference Time Domain) and the other on FEM (Finite Element Method). In the FDTD approach they used a similar procedure to that employed in [105]. In the FEM approach they used the freeware software FEMM4.0 [26]. In fig. 5.12 and fig. 5.13 we show the components of the magnetic flux density B_ρ and B_y calculated with FEMM4.0, FDTD and ERMES when the coil current is $I = 20.81 \text{ kA}$. In these figures we see that the results given by both FEM codes are similar between them but different from the results given by the FDTD method.

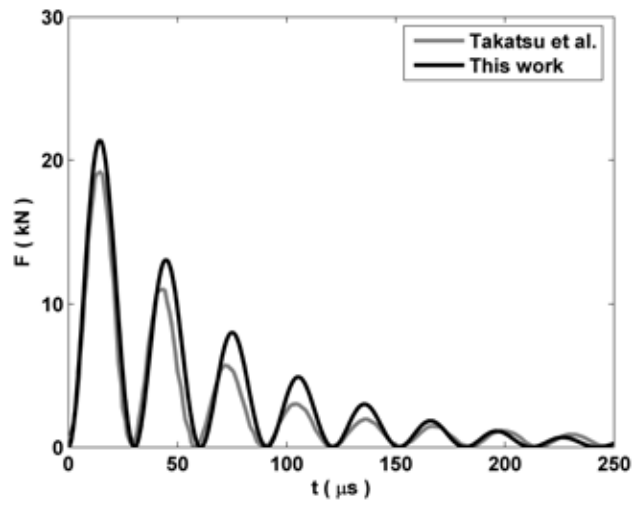


Figure 5.10: Total magnetic force calculated in Takatsu et al. [105] compared with the total magnetic force calculated in this work.

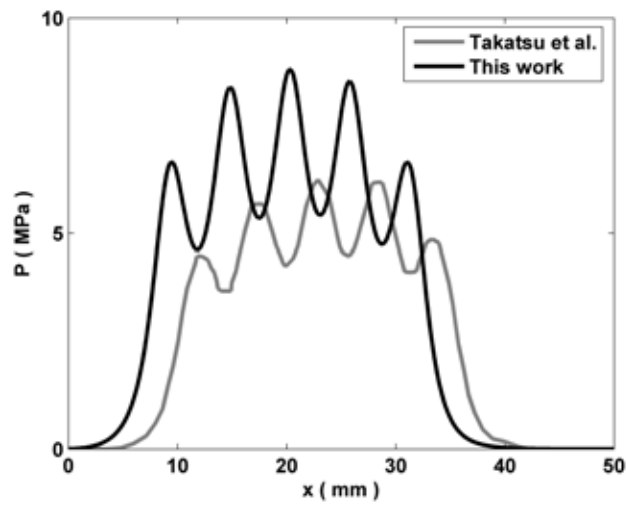


Figure 5.11: Radial distribution of the magnetic pressure calculated in Takatsu et al. [105] when the coil current reaches its maximum ($t = 15.4 \mu s$) compared with the radial distribution of the magnetic pressure calculated in this work ($I_{max} = 21.83 \text{ kA}$ at $t = 14.5 \mu s$).

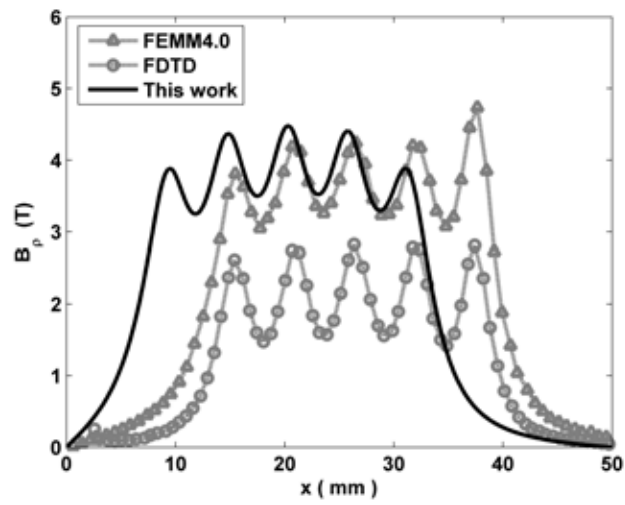


Figure 5.12: Radial component of the magnetic flux density calculated in [101] with FEM (FEMM4.0) and FDTD compared with the radial component of the magnetic flux density calculated in this work with ERMES.

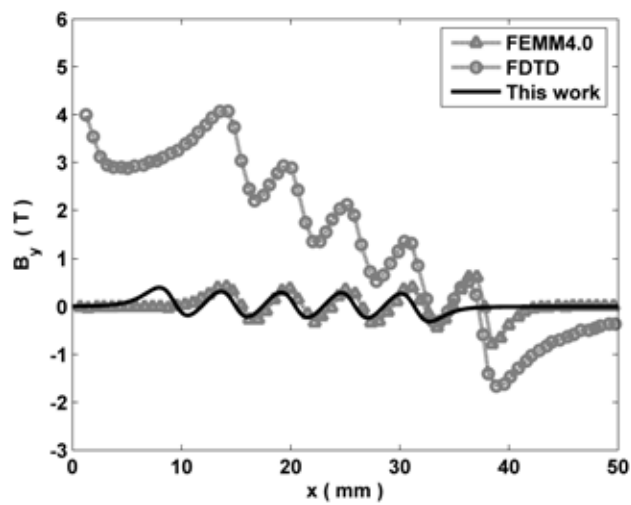


Figure 5.13: Axial component of the magnetic flux density calculated in [101] with FEM (FEMM4.0) and FDTD compared with the axial component of the magnetic flux density calculated in this work with ERMES.

The differences between the FDTD and the FEM approaches can be attributed to the use of a coarse mesh in the FDTD method. To show this, we solved a problem similar to the one appearing in this section (see fig. 5.2) but with a fixed workpiece of thickness $\tau = 3.0$ mm, gap distance $h = 2.9$ mm and initial voltage $V_0 = 2$ kV. We calculated in this set-up the radial component of the magnetic flux density B_ρ . Then, we compared our results with the simulations performed in [100] for different FDTD mesh sizes and also with the measurements of [105] (see fig. 5.14).

In fig. 5.14 we see that when the FDTD mesh is coarse (6 elements along the thickness of the sheet) the results of the FDTD simulations are in good agreement with the measurements but they are different from the results obtained with ERMES. On the hand, if we improve the FDTD mesh to 20 elements along the thickness of the sheet, the results of the FDTD simulations are similar to the results obtained with ERMES but they are different from the measurements. This unusual behavior can be explained if we consider that R_{con} and L_{con} are undervalued. If we add, for instance, only 1 meter of 16 AWG copper wire ($R_{1m} = 13.2$ m Ω , $L_{1m} = 1.5$ μ H [32]) to the total resistance and the total inductance of the RLC circuit then, the results obtained with ERMES, and with the improved FDTD mesh, are in agreement with the measurements and also with the fact that improving the mesh must improve the results.

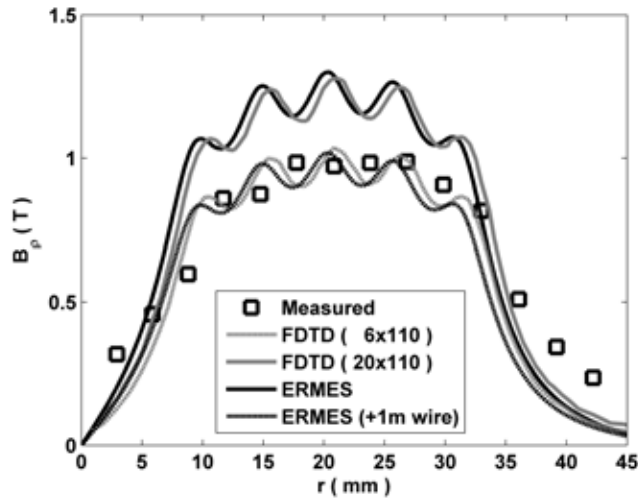


Figure 5.14: Radial component of the magnetic flux density B_ρ for the coil of fig. 5.2 with a fixed workpiece of thickness $\tau = 3.0$ mm, gap distance $h = 2.9$ mm and initial voltage $V_0 = 2$ kV. Measurements are from [105]. FDTD (6x110) represents the simulations performed in [100] with a FDTD mesh of 6 elements along the thickness of the sheet and 110 elements along the radial direction. FDTD (20x110) represents the simulations performed in [100] with a FDTD mesh of 20 elements along the thickness of the sheet and 110 elements along the radial direction. ERMES represents the simulations performed in this work. ERMES (+1m wire) represents the simulations performed in this work adding the DC resistance and the inductance of 1 meter of 16 AWG copper wire ($R_{1m} = 13.2$ m Ω , $L_{1m} = 1.5$ μ H [32]) to the total inductance and the total resistance of the RLC circuit.

5.5.5 Deflection of the workpiece

We introduced in STAMPACK the magnetic pressure calculated in section 5.5.4 to obtain the deflection of the metal sheet. STAMPACK interprets the magnetic pressure as a mechanical pressure which deforms the workpiece. The results are shown in fig. 5.15.

In STAMPACK is not available the mechanical model used in [105]. Therefore, we had to adapt the parameters of the available model to reproduce the behavior of the material used in [105]. We considered the workpiece as an aluminium alloy with a Young's modulus $E = 69$ GPa, density $\rho = 2700$ Kg/m³ and Poisson's ratio $\nu = 0.33$. STAMPACK used the Voce hardening law

$$\sigma_{cs} = \sigma_{y0} + (\sigma_m - \sigma_{y0}) (1 - e^{-n\varepsilon_{ps}}), \quad (5.29)$$

where σ_{cs} is the Cauchy stress, $\sigma_{y0} = 34.9$ MPa is the yielding tensile strength, $\sigma_m = 128.8$ MPa is the ultimate tensile strength, $n = 12.0$ is the isotropic hardening parameter and ε_{ps} is the effective plastic deformation. STAMPACK also used a damping proportional to the nodal velocity ($\mathbf{F}_i = -\eta_i \mathbf{v}_i$) with $\eta_i = 2\alpha M_i$, being $\alpha = 138.6$ and M_i the lumped mass at the i -th node. The constant parameters of the mechanical model were obtained introducing in STAMPACK the magnetic pressure calculated in [105]. Then, we adjusted the parameters until achieve with STAMPACK the same deflection of the disk as the one measured in [105].

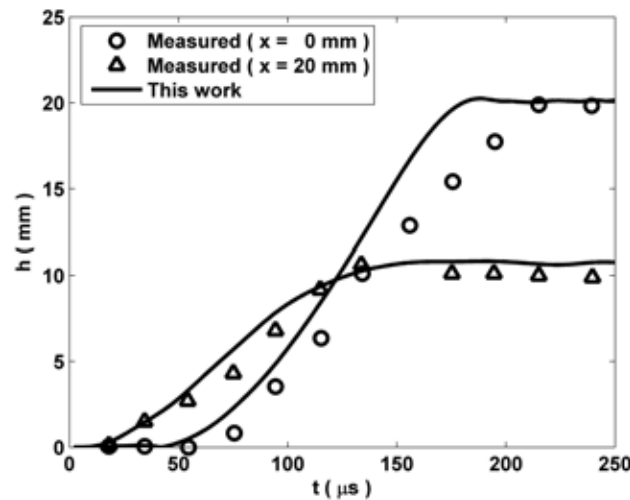


Figure 5.15: Deflection of the workpiece at the positions $x = 0$ mm and $x = 20$ mm as a function of time. The results of this work are compared with the measurements of Takatsu et al. [105].

5.6 Application example II. Tube bulging.

In this section we apply the electromagnetic model of section 5.3 to the EMF process presented in [117]. This process consists in the expansion of a cylindrical tube by a solenoidal coil. In [117] is analyzed the tube bulging process under different working conditions but, here, our objective is to find the magnetic pressure acting on the workpiece when the capacitance is $C_{cb} = 160 \mu\text{F}$, the coil length is $\ell = 200 \text{ mm}$ and the initial charging energy is $U_0 = 2 \text{ kJ}$.

5.6.1 Description of the system coil-workpiece

We take the geometrical description of the solenoidal coil and the tubular workpiece from [117]. The coil is approximated by coaxial loop currents, concentric with the workpiece and placed inside it. Thus, the problem is considered axis symmetric.

The coil is made of $d = 2.0 \text{ mm}$ diameter copper wire. The outer diameter of the coil is $D_c = 37.0 \text{ mm}$. The separation between each loop is $p = 3.0 \text{ mm}$. The length of the coil is approximately $\ell = 200 \text{ mm}$ and the number of turns is $N = 68$. We assume an electrical conductivity for copper of $\sigma = 58e6 \text{ S/m}$.

The workpiece is a cylindrical tube made of annealed aluminum A1050TD with an outer diameter $D_{wp} = 40.0 \text{ mm}$ and a thickness of $\tau = 1.0 \text{ mm}$. We assume an electrical conductivity for the workpiece of $\sigma = 36e6 \text{ S/m}$. We also assume that $\epsilon = \epsilon_0$ and $\mu = \mu_0$ for workpiece and coil.

In [117] is said that $L_{cb} + L_{con}$ and $R_{cb} + R_{con}$ are less than $1.0 \mu\text{H}$ and $2.0 \text{ m}\Omega$ respectively. But, in [65], where it is used an EMF set-up similar to that used in [117], it is reached to the conclusion that these quantities underestimate the inductance and the resistance of the wires connecting the capacitor bank with the coil. In [65] is found that $L_{cb} + L_{con} = 2.5 \mu\text{H}$ and $R_{cb} + R_{con} = 15.0 \text{ m}\Omega$ are more realistic values. In this work we employ the $L_{cb} + L_{con}$ and $R_{cb} + R_{con}$ given in [65].

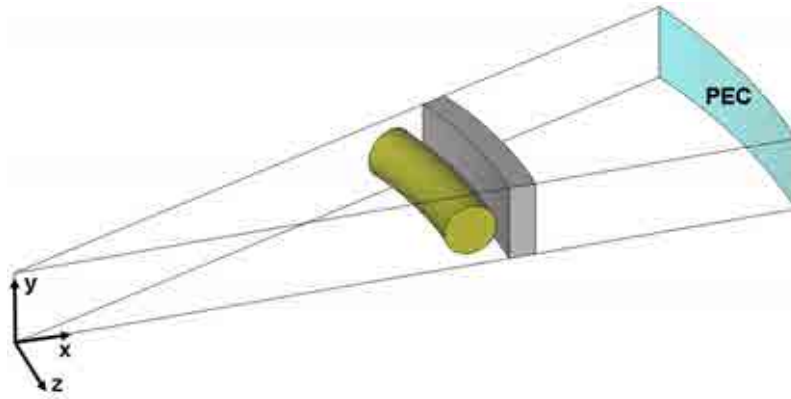


Figure 5.16: Geometry used in ERMES to compute the electromagnetic fields of the tube bulging process analyzed in [117].

5.6.2 Finite element model

The FEM model used for the tube bulging process is similar to that described in section 5.5.2. We computed the fields $\mathbf{E}(\mathbf{r}, \omega)$ and $\mathbf{H}(\mathbf{r}, \omega)$ in the geometry of fig. 5.16. The geometry represents a truncated portion of one turn of the coil with an angle of 20° . The problem is driven by a current density uniformly distributed in the volume of the wire. We applied the PEC boundary condition (6.6) in the colored surface of fig. 5.16. We imposed the change of coordinates explained in section 5.5.2 at each node of the FEM mesh. One of the advantages of using the geometry of fig. 5.16 is that we can obtain L_{wp} and R_{wp} for any coil length. We only need to multiply the integrals (5.1) and (5.2) performed in the volume of fig. 5.16 by $N \cdot (360^\circ/20^\circ)$, where N is the number of turns of the coil.

5.6.3 Intensity through the RLC circuit

We follow the steps given in section 5.5.3 to compute the intensity flowing through the coil of length $\ell = 200$ mm ($N = 68$ turns) when the capacitance is $C_{cb} = 160 \mu\text{F}$ and the initial charging energy is $U_0 = 2$ kJ. We found that $\nu_0 = 4.6$ kHz, $V_0 = 5$ kV, $L_0 = 6.9 \mu\text{H}$ and $R_0 = 101.1$ m Ω , being $L_0 = L_{cb} + L_{con} + L_{cw}$ and $R_0 = R_{cb} + R_{con} + R_{cw}$.

In [117] is measured the maximum current intensity for several coil lengths and capacitances C_{cb} when the initial charging energy is $U_0 = 1$ kJ. In fig. 5.17 we compare these measurements with the results of this work.

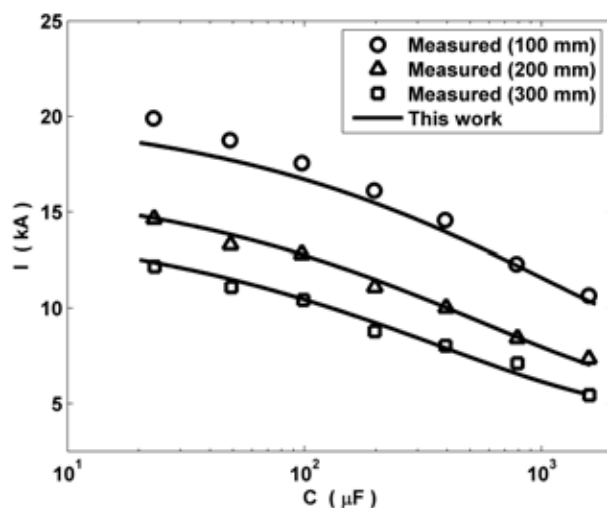


Figure 5.17: Maximum current intensity for several coil lengths and capacitances C_{cb} . The initial charging energy is $U_0 = 1$ kJ in all the cases. The measurements from [117] are compared with the results of this work.

5.6.4 Magnetic pressure on the workpiece

In fig. 5.18 we show the modulus of the magnetic fields $|\mathbf{H}_n(\mathbf{r}_0, \omega_0) I(\omega)|$, $|\mathbf{H}_n(\mathbf{r}_0, \omega) I(\omega)|$ and $|\mathbf{H}_n(\mathbf{r}_\tau, \omega) I(\omega)|$ as a function of the frequency ν , where the notation used here is the same as in section 5.5.4. In this case we can not apply the approximations (5.27) and (5.28) and we must employ the equations (5.18) and (5.17) to calculate the magnetic pressure acting on the workpiece.

In fig. 5.19 we show the magnetic pressure calculated in this work compared with the magnetic pressure calculated in [117]. We had to average the magnetic pressure over the surfaces of the workpiece to compare our results with those provided by [117].

The differences shown in fig. 5.19 can be attributed to the features of each electromagnetic model. In [117] is considered the movement of the workpiece, assumed a uniform current density along all the the length of the coil and an exponential decay of the magnetic field from the inner surface to the outer surface of the metallic tube. On the other hand, we neglected the workpiece deformation, considered a more realistic coil geometry and calculated numerically the magnetic field on the surfaces of the metallic tube.

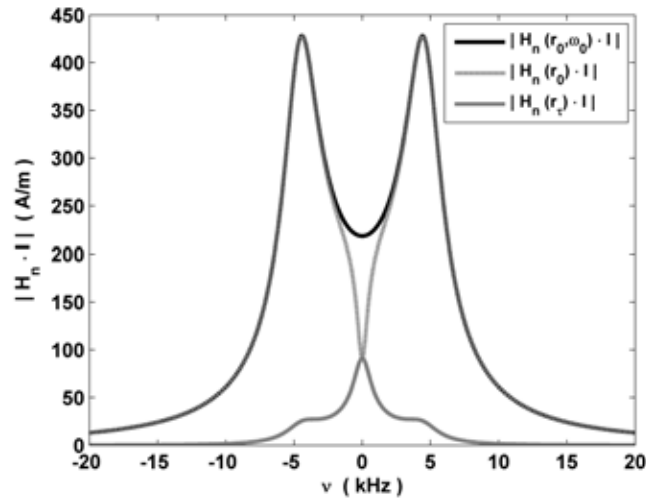


Figure 5.18: Modulus of the magnetic fields $|\mathbf{H}_n(\mathbf{r}_0, \omega_0) I(\omega)|$, $|\mathbf{H}_n(\mathbf{r}_0, \omega) I(\omega)|$ and $|\mathbf{H}_n(\mathbf{r}_\tau, \omega) I(\omega)|$ as a function of the frequency ν .

5.6.5 Deflection of the workpiece

We calculated the expansion of the workpiece using the mechanical model explained in section 5.5.5. The material properties and constant parameters are the same as in section 5.5.5 except for the damping coefficient α , which now is $\alpha = 693.1$.

The parameters of the mechanical model were obtained by introducing in STAMPAK the magnetic pressure calculated in [117]. Then, we adjusted the parameters until reproduce the forming velocity given in [117].

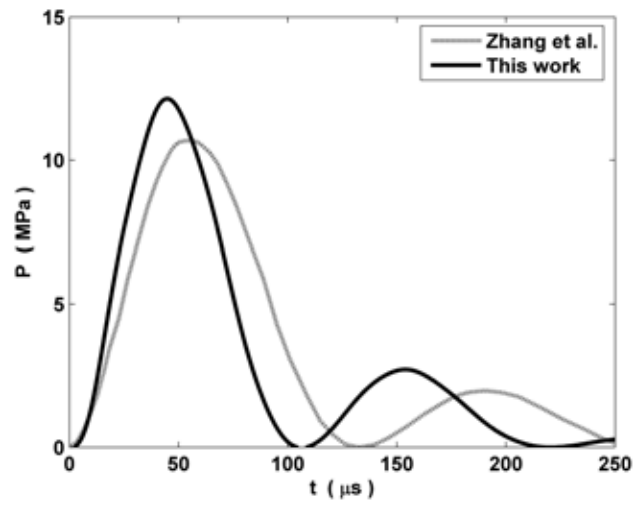


Figure 5.19: Magnetic pressure calculated by Zhang et al. [117] compared with the magnetic pressure calculated in this work.

In fig. 5.20 we compare the deflection of the workpiece deduced from [117] with the deflection of the workpiece calculated in this work. In [117] is not provided the deflection of the workpiece, we obtained it by integrating in time the forming velocity facilitated there.

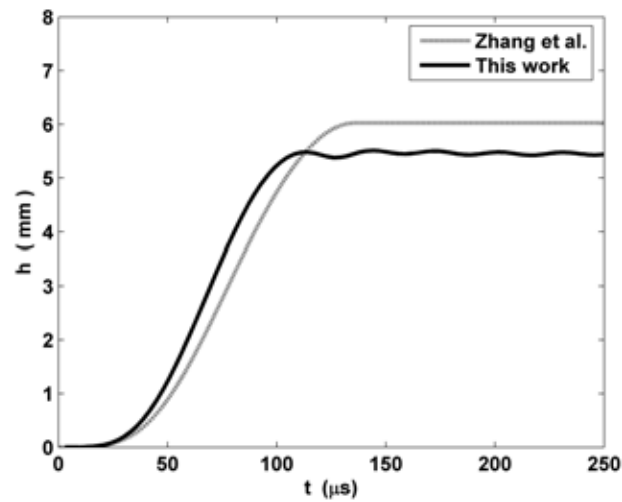


Figure 5.20: Deflection of the workpiece as a function of time. The results of Zhang et al. [117] are compared with the results of this work.

5.7 Optimum frequency and optimum capacitance

The frequency at which the discharge current oscillates is a key parameter in the design of an electromagnetic forming system. In [34, 117, 41] it is shown that, for a fixed energy U_0 and a given set of capacitor bank, connectors, coil and workpiece, there exist a frequency ν_{op} at which the maximum deformation of the workpiece is achieved. The use of this optimum frequency saves energy and prevents the premature wearing of the coil.

The frequency of the discharge ν is controlled by the capacitance C_{cb} for a given set of capacitor bank, connectors, coil and workpiece. The relationship between C_{cb} and ν is described by equations (5.7) and (5.10). Therefore, the search for the optimum frequency ν_{op} is equivalent to the search for the optimum capacitance C_{op} . Usually, in EMF, there is only a discrete set of capacitances C_{cb} available in the capacitor bank. Then, once we have determined C_{op} we must search for the closest available C_{cb} . In this work, we will refer indistinctly to the available value or to the theoretical value as the optimum capacitance C_{op} .

The optimum capacitance can be obtained computing the deformation of the workpiece for the available C_{cb} using the same initial charging energy U_0 in all the numerical simulations. Thereafter, we select the capacitance C_{cb} which produces the maximum deformation. This is the approach followed in [34, 117, 41]. We can reduce the number of electro-mechanical simulations if we make an initial estimation C_{ig} close to the optimum value C_{op} . In fact, if C_{ig} is close enough, we can find C_{op} with only three simulations. For instance, suppose that C_{ig} falls between two available capacitances C_1 and C_2 , being $C_1 < C_2$. We make two electro-mechanical simulations and obtain that the deflections of the workpiece satisfy $h_1 < h_2$. Afterwards, we take a capacitance C_3 which is the lower value available such as $C_2 < C_3$. If we compute that $h_2 > h_3$ then C_2 is the optimum capacitance. In this case, we have required only three electro-mechanical simulations. On the other hand, if $h_2 < h_3$, we must keep on testing with successive C_n until find a n such as $h_n > h_{n+1}$. When this happens, we have that C_n is the optimum capacitance and $n + 1$ the number of electro-mechanical simulations. Therefore, the better C_{ig} is the less $n + 1$ is.

The simplest way to find an initial guess is derived from expression (5.25). As it is mentioned in section 5.5.3, we have observed in the literature that the typical frequencies employed in EMF lay in the interval (5.25). Therefore, we can consider an initial estimation ν_{ig} as the frequency which satisfies $\delta = \tau$.

We can improve the initial guess if we have prior knowledge about the workpiece. For instance, in [34], it is stated that the optimum frequency for the compression of a tube of thickness $\tau = 2$ mm made of aluminium AA3003 satisfies $\delta = 0.66 \tau$. If we are going to use the same workpiece in a different EMF process (different coil or capacitor bank) we can try the frequency which satisfy $\delta = 0.66 \tau$ as the initial guess. The same can be applied to the workpiece used in [117], where it is found that the optimum frequency for the expansion of a tube of thickness $\tau = 1$ mm made of aluminium A1050TD satisfies $\delta = 0.9 \tau$.

In the case we do not possess any prior knowledge about workpiece we propose a method to find ν_{ig} . The idea is to look for the frequency which produces the maximum momentum \mathbf{P} in the first n semi-periods, where a semi-period is half a period $T/2 = 1/2\nu$. That is, we look for the

frequency which makes maximum the quantity

$$\Delta \mathbf{P}_n = \int_0^{\frac{n}{2\nu}} \mathbf{F}_{tot} \cdot dt, \quad (5.30)$$

where \mathbf{F}_{tot} is the total magnetic force acting on the workpiece and $\Delta \mathbf{P}_n$ is the momentum produced by this force in the first n semi-periods. The number n depends on the application and we obtained the best results with the minimum natural number which accomplish

$$n \geq \frac{4L_0\nu_\infty}{R_0}, \quad (5.31)$$

where L_0 and R_0 are the inductance and the resistance defined in section 5.3.3 and ν_∞ is the frequency which makes maximum the quantity $\Delta \mathbf{P}_\infty$. The quantity $\Delta \mathbf{P}_\infty$ is obtained when $n \rightarrow \infty$ in (5.30). L_0 and R_0 are evaluated at the frequency ν_∞ . The expression (5.31) comes from reordering $(n/2\nu) \geq (1/\gamma_0)$, where γ_0 is defined in (5.8), and it represents the minimum number of semi-periods required to release more than 80% of the total momentum $\Delta \mathbf{P}_\infty$.

In summary, we first locate the frequency ν_∞ which makes maximum the quantity $\Delta \mathbf{P}_\infty$. Second, we compute n with (5.31) at ν_∞ . Finally, ν_{ig} is the frequency which makes maximum $\Delta \mathbf{P}_n$, being n the natural number calculated in the second step. All this process is performed neglecting the workpiece deformation. We do not require any additional simulation. We are using the data obtained in the initial frequency sweep of our electromagnetic model. It takes only a few seconds to compute all the integrals and obtain ν_{ig} . In the next section we apply this method to two particular examples.

5.8 Optimum capacitance estimation

In this section we are going to obtain an initial guess C_{ig} for the tube bulging process analyzed in [117] and for the tube compression process analyzed in [34]. We apply the method proposed in section 5.7 to calculate C_{ig} .

5.8.1 Tube bulging

In [117] is analyzed the expansion of a tube by a solenoidal coil under different working conditions. They used several coils with lengths $\ell = \{100, 200, 300, 400, 500\}$ mm. They computed for each coil the bulge height with the capacitance varying from $C_{cb} = 20 \mu\text{F}$ to $C_{cb} = 1600 \mu\text{F}$. They obtained the optimum capacitance C_{op} for each coil length and concluded that the optimum frequency satisfy $\delta = 0.9 \tau$ in all the cases.

We analyzed this problem with the geometry, material properties and FEM model detailed in section 5.6. We found that the number defined in (5.31) is $n = 2$ in all the cases. Then, the initial guess C_{ig} is the capacitance which makes maximum the quantity $\Delta \mathbf{P}_2$ defined in (5.30). In fig. 5.21 we show the momentum $\Delta \mathbf{P}_2$ as a function of the capacitance C_{cb} for the coil lengths $\ell = \{200, 300, 400, 500\}$ mm and the initial charging energy $U_0 = 2$ kJ. In Table 5.1 we show the values of C_{ig} compared with the optimum capacitances C_{op} calculated in [117].

In [117] is also analyzed a coil with $\ell = 100$ mm and $U_0 = 1$ kJ. They measure the bulge height for the capacitances $C_{cb} = \{24, 50, 100, 200, 400, 800, 1600\} \mu\text{F}$ and they found that the maximum height was in $C_{cb} = 200 \mu\text{F}$. They also calculated numerically the optimum capacitance and they obtained a value of $C_{op} = 310 \mu\text{F}$. We calculated the initial guess with the method of section 5.7 and we found that $C_{ig} = 296 \mu\text{F}$.

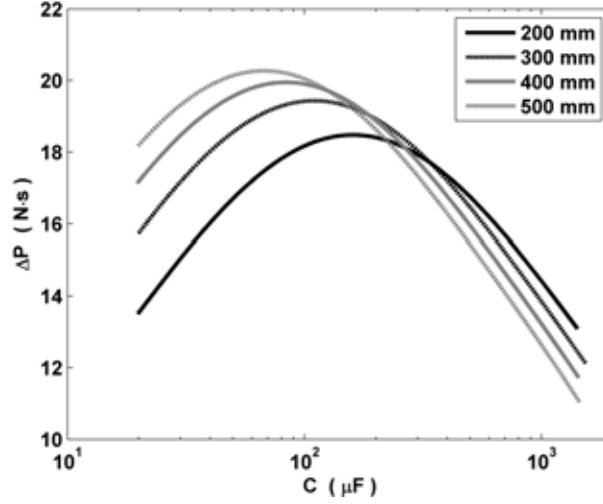


Figure 5.21: Momentum ΔP_2 as a function of the capacitance C_{cb} for several coil lengths. The initial charging energy is $U_0 = 2$ kJ in all the cases. The initial guess C_{ig} is the capacitance which makes maximum the quantity ΔP_2 . The values of C_{ig} are shown in Table 5.1.

ℓ (mm)	C_{op} (μF)	C_{ig} (μF)
200	160	161
300	100	108
400	70	83
500	40	67

Table 5.1: Optimum capacitance (C_{op}) and initial guess (C_{ig}) for different coil lengths (ℓ).

5.8.2 Tube compression

In [34] is analyzed the compression of a tube by a solenoidal coil for the capacitances $C_{cb} = \{60, 120, 240, 360, 480, 600, 702, 720, 840, 960, 1080, 1800\} \mu\text{F}$ and the initial charging energy $U_0 = 2.02$ kJ. They computed the radial displacement of the walls of the tube and they found that the maximum displacement occurs when $C_{op} = 840 \mu\text{F}$, $\nu_{op} = 4.97$ kHz and $\delta = 0.66 \tau$.

We analyzed numerically this problem with the geometry of fig. 5.22. The geometry represents half of the coil and the workpiece placed inside a truncated portion of a semi-sphere with an angle of 20° . The FEM model used here is similar to that described in sections 5.5.2 and 5.6.2.

The workpiece is made of the aluminium alloy AA3003. The electrical conductivity is $\sigma = 29.4e6$ S/m. The outer diameter of the workpiece is $D_{wp} = 50.0$ mm. Its thickness is $\tau = 2$ mm and its length is $\ell = 100.0$ mm.

The solenoidal coil is approximated by coaxial loop currents, concentric with the workpiece and placed outside it. The coil is made of copper with a conductivity of $\sigma = 58e6$ S/m. The inner diameter of the coil is $D_c = 56.0$ mm. The separation between each loop is $p = 6.25$ mm. The length of the coil is $\ell = 100$ mm and the number of turns is $N = 17$. The dimensions of the coil wires are not provided in [34]. We assumed a thickness of $\Delta x_c = 5$ mm and a height of $\Delta y_c = 3$ mm for each coil wire.

In [34] is assumed that $R_0 = R_{cb} + R_{con} + R_{cw} = 13.03$ m Ω and $L_0 = L_{cb} + L_{con} + L_{cw} = 1.22$ μ H for all the frequencies. Therefore, for comparison purposes, we assumed the same.

We found that the maximum of $\Delta \mathbf{P}_\infty$ was in $\nu_\infty = 13$ kHz. If we substitute ν_∞ , L_0 and R_0 in (5.31), we have that $n = 5$. Then, C_{ig} is the capacitance which makes maximum the quantity $\Delta \mathbf{P}_5$. In fig. 5.23 we show the momentum $\Delta \mathbf{P}_5$ as a function of the capacitance C_{cb} . The maximum is at $C_{ig} = 805$ μ F, $\nu_{ig} = 5$ kHz and $\delta = 0.66 \tau$.

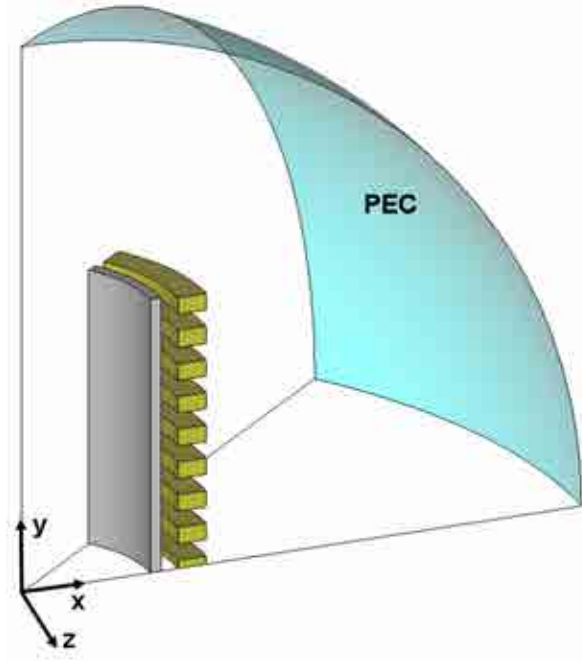


Figure 5.22: Geometry used in ERMES to compute the electromagnetic fields of the tube compression process analyzed in [34].

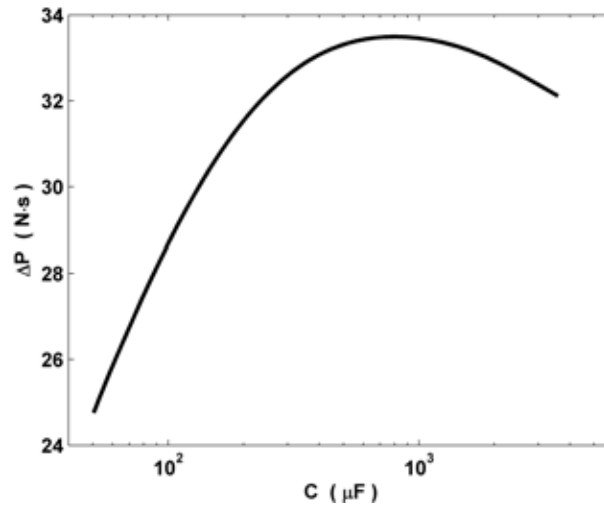


Figure 5.23: Momentum ΔP_5 as a function of the capacitance C_{cb} . The initial guess C_{ig} is the capacitance which makes maximum the quantity ΔP_5 . The value of the initial guess is $C_{ig} = 805 \mu\text{F}$.

5.9 Summary

In this chapter we have presented a numerical model for the simulation of electromagnetic forming processes. This method is computationally efficient because it only requires to solve the time-harmonic Maxwell equations for a few frequencies to have completely characterized the EMF system. The approach can be very useful for estimating the order of magnitude of the parameters of an EMF process, for experimentation on modeling conditions or for modeling complex geometries. Moreover, it can be easily included in a sequential coupling strategy without the worry of numerical instabilities. The method provides an explicit relation between the capacitance of the capacitor bank and the frequency of the discharge. This allow us to estimate the optimum frequency and capacitance at which it is attained the maximum workpiece deformation for a given initial energy and a given set of coil and workpiece. Also, it offers an alternative to the more extended time domain methods and a new insight into the physics of EMF. Finally, we have shown that the numerical results provided by this method exhibit a good correlation with the measurements and with the theoretical developments of other authors.

Chapter 6

Transfer impedance of cable shields

The transfer impedance of a cable shield is a parameter that characterizes its shielding effectiveness. The aim of this chapter is to adapt a general-purpose finite element formulation to the computation of this parameter. The advantage of using a numerical approach, instead of the usual analytical or semi-empirical approaches, is that it reproduces more accurately the high frequency behavior of the transfer impedance and that it can be applied to a wider variety of situations where complex geometries and materials may be present. After the presentation of the numerical model we will apply it to perforated tube shields and we will compare the results of our simulations with analytical models and measurements found in the literature. The work described in this chapter has been introduced in [81, 95, 96] and it is part of the project HIRF-SE (High Intensity Radiated Fields Synthetic Environment), European Community's 7th Framework Programme FP7/2007-2013, ref.: 205294.

6.1 Introduction

The transfer impedance Z_t (also known as surface transfer impedance) characterizes the quality of a cable shield. A lower transfer impedance indicates a good shielding against interfering electromagnetic fields. This concept was initially introduced by Schelkunoff in [94] and it is an intrinsic parameter that represents, independently of environmental factors, the shielding effectiveness of a cable shield. Also, the measurement of Z_t is relatively easy to perform and the experimental setup provides accuracy and repeatability (for a review of measurements methods see for instance [4]).

The knowledge of Z_t is important because it determines the coupling of interference to the wires inside the cable shield. An interference current will be induced in the shield of a cable which is exposed to an electromagnetic field, either because the cable acts as an antenna or because the (grounded) shield is part of a loop in which an interference voltage is induced. In the latter case an interference current will flow depending on the impedance of the loop. If the transfer impedance is known the common mode voltage between the inner conductors and the shield can be determined. Therefore, with the knowledge of Z_t , we can estimate the effect produced by an external field in the wires inside the cable, or reciprocally, we can also estimate the radiation leaked from inside the cable to the environment.

A number of analytical and empirical approaches have been formulated in the past to determine the transfer impedance of cable shields, specially to the most usual arrangement based on braided metal wires [112, 55, 108, 93, 51, 33]. The low and medium frequency behavior of the transfer impedance (DC resistance and skin depth) can be determined quite accurately with these models. However, the behavior of the inductance of the metal braid is very complex. The accuracy of the analytical and empirical models for the higher frequencies in which the inductance plays an important role is sometimes poor. A numerical approach might provide a higher accuracy especially for the high frequency behavior. Also, it can be applied systematically to a wider variety of situations where complex geometries and materials may be present.

The objective of this work is to develop a numerical model for the computation of the transfer impedance of cable shields. This numerical model is based on the finite element method (FEM). More specifically, it is based on the finite element formulation explained in chapter 3. Nevertheless, our numerical model can be easily adapted to any other FEM formulation. You only need to calculate the electric field with your preferred formulation or a "black-box" commercial software and then perform the surface integrals of section 6.2.

In section 6.2 we introduce the formal definition of transfer impedance Z_t . Then, we re-express Z_t as a function of the electric field integrated on the exterior and transversal surfaces of the shield.

In section 6.3 we adapt the general-purpose finite element formulation of chapter 3 to the specific problem of computing Z_t . The input data required in this process are the geometry and the material properties of the shield. The output data is the electric field.

In section 6.4 we validate the numerical model by computing the transfer impedance of perforated tubes and comparing the results of our simulations with analytical methods and measurements found in the literature. The reason for selecting perforated tubes shields instead of the more usual braided wires shields is because the braided wires present some uncertainties which can hinder the validation process. This uncertainties are due mainly to the contact impedance between adjacent and porpoising wires or changes in the properties because of aging and handling [10]. The objective of the present work is to show that our finite element model can give accurate results. It is left for a future work the application of the same numerical model to the study of braided wires shields.

6.2 Definitions

The transfer impedance Z_t (Ω/m) of a cable shield is defined as [94, 112]

$$Z_t = \frac{1}{I_0} \frac{\partial V}{\partial z} \quad (6.1)$$

where I_0 is the current flowing through the shield induced on its outer surface and $\partial V/\partial z$ is the voltage per unit length on the inside of the shield. Definition (6.1) can be re-expressed as a function of the electric field by means of the relations

$$\frac{\partial V}{\partial z} = \frac{1}{A_e} \iint_{S_e} E_z dS_e \quad (6.2)$$

and

$$I_0 = \iint_{S_i} \sigma E dS_i, \quad (6.3)$$

where E is the modulus of the electric field, E_z is the modulus of the longitudinal component of the electric field, S_e is the inner surface of the cable shield, S_i is its transversal surface, A_e is the area of S_e and σ is the electrical conductivity of the shield. Equation (6.2) represents the transversal electric field averaged over the inner surface of the shield and equation (6.3) represents the induced current going through it.

The transfer impedance can also be defined, by reciprocity, as the ratio between the voltage per unit length on the outer surface of the shield and the current flowing through the shield induced on its inner surface [10]. In this last case, S_e is the outer surface of the cable shield and (6.2) represents the transversal electric field averaged over its outer surface (see fig. 6.1 and fig. 6.2).

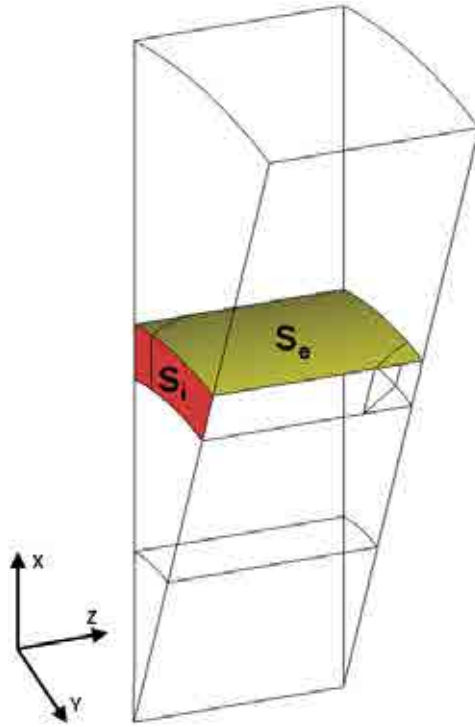


Figure 6.1: Minimum portion of the shield shown in fig. 6.2 necessary to compute its transfer impedance. If we know the value of the electric field \mathbf{E} in the surfaces S_e and S_i we can compute Z_t . We must integrate E_z over S_e to obtain the longitudinal electric field averaged over the outer surface of the shield and $J = \sigma E$ over S_i to obtain a sixteenth of the total induced electric current going through the shield. We have only a sixteenth of the total electric current because S_i is a sixteenth of the whole transversal section of the geometry in fig. 6.2. Therefore, to calculate the total current, we must multiply by sixteen the value of the integral (6.3). On the other hand, the integral (6.2) does not need such a multiplication. Performing the integral (6.2) over the surface S_e give us the same result as if we performed the integral over the whole outer surface of the shield.

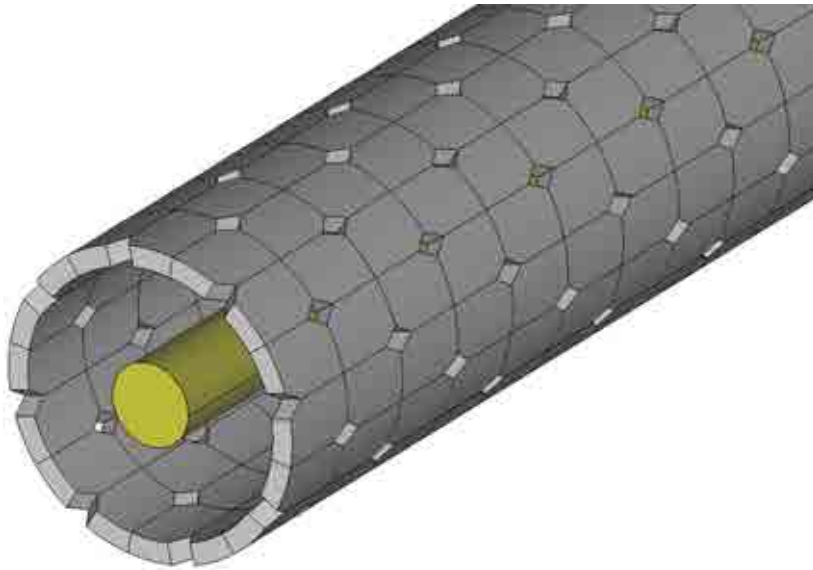


Figure 6.2: Geometry of the shield of a standard RG 58 coaxial cable tinned (section 6.4.3). This cable shield was modeled as a perforated tube with rhomboidal holes. The thickness of the shield is $T = 2d$, being d the diameter of the wires of the braid ($d = 0.12$ mm). The external diameter of shield is $D_{ext} = 3.5$ mm. The braid angle is $\theta = 32.32^\circ$. The numbers of carriers is $C = 16$ and the number of wires in each carrier is $N = 7$. The electrical conductivity is $\sigma = 32.4e6$ S/m, which is the average between the conductivity of copper given in [107] ($\sigma = 56e6$ S/m) and the conductivity of tin ($\sigma = 8.8e6$ S/m [106]).

6.3 Finite element model

From the expressions (6.2) and (6.3), it is clear that, to obtain Z_t , we need first to compute the transversal component of the electric field. In this section, we show how to calculate the electric field in the cable shield with the help of the finite element formulation explained in chapter 3.

The first step is to take a portion of an infinitely long cable shield (see fig. 6.3 and fig. 6.4 or fig. 6.5 and fig. 6.6). Thanks to the special characteristics of our problem we only need to compute the electric field in a portion of the shield. The only requirement to select this portion is that it must have the capacity to generate the whole shield geometry after applying consecutively a mirror symmetry at its faces.

The second step is to induce an electric current in the shield. This can be done by means of an electric field coming from the outside of the shield. In this case, we will integrate the transversal component of the electric field on the internal surface of the shield to obtain Z_t . Another possibility is, by reciprocity, to induce the electric current by means of a field coming from the inside of the shield and integrate the electric field on its exterior surface. These two ways of solving the problem are completely equivalent [10]. We have selected the second option. We produce the incoming inner field by a longitudinal current density J_z placed along the centered inner cylinder shown in fig. 6.4 and fig. 6.6.

As a boundary conditions (see fig. 6.4 or fig. 6.6), we impose on the top surface a first order absorbing boundary condition (1st ABC) adapted to the regularized formulation [36]

$$\begin{aligned}\hat{\mathbf{n}} \times \nabla \times \mathbf{E} &= i\omega\sqrt{\epsilon_0\mu_0} (\hat{\mathbf{n}} \times \hat{\mathbf{n}} \times \mathbf{E}), \\ \nabla \cdot \mathbf{E} &= i\omega\sqrt{\epsilon_0\mu_0} (\hat{\mathbf{n}} \cdot \mathbf{E}),\end{aligned}\quad (6.4)$$

where ϵ_0 and μ_0 are, respectively, the electric permittivity and the magnetic permeability of vacuum. On the longitudinal surfaces we impose the regularized perfect magnetic conductor (PMC) condition [36]

$$\begin{aligned}\hat{\mathbf{n}} \times \nabla \times \mathbf{E} &= 0, \\ \hat{\mathbf{n}} \cdot \mathbf{E} &= 0.\end{aligned}\quad (6.5)$$

Finally, on the transversal surfaces we impose the regularized perfect electric conductor (PEC) condition [36]

$$\begin{aligned}\nabla \cdot (\varepsilon\mathbf{E}) &= 0, \\ \hat{\mathbf{n}} \times \mathbf{E} &= 0.\end{aligned}\quad (6.6)$$

The application of these boundary conditions is possible thanks to the peculiar symmetry of the electric field in the perforated tube geometries. The PEC condition indicates that the field is normal to the transversal surfaces. The PMC condition represents that the field is parallel to the longitudinal surfaces.

On the other hand, expressions (6.5) and (6.6) are not longer applicable when modeling braided wires geometries. In that case we must use periodic boundary conditions. Also, the minimum portion of geometry necessary to compute the transfer impedance is different. This portion must have the capacity to generate the whole braided wire geometry after applying successive translation symmetries in the transversal surfaces and successive rotation symmetries in the longitudinal faces of the problem domain. This model will be the topic of future work.

Summarizing, in the case of perforated tube shields, we are solving the problem of finding $\mathbf{E} \in \mathbf{H}_0(\mathbf{curl}, \text{div}; \Omega)$ such that, $\forall \mathbf{F} \in \mathbf{H}_0(\mathbf{curl}, \text{div}; \Omega)$ holds

$$\begin{aligned}\int_{\Omega} \frac{1}{\mu} (\nabla \times \mathbf{E}) \cdot (\nabla \times \bar{\mathbf{F}}) + \int_{\Omega} \frac{1}{\mu\varepsilon\bar{\varepsilon}} (\nabla \cdot (\varepsilon\mathbf{E})) \cdot (\nabla \cdot (\bar{\varepsilon}\bar{\mathbf{F}})) - \omega^2 \int_{\Omega} \varepsilon (\mathbf{E} \cdot \bar{\mathbf{F}}) \\ - i\omega\sqrt{\frac{\epsilon_0}{\mu_0}} \int_{\partial\Omega_r} (\mathbf{E} \cdot \bar{\mathbf{F}}) = i\omega \int_{\Omega} \mathbf{J} \cdot \bar{\mathbf{F}},\end{aligned}\quad (6.7)$$

where Ω is the problem domain, $\partial\Omega_r$ is the surface where the 1st ABC condition has been applied, \mathbf{E} is the electric field, ω is the angular frequency, \mathbf{J} is the current density, μ is the magnetic permeability and ε is the electric permittivity ($\varepsilon = \epsilon + i\sigma/\omega$). The bar over the magnitudes denotes the complex conjugate. The functional space $\mathbf{H}_0(\mathbf{curl}, \text{div}; \Omega)$ is defined by

$$\mathbf{H}_0(\mathbf{curl}, \text{div}; \Omega) := \{\mathbf{F} \in \mathbf{H}(\mathbf{curl}, \text{div}; \Omega) \mid \hat{\mathbf{n}} \times \mathbf{F} = 0 \text{ in PEC, } \hat{\mathbf{n}} \cdot \mathbf{F} = 0 \text{ in PMC}\}. \quad (6.8)$$

In the presence of a field singularity or a surface of discontinuity between two media, we apply the techniques explained in chapter 3.

Once \mathbf{E} is known, we must return to the equations (6.2) and (6.3) to obtain Z_t . The integration surfaces S_e and S_i are shown in fig. 6.1. S_e is the surface just above the shield and also includes

the holes. S_i can be the forward or the backward surface in fig. 6.1. A third option to calculate (6.3) consists in doing the integration over the forward and over the backward transversal surfaces and then perform the geometric average between these two values. We must recall that the surface S_i shown in fig. 6.1 is only a fraction of the whole transversal section of the shield. Therefore, to calculate the total intensity flowing through the shield, which is the magnitude required in (6.1), we must multiply (6.3) by the number of times required to recover the whole transversal section. For instance, in the case shown in fig. 6.1, which represents a sixteenth of the whole geometry of fig. 6.2, we have to multiply (6.3) by sixteen. On the other hand, the integral (6.2) does not need such a multiplication. Performing the integral (6.2) over the surface S_e of fig. 6.1 give us the same result as if we performed the integral over the whole outer surface of the shield.

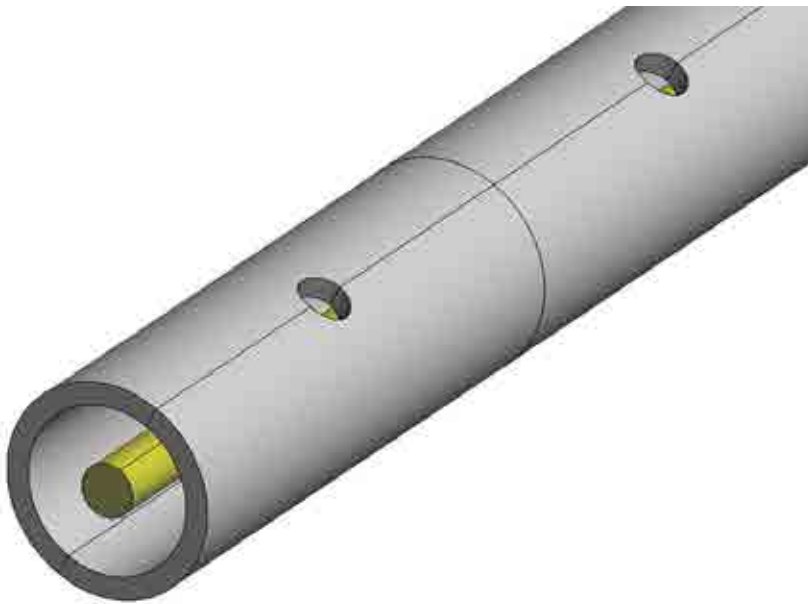


Figure 6.3: Perforated tube with 22 circular holes per meter. Each hole has a diameter $d_h = 3.175$ mm. The thickness of the wall is $T = 1.683$ mm. The external diameter of the tube is $D_{ext} = 15.875$ mm. The tube is made of brass with an electrical conductivity of $\sigma = 13.32e6$ S/m.

6.4 Validation

In this section we apply our numerical model to different cable shield configurations: a homogeneous tube, four different perforated tubes with circular holes and to a standard RG 58 coaxial cable tinned. As mentioned in the introduction of this chapter, we have selected these configurations because they present less uncertainties than the usual configurations based on braided wires. It is left for a future work the application of the present numerical model to the study of the transfer impedance of braided wires shields.

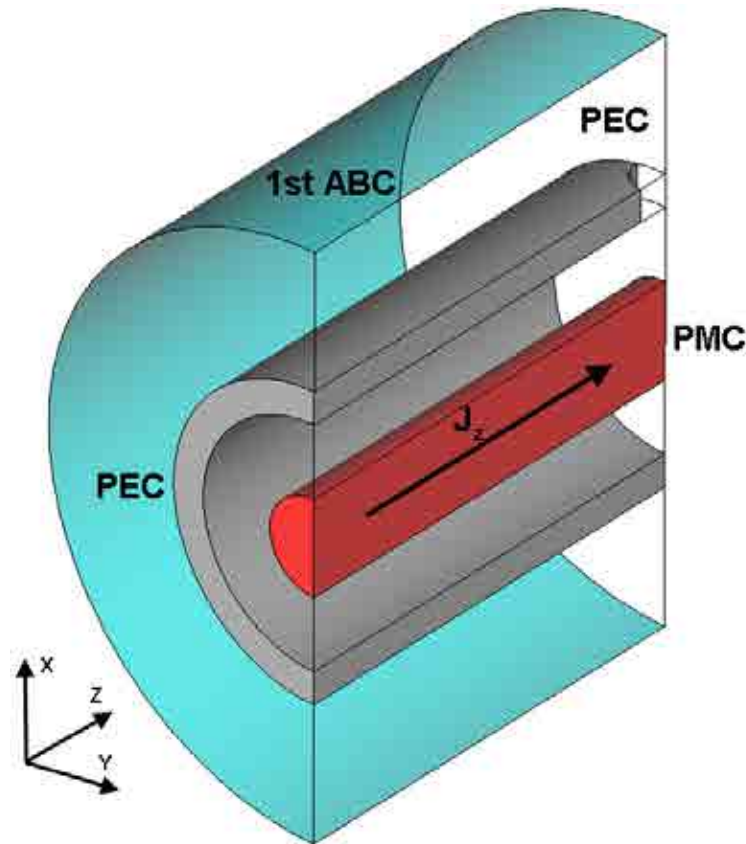


Figure 6.4: Detail of the geometry of the shield shown in fig. 6.3. This geometrical set-up was used to compute the electric field with ERMES. In the two transversal surfaces is applied a perfect electric conductor boundary condition (PEC). In the longitudinal surface is applied a perfect magnetic boundary condition (PMC). In the exterior curved surface is applied a first order absorbing boundary condition (1st ABC). The problem is driven by a volumetric current density J_z located along the central axis of the shield.

We employed the in-house code ERMES to find the numerical solution of the problems shown here. ERMES is the C++ implementation of the formulation explained in chapter 3 and its main features are displayed in appendix A. We used isoparametric tetrahedral second order nodal elements with 3UL (see chapter 3) and the resulting linear system was solved using a quasi-minimal residual (QMR) iterative solver [28] with a diagonal preconditioner. In all the simulations performed the convergence of the solver was excellent, proving the well-conditioning of the matrix. In average, it were used around 200000 tetrahedral second order nodal elements which produced a linear system with about 600000 unknowns. Around 700 iterations of the solver were necessary to reach a residual ($\|Ax - b\| / \|b\|$) of less than $1e-4$. The memory employed was approximately 1 GB and the time spent solving each frequency was around 400 seconds. These data are referred to a desktop computer with a CPU Intel Core 2 Quad Q9300 at 2.5 GHz and the operative system Microsoft Windows XP.

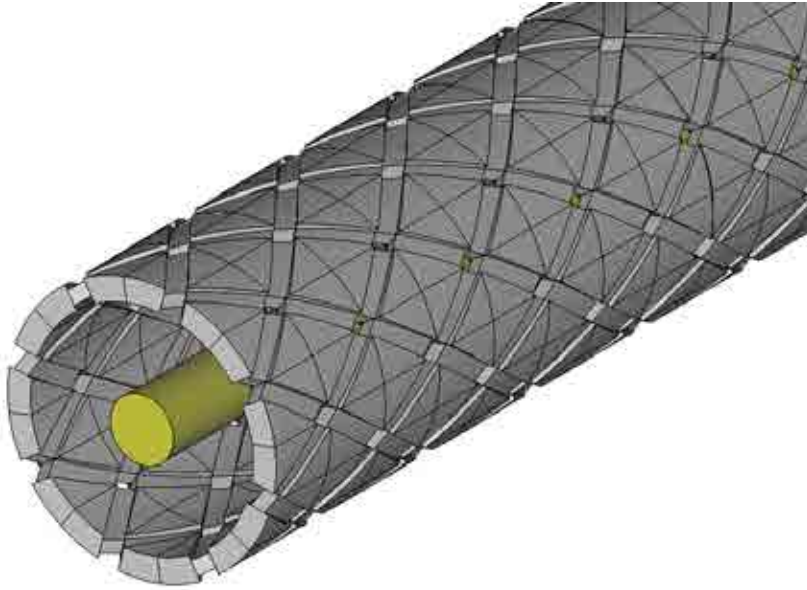


Figure 6.5: Geometry of the shield of a standard RG 58 coaxial cable tinned (section 6.4.3). This cable shield was modeled as a perforated tube with rhomboidal holes. In the areas where the carriers of the braid overlap each other the thickness of the shield is $T = 2.5d$ [18], being d the diameter of the wires of the braid ($d = 0.12$ mm). In the areas where the carriers of the braid do not overlap each other the thickness of the shield is $T = 1.5d$. The external diameter of shield is $D_{ext} = 3.5$ mm. The braid angle is $\theta = 32.32^\circ$. The numbers of carriers is $C = 16$ and the number of wires in each carrier is $N = 7$. The electrical conductivity is $\sigma = 32.4e6$ S/m, which is the average between the conductivity of copper given in [107] ($\sigma = 56e6$ S/m) and the conductivity of tin ($\sigma = 8.8e6$ S/m [106]).

6.4.1 Homogeneous tube

In fig. 6.7 is shown the transfer impedance calculated with ERMES for a stainless steel tube with an internal radius $r_{int} = 3.625$ mm, wall thickness $T = 0.91$ mm and electrical conductivity $\sigma = 1.1e6$ S/m. In a homogeneous tube, only the current diffusion is important and the values of Z_t are due to DC resistance modified by skin-effect screening. In this case, an analytical solution can be obtained from the formula given in [111]

$$Z_t = \frac{\gamma}{\sigma 2\pi a} \left(\frac{1}{\sinh(\gamma T)} \right), \quad (6.9)$$

where γ is the propagation constant in the shield material, σ is the conductivity of the shield, T is its thickness and a is its mean radius ($a = r_{int} + T/2$). The analytical results were computed using $a = 4.08$ mm, $T = 0.91$ mm and $\sigma = 1.1e6$ S/m.

The measurements shown in fig. 6.7 were performed in [89]. The shield configuration consisted in the core (inner conductor plus dielectric) of a URM 67 cable with a solid stainless steel outer conductor 0.91 mm thick. In [89] is assumed an electrical conductivity of $0.8e6$ S/m for stainless steel at room temperature. This figure is too low compared to the values found in the literature (see for instance [106] or [23]). We adopted the more reasonable value of $\sigma = 1.1e6$ S/m

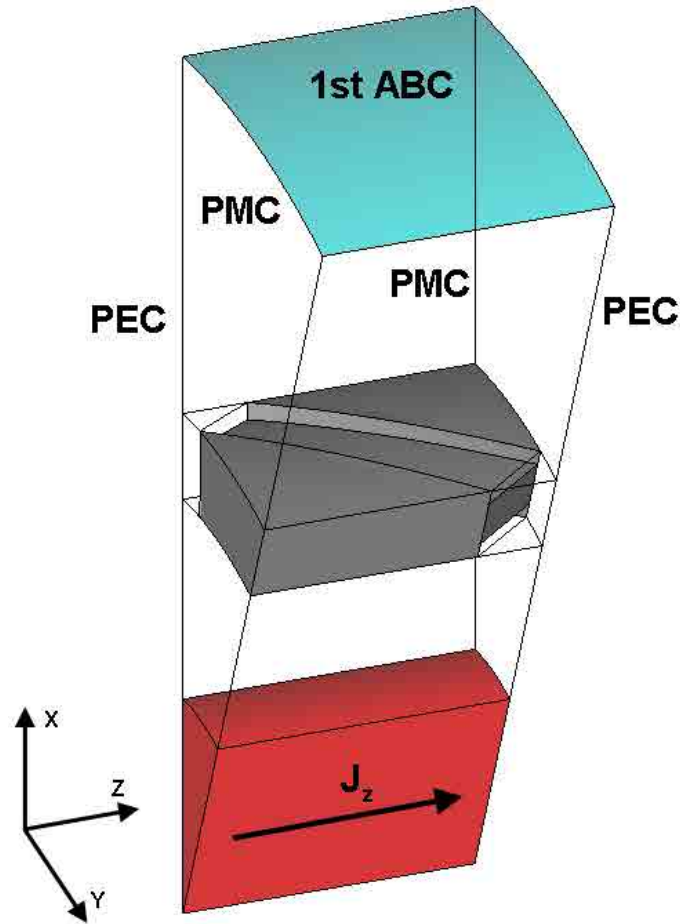


Figure 6.6: Detail of the geometry of the shield shown in fig. 6.5. This geometrical set-up was used to compute the electric field with ERMES. In the two transversal surfaces is applied a perfect electric conductor boundary condition (PEC). In the two longitudinal surfaces is applied a perfect magnetic boundary condition (PMC). In the upper curved surface is applied a first order absorbing boundary condition (1st ABC). The problem is driven by a volumetric current density J_z located along the central axis of the shield.

for the simulations and the analytical calculations. If we use $\sigma = 0.8e6$ S/m we obtain the same Z_t with ERMES and with the equation (6.9) but, these results are displaced upwards with respect the measurements in [89]. The numerical results of fig. 6.7 were obtained considering vacuum in the core of the tube. Nonetheless, simulations performed with ERMES adding a dialectic (polyethylene, $\epsilon_r = 2.3$) produced the same values of Z_t that the ones shown in fig. 6.7.

6.4.2 Perforated tubes with circular holes

Four different configurations of perforated tubes were simulated with ERMES. The first one, shown in fig. 6.3, has 22 circular holes per meter, each hole with a diameter $d_h = 3.175$ mm. The

external diameter of the tube is $D_{ext} = 15.875$ mm and the thickness of the wall is $T = 1.683$ mm. The tube is made of brass with an electrical conductivity of $\sigma = 13.32e6$ S/m. The results of the simulations with ERMES compared with measurements and analytical formulas are shown in fig. 6.8. The rest of the configurations consisted in three different copper tubes with one circular hole per meter. The diameter of the hole in each tube was, respectively, $d_h = 15.875$ mm, $d_h = 9.525$ mm and $d_h = 6.350$ mm. All three tubes had the same external diameter $D_{ext} = 31.750$ mm and the same wall thickness $T = 1.504$ mm. It was considered an electrical conductivity for copper of $\sigma = 58e6$ S/m. In fig. 6.9 are compared the results of the simulations with measurements. In fig. 6.10 the simulations and the measurements are compared with two different analytical approaches. The analytical results of Vance [111] were obtained with the formula

$$Z_t = \frac{\gamma}{\sigma 2\pi a (1 - \tau) \sinh(\gamma T)} + i\omega v \frac{\mu_0 m}{4\pi^2 a^2}, \quad (6.10)$$

where v is the number of holes per unit length, m is the polarizability of each hole, τ is the transparency of the shield and the remainder symbols are the same as in (6.9). The first term of (6.10) is equal to the transfer impedance of a solid shield (6.9) except for the scalar factor $(1 - \tau)$, which represents the shield coverage. For a perforated shield containing v uniformly distributed circular holes, each with a radius r_h , we have

$$\tau = v \frac{r_h^2}{2a}. \quad (6.11)$$

The second term in (6.10) is a mutual inductance that depends on the number of openings v in the shield and the polarizability m of each opening. For a circle of radius r_h , the polarizability is

$$m = \frac{4r_h^3}{3}. \quad (6.12)$$

The bad results given by (6.10) (see fig. 6.8 and fig. 6.10) are mainly due to the implicit assumption made in (6.12) that the thickness of the shield T is small compared to the radius r_h of the circular apertures. On the other hand, in the model proposed by Kley [51] the effect of a non-negligible thickness is considered. The expression provided in [51] for the transfer impedance of a solid shield perforated with circular holes reads as follows:

$$Z_t = Z_R + i\omega v M_{LL} + (1 + i)\omega v L_{SL}, \quad (6.13)$$

where Z_R is the transfer impedance of a solid shield, M_{LL} is the hole inductance and L_{SL} is the skin inductance. Z_R is equal to the first term of (6.10)

$$Z_R = \frac{\gamma}{\sigma 2\pi a (1 - \tau) \sinh(\gamma T)}. \quad (6.14)$$

M_{LL} is obtained by multiplying the inductance of a hole with negligible thickness by an attenuation factor due to the "chimney effect". The approximate formula for M_{LL} is

$$M_{LL} \approx \mu_0 \frac{0.875 r_h^3}{3\pi^2 a^2} \exp\left(\frac{-1.84 T}{r_h}\right). \quad (6.15)$$

L_{SL} models the effect of the eddy currents induced in the walls of the hole. The approximate formula for L_{SL} is

$$L_{SL} \approx \frac{Tr_h}{2a^2} \exp\left(\frac{-2.30T}{r_h}\right) \sqrt{\frac{\mu}{2\sigma\omega}}. \quad (6.16)$$

In fig. 6.8 and fig. 6.10 is clear the improvement introduced by Kley (6.16) with respect to Vance (6.10).

The measurements in fig. 6.8, fig. 6.9 and fig. 6.10 were carried out in [40]. The data provided in [40] for the tube with $v = 22$ holes/meter (fig. 6.8) were $D_{ext} = 15.875$ mm (5/8 in), $d_h = 3.175$ mm (1/8 in) and the material of the tube (brass, an alloy with an electrical conductivity which can vary between $10e6$ S/m and $30e6$ S/m). The thickness T and the conductivity σ were not provided in [40] but we deduced them from fig. 6 in [40]. In the graph of fig. 6 [40] is displayed the measured transfer impedance of the same tube, but without holes. Then, we can infer T and σ with the help of equation (6.9). From fig. 6 [40] we know that $|Z_t|_{1\text{KHz}} = 1$ m Ω /m and $|Z_t|_{100\text{KHz}} = 0.23$ m Ω /m. If we solve (6.9) with these values of $|Z_t|$ we obtain $T = 1.683$ mm and $\sigma = 13.32e6$ S/m.

A similar situation is found for the three tubes with $v = 1$ holes/meter (fig. 6.9 and fig. 6.10). The data provided in [40] are $D_{ext} = 15.875$ mm (1-1/4 in), $d_h = 15.875$ mm (5/8 in), $d_h = 9.525$ mm (3/8 in), $d_h = 6.350$ mm (1/4 in) and the material of the tubes (copper). We assumed a conductivity for copper of $\sigma = 58e6$ S/m [106] and we deduced the thickness from fig. 2 in [40]. In the graph of fig. 2 [40] is shown the measured transfer impedance for the same tubes but without holes. From fig. 2 [40] we know that $|Z_t|_{1\text{KHz}} = 0.12$ m Ω /m. If we solve (6.9) with this value of $|Z_t|$ we obtain a thickness $T = 1.504$ mm.

6.4.3 Standard RG 58 coaxial cable tinned

The last validation example is the braided wire shield of a standard RG 58 coaxial cable in which the wires were fused together with a tin solder dip [107]. The braided shield consists of $C = 16$ interwoven carriers, each carrier having $N = 7$ copper wires with a diameter $d = 0.12$ mm. The diameter of the shield is $D = 3.5$ mm. The angle between the cable direction and the wires, the braid angle θ , is not provided in [107]. We derived θ by considering that, in general, the optical coverage of a RG 58 is $K = 0.95$ (95%) and its filling factor is less than 1 ($F < 1$). The definition of the filling factor F is [112]

$$F = \frac{CNd}{4\pi a \cos(\theta)}, \quad (6.17)$$

where C is the number of carriers, N is the number of wires per carrier, d is the diameter of each wire, θ is the braid angle and a is the mean radius of the shield ($a = r_{int} + d$, where r_{int} is the inner radius of the shield). The filling factor F is related with the optical coverage K by means of the equation

$$K = 2F - F^2. \quad (6.18)$$

Imposing $K = 0.95$ and $F < 1$ in (6.18) gives $F = 0.7764$. If it is replaced this value of F in (6.17) with $C = 16$, $N = 7$, $d = 0.12$ mm and $a = 1.63$ mm, it is finally obtained the braid angle $\theta = 32.32^\circ$.

The analytical results by Vance [112] shown in fig. 6.11 and 6.12 were obtained representing the diamond-shaped holes of fig. 6.2 as elliptical holes. The expression of Z_t in this case is similar to (6.10) but with

$$\tau = v \frac{w_e l_e}{8a} \quad (6.19)$$

and

$$m = \frac{\pi l_e^3}{24} \left(\frac{(1 - e^2) e^2}{E(e) - (1 - e^2) K(e)} \right), \quad (6.20)$$

where l_e is the major axis of the equivalent elliptical hole, w_e is the minor axis, e is the eccentricity ($e = \sqrt{1 - (w_e/l_e)^2}$) and $K(e)$ and $E(e)$ are the complete elliptic integrals of the first and the second kind, respectively, defined by

$$\begin{aligned} K(e) &= \int_0^{\pi/2} \frac{1}{\sqrt{1 - e^2 \sin^2(\varphi)}} d\varphi, \\ E(e) &= \int_0^{\pi/2} \sqrt{1 - e^2 \sin^2(\varphi)} d\varphi. \end{aligned} \quad (6.21)$$

Equation (6.20) is valid when $\theta < 45^\circ$. The parameters l_e , w_e and v can be deduced from the known values F , θ , N and d thanks to the relations [112]

$$v = 4\pi a \sin(\theta) \cos(\theta) \left(\frac{F}{Nd} \right)^2, \quad (6.22)$$

$$l_e = \frac{(1 - F) Nd}{F \sin(\theta)}, \quad (6.23)$$

$$w_e = \frac{(1 - F) Nd}{F \cos(\theta)}. \quad (6.24)$$

The bad results given by the Vance model in fig. 6.11 and fig. 6.12 can be attributed to same reason as in the previous examples with circular holes, the non-depreciable thickness of the shield to respect the size of the holes. Unfortunately, we had not found available in the literature any adaptation of the Kley's model (6.16) to perforated solid tubes with diamond-shaped holes. Hence, in fig. 6.11 and fig. 6.12, we employed (6.16) with $r_h = \sqrt{l_e w_e / 4}$, that is, we approximate the rhomboidal holes as circular and with the same area as the equivalent elliptical hole. In this case, the bad results given by Kley's model can be attributed to a lack of a properly adaptation to the new circumstances.

We simulated with ERMES the tinned RG 58 cable with two different geometrical models. The first one is shown in fig. 6.2 and the results appear in fig. 6.11. We can see an excellent resemblance with measured data in the high and low frequency range. The second geometrical model is shown in fig. 6.5 and the results appear in fig. 6.12. This last model is more realistic and it presents a better correlation with the measured data in all the frequency range. We must recall that the determination of the electrical conductivity is an approximation ($\sigma = 32.4e6$ S/m, which is the average between the conductivity of copper and the conductivity of tin) and this makes also approximate the value of Z_t in the low and medium frequency range. On the other hand, at higher frequencies Z_t is almost independent of σ .

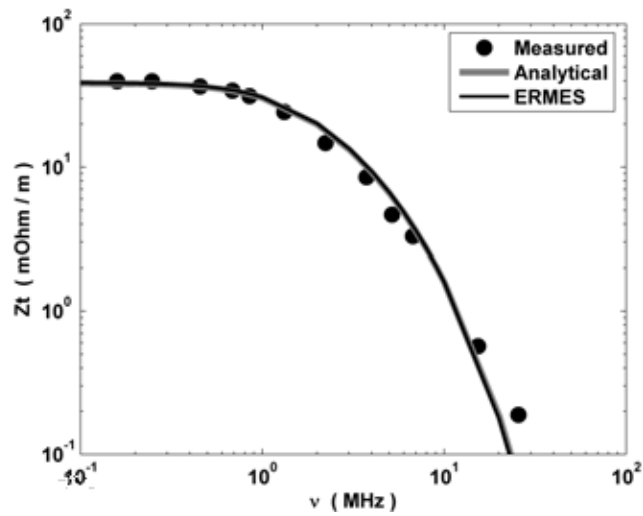


Figure 6.7: Transfer impedance of a stainless steel tube with an internal radius $r_{int} = 3.625$ mm, wall thickness $T = 0.91$ mm and electrical conductivity $\sigma = 1.1e6$ S/m. Analytical results from [111]. Measurements from [89].

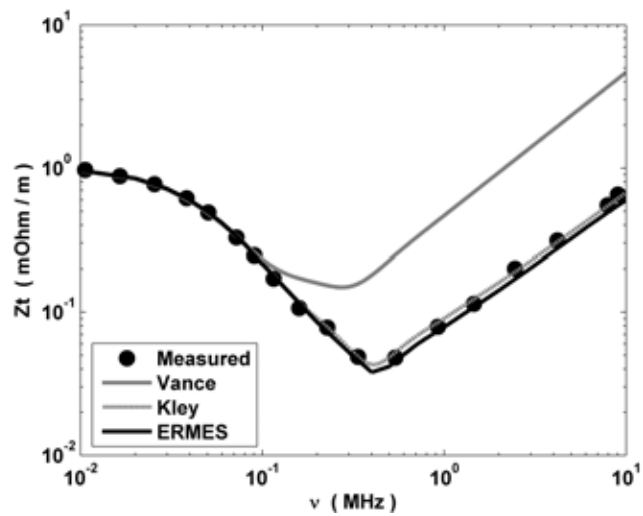


Figure 6.8: Transfer impedance of the perforated tube shown in fig. 6.3 ($\nu = 22$ holes/meter, $d_h = 3.175$ mm, $D_{ext} = 15.875$ mm, $T = 1.683$ mm and $\sigma = 13.32e6$ S/m). Analytical results from Vance [111] and Kley [51]. Measurements from [40].

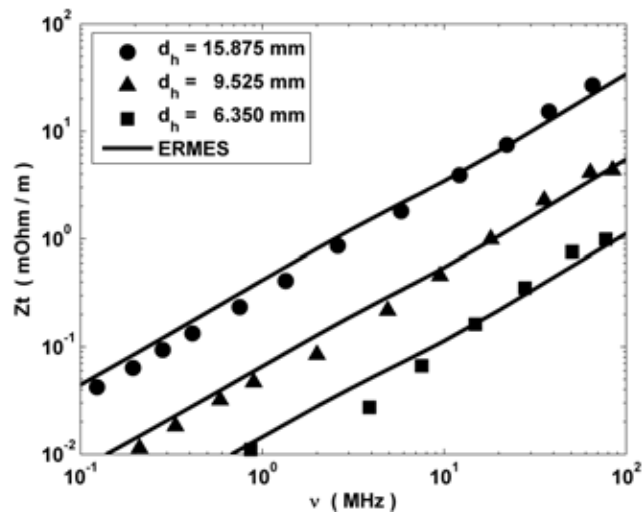


Figure 6.9: Transfer impedance of three copper tubes with 1 circular hole per meter. The diameter of the hole in each tube is, respectively, $d_h = 15.875$ mm, $d_h = 9.525$ mm and $d_h = 6.350$ mm. All three tubes have the same external diameter $D_{ext} = 31.750$ mm and the same wall thickness $T = 1.504$ mm. It is considered an electrical conductivity for copper of $\sigma = 58e6$ S/m [106]. Measurements (\bullet , \blacktriangle , \blacksquare) from [40].

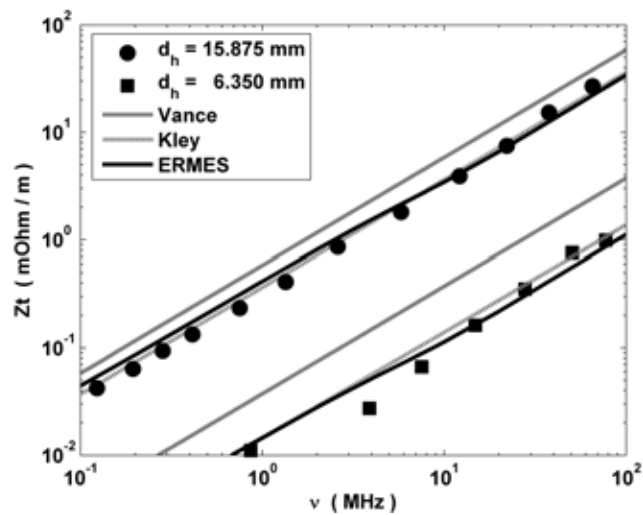


Figure 6.10: Transfer impedance of two of the three copper tubes shown in fig. 6.9. The two tubes selected are those with the maximum and the minimum hole diameter ($d_h = 15.875$ mm and $d_h = 6.350$ mm). Analytical results from Vance [111] and Kley [51]. Measurements (\bullet , \blacksquare) from [40].

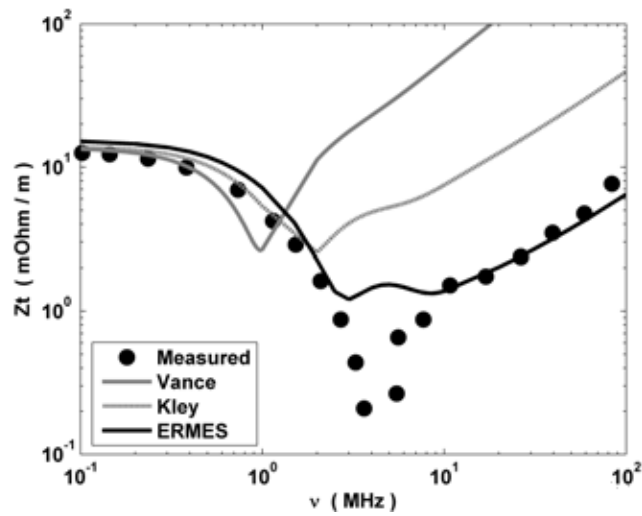


Figure 6.11: Transfer impedance of the shield of a standard RG 58 coaxial cable tinned. This cable shield was modeled as the perforated tube shown in fig. 6.2 ($D_{ext} = 3.5$ mm, $d = 0.12$ mm, $T = 2d$, $\theta = 32.32^\circ$, $C = 16$, $N = 7$ and $\sigma = 32.4e6$ S/m). Analytical results from Vance [112] and Kley [51]. Measurements from [107].

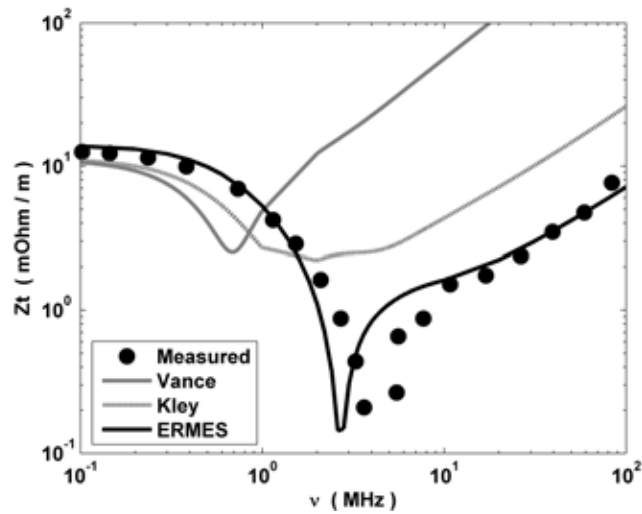


Figure 6.12: Transfer impedance of the shield of a standard RG 58 coaxial cable tinned. For the analytical computations with the formulas of Vance [112] and Kley [51] the shield was modeled as the perforated tube shown in fig. 6.2, but with the values: $D_{ext} = 3.5$ mm, $d = 0.12$ mm, $T = 2.5d$ [18], $\theta = 32.32^\circ$, $C = 16$, $N = 7$ and $\sigma = 32.4e6$ S/m. For the simulations with ERMES the shield was modeled as it is shown in fig. 6.5. Measurements from [107].

6.5 Summary

In this chapter we have presented a numerical model for the computation of the transfer impedance of cable shields. This model has been validated on some specific geometries comparing simulations with measurements. One of the advantages of the numerical approach is its flexibility and its ability to deal with complex geometries and materials. Also, we had shown that our numerical model reproduces more accurately the high frequency behavior of the transfer impedance than the analytical approaches found in the literature.

In a future work the same numerical model presented here will be applied to a more real geometries where interwoven wires will be considered. The numerical model developed for perforated tubes only needs minor changes to be adapted to this new situation. We only have to change the PEC and PMC boundary conditions by periodic boundary conditions and use a different minimum portion of the shield.

The major difficulty in solving braided wires rests in the generation of a computer aided design (CAD) geometry ready to be used as input data for the finite element method. The generation of a braided wire CAD geometry is a time consuming task (more than the computing time of the transfer impedance itself), this is why we are currently developing a computer tool able to generate automatically this kind of geometry after being informed of the relevant parameters. This task is very important if we want to apply the numerical model to the wide variety of different braided wires shields available in the market or if we want to design new ones.

Chapter 7

Conclusions and future work

This chapter summarizes the main conclusions of this work and the futures lines of research and development.

7.1 Regularized Maxwell equations and nodal finite elements

It has been demonstrated that accurate solutions can be obtained with nodal finite elements and the regularized Maxwell equations provided we take care of the singularities and discontinuities of the fields. To take care of the field singularities, we must eliminate the divergence term of the regularized weak form in the elements near the singularity (RME-UL). The number of layers of elements whose divergence term must be eliminated (UL) depends on their order. We reached to the conclusion that the optimal combination is second-order elements with 3 ULs. To take care of the field discontinuities, we must define multiple nodes in the surfaces of discontinuity between different media (one on each surface) and relate them explicitly.

We implemented the above formulation in a C++ code called ERMES. This code was used for computing the scattering parameters of microwave filters and the SAR induced in a body when exposed to electromagnetic fields. The results obtained were accurate but, if there are too many field singularities in the problem domain, the computational cost is high. This is due to the need of meshing with small elements near the singularity and the worsening of the condition number in the resultant matrix. Therefore, it is necessary to further study the treatment of the field singularities in the RME-UL approach to improve its efficiency. We need a deeper understanding of the relation between the number of ULs and the element size, element order and singularity order. Also, we need to study in more detail how the ULs affect the well-conditioning of the RME-UL matrix.

It is left for future work the improvement of ERMES capabilities. This includes the improvements in the modelization of the electric field singularities, the implementation of better solvers and preconditioners, parallelization, hybridization with integral numerical techniques, better radiation and waveguide boundary conditions and the incorporation of new features (e.g. far field radiation patterns, automatic detection of singularities and discontinuities). It is also left for future work the comparative performance of the classical edge-double-curl formulation versus the nodal-regularized formulation presented in this work.

7.2 Electromagnetic metal forming

We had presented a numerical model for the simulation of electromagnetic metal forming processes. The approach is computationally efficient and very useful for estimating the order of magnitude of the parameters involved in the design of an EMF system. Also, it is able to estimate the optimum frequency and capacitance at which it is attained the maximum workpiece deformation for a given set of coil, workpiece and initial energy. This model also reveals the excellent behavior of ERMES when solving low-frequency problems.

It is left for future work to implement a sequential coupling strategy with ERMES and STAMPACK. A sequential coupling strategy will improve the accuracy of our computations in problems with large deformations and long magnetic pressure pulses. It is also left for future work to study in more detail the influence of the frequency of the discharge in the deformation of the workpiece.

7.3 Transfer impedance of cable shields

We had presented a numerical model for the computation of the transfer impedance of cable shields. This model has been validated for perforated tubes and we had shown that it reproduces the high frequency behavior of the transfer impedance more accurately than the approaches found in the literature.

The next step is to adapt the model to braided wires shields. The objective is to study how the value of the transfer impedance is affected by the geometric disposition of the wires in the braid. Once we know the influence of the path, shape and distance between wires in the same and different carriers we will look for the arrangements with the lowest transfer impedance and the minimum quantity of shielding material.

The numerical model developed for perforated tubes only needs minor changes to be adapted to the new situation described above. We only have to change the PEC and PMC boundary conditions by a periodic boundary condition. Currently, we are implementing the periodic boundary condition in ERMES. Also, we are developing a plug-in module for ERMES able to generate automatically braided wire geometries after being informed of the relevant parameters.

Appendix A

ERMES: Numerical tool for electromagnetic field computations

This appendix is the user manual of ERMES. We explain step-by-step how to run a numerical simulation with this computational tool.

A.1 Description of ERMES

The C++ implementation of the RME-UL method explained in chapter 3 is called ERMES (*Electric Regularized Maxwell Equations with Singularities*). ERMES has a user-friendly interface based on GiD [29]. GiD is employed for geometrical modeling, meshing and visualization of results. The current version of ERMES is mono-processor and it runs in the operative system Windows XP (64-bits and 32-bits). The graphic interface works with GiD 10 and lower versions.

A.2 Installation

ERMES is a problem type of GiD and, therefore, we only have to *copy&paste* the folder *ERMES 6.0* in the folder *problemtypes* of GiD to install it. ERMES is opened in the upper menu of GiD *Data* → *Problem type* → *ERMES 6.0* → *ERMES* (see fig. A.1). The ERMES menu bar appears at the left side of GiD after clicking on *ERMES* (see fig. A.2).

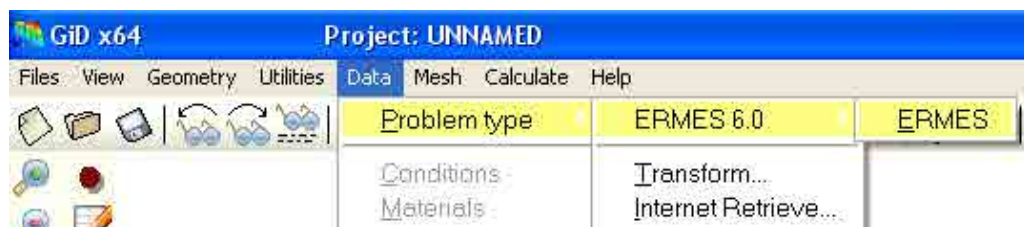


Figure A.1: ERMES is opened in the upper menu of GiD *Data* → *Problem type* → *ERMES 6.0* → *ERMES*.

A.3 Pre-Process

Before running a simulation with ERMES we need to create a geometry, define materials, apply boundary conditions and set problem parameters. The geometry can be imported or created inside GiD. It is important to remember that ERMES needs two different surfaces, joined by *contact elements*, for modeling the discontinuity of the fields in the surface of separation between two media (chapter 3, section 3.4). The materials, boundary conditions and problem parameters must be defined and assigned from the windows associated to the ERMES menu bar. In the following subsections we describe these windows in detail. Once the problem is set up properly, we only have to mesh the geometry (clicking on the *Generate mesh* button) and, finally, execute ERMES (clicking on the *Calculate* button).

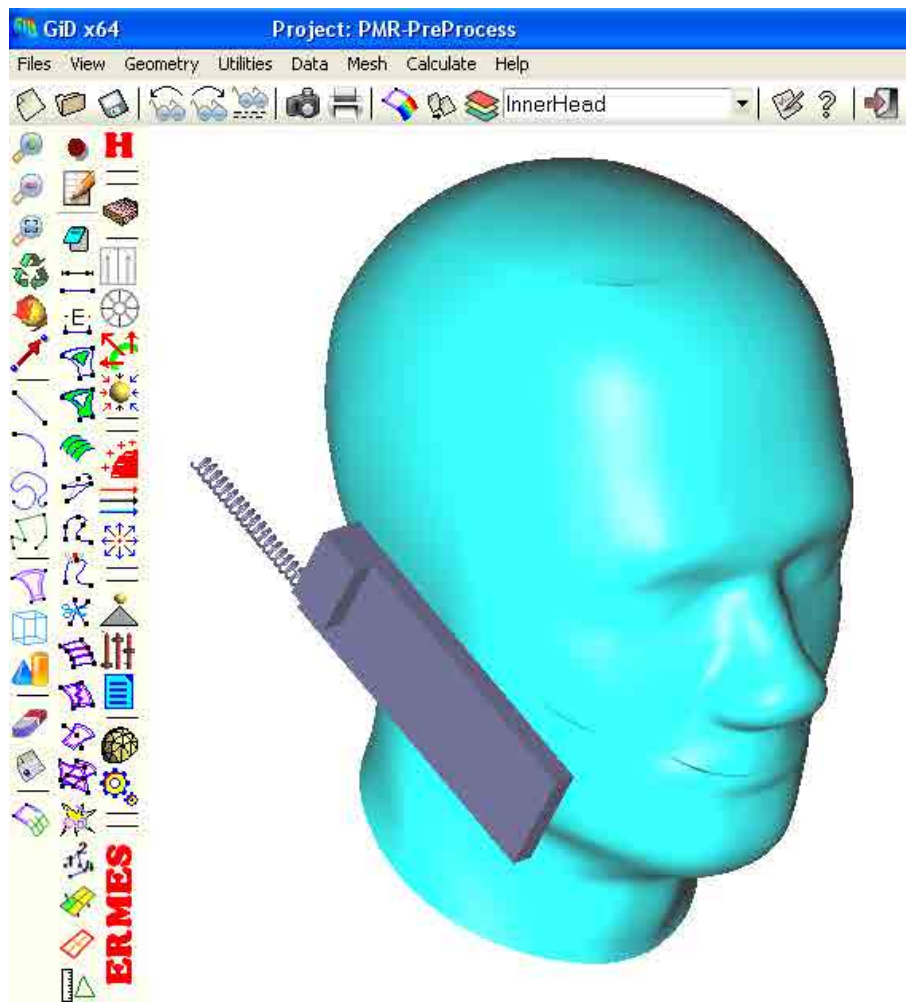


Figure A.2: ERMES menu bar.

A.3.1 Materials

The window *Materials* (see fig. A.3) defines materials and assigns it to the volumes of the geometry. The material properties required are:

- *Electrical conductivity (S/m)*: electrical conductivity σ (S/m).
- *Electric permittivity real*: real part of the relative electric permittivity ϵ'_r (ϵ' / ϵ_0).
- *Electric permittivity img*: imaginary part of the relative electric permittivity ϵ''_r (ϵ'' / ϵ_0).
- *Magnetic permeability real*: real part of the relative magnetic permeability μ'_r (μ' / μ_0).
- *Magnetic permeability img*: imaginary part of the relative magnetic permeability μ''_r (μ'' / μ_0).

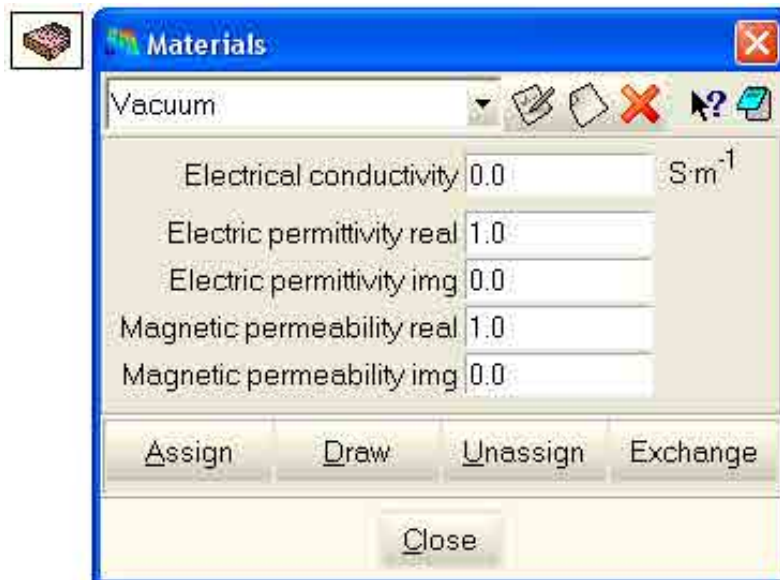


Figure A.3: *Materials* window.

A.3.2 RWPort TE10

The window *RWPortTE10* (see fig. A.4) defines the rectangular waveguide ports. The parameters required are:

- *Port Type*: ID number. *PortType* = 0 for an input port. *PortType* > 0 for an output port.
- *00 X*: X coordinate of the lower left corner of the port.
- *00 Y*: Y coordinate of the lower left corner of the port.
- *00 Z*: Z coordinate of the lower left corner of the port.
- *high X*: X coordinate of the upper left corner of the port.
- *high Y*: Y coordinate of the upper left corner of the port.
- *high Z*: Z coordinate of the upper left corner of the port.
- *width X*: X coordinate of the lower right corner of the port.
- *width Y*: Y coordinate of the lower right corner of the port.
- *width Z*: Z coordinate of the lower right corner of the port.

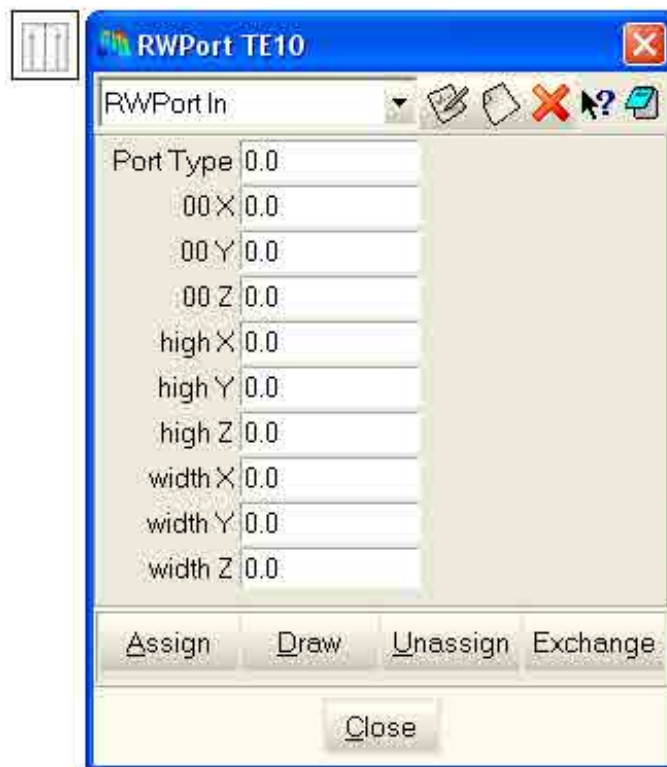


Figure A.4: *RWPortTE10* window.

A.3.3 CoaxialPort TEM

The window *CoaxialPortTEM* (see fig. A.5) defines the coaxial waveguide ports. The parameters required are:

- *Port Type*: ID number. $PortType = 0$ for an input port. $PortType > 0$ for an output port.
- *00 X*: X coordinate of the center of the coaxial waveguide port.
- *00 Y*: Y coordinate of the center of the coaxial waveguide port.
- *00 Z*: Z coordinate of the center of the coaxial waveguide port.
- *Inner radius a*: radius of the inner cylinder of the coaxial waveguide.
- *Exterior radius b*: radius of the exterior cylinder of the coaxial waveguide.
- *Electric permittivity*: real part of the relative electric permittivity ϵ'_r (ϵ'/ϵ_0) of the medium inside the coaxial waveguide.
- *Magnetic permeability*: real part of the relative magnetic permeability μ'_r (μ'/μ_0) of the medium inside the coaxial waveguide.

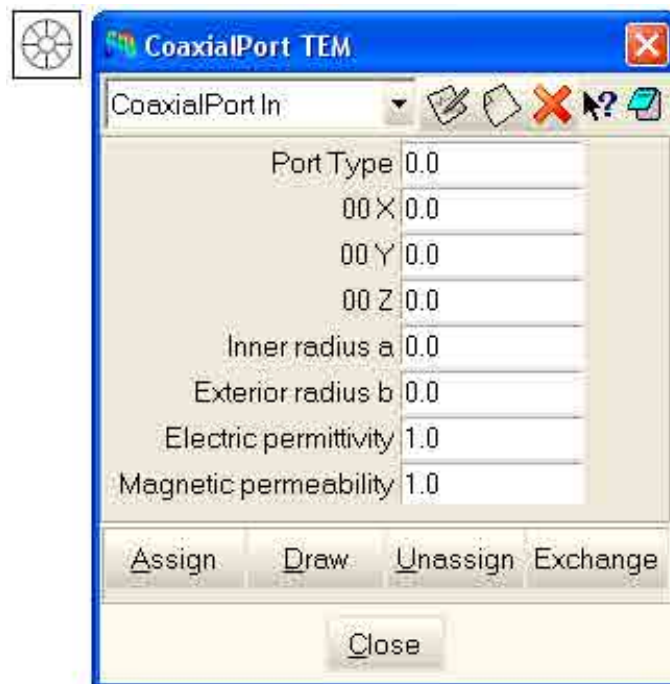


Figure A.5: *CoaxialPortTEM* window.

A.3.4 Generic Robin Coefficients

The window *Generic Robin Coefficients* (see fig. A.6) defines the coefficient γ that appears in the boundary condition

$$\hat{\mathbf{n}} \times \nabla \times \mathbf{E} - \gamma (\hat{\mathbf{n}} \times \hat{\mathbf{n}} \times \mathbf{E}) = 0. \quad (\text{A.1})$$

The parameters required are:

- *Robin coef real*: real part of the coefficient γ .
- *Robin coef img*: imaginary part of the coefficient γ .



Figure A.6: *Generic Robin Coefficients* window.

A.3.5 Current Sources Properties

The window *Current Sources Properties* (see fig. A.7) defines the electric current densities. The parameters required are:

- J_x (A/m^2): modulus of the X component of the electric current density.
- $Phase\ x$ (rad): phase of the X component of the electric current density.
- J_y (A/m^2): modulus of the Y component of the electric current density.
- $Phase\ y$ (rad): phase of the Y component of the electric current density.
- J_z (A/m^2): modulus of the Z component of the electric current density.
- $Phase\ z$ (rad): phase of the Z component of the electric current density.
- J_a (A/m^2): modulus of the angular component of an axis symmetric current density around the Y axis.
- $Phase\ a$ (rad): phase of the angular component of an axis symmetric current density around the Y axis.

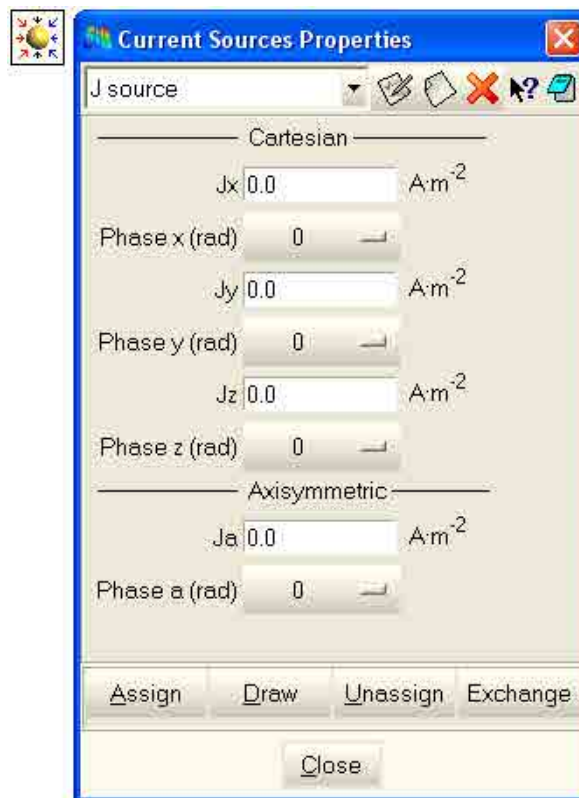


Figure A.7: *Current Sources Properties* window.

A.3.6 Dirichlet Conditions

The window *Dirichlet Conditions* (see fig. A.8) assigns the following conditions:

- *Singularity*: number of *Ungaged Layers* (see section 3.5) around to a point or line.
- *Electric Field PEC*: perfect electric conductor boundary condition ($\hat{\mathbf{n}} \times \mathbf{E} = 0$).
- *Electric Field PMC*: perfect magnetic conductor boundary condition ($\hat{\mathbf{n}} \cdot \mathbf{E} = 0$).
- *Electric Field TE Port*: boundary condition $\hat{\mathbf{n}} \cdot \mathbf{E} = 0$ for waveguide ports. It avoids the geometric average of the boundary normals at the intersection of a port surface with a PMC surface.
- *Correct Contact Normals*: makes coherent the definition of the normals at the surfaces of discontinuity between two media (see section 3.4).

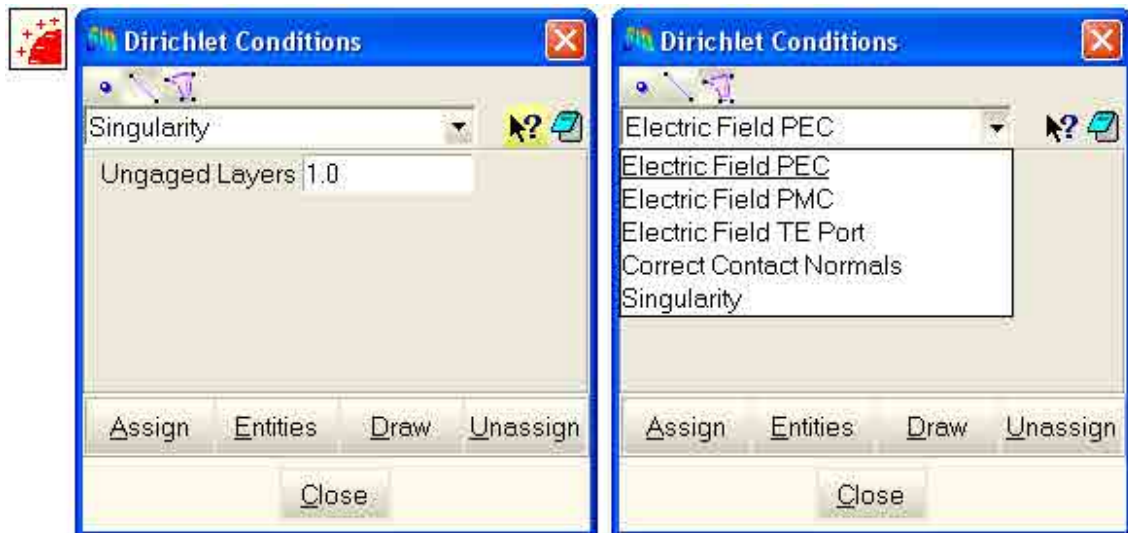


Figure A.8: *Dirichlet Conditions* window.

A.3.7 Robin Conditions

The window *Robin Conditions* (see fig. A.9) assigns the boundary condition

$$\hat{\mathbf{n}} \times \nabla \times \mathbf{E} - \gamma (\hat{\mathbf{n}} \times \hat{\mathbf{n}} \times \mathbf{E}) = \mathbf{U}, \quad (\text{A.2})$$

being the parameters γ and \mathbf{U} the following:

- *RW Port TE10 Conditions*: γ is the propagation constant of the mode TE_{10} .
If $\text{PortType} = 0$ then $\mathbf{U} = -2\gamma (\hat{\mathbf{n}} \times \hat{\mathbf{n}} \times \mathbf{E}_{10})$.
If $\text{PortType} > 0$ then $\mathbf{U} = 0$.
The rectangular waveguide ports are defined in the window *RWPortTE10*.
See sections 3.2, 3.3 and 3.7 for more details.
- *Coaxial TEM Conditions*: γ is the propagation constant of the mode TEM.
If $\text{PortType} = 0$ then $\mathbf{U} = -2\gamma (\hat{\mathbf{n}} \times \hat{\mathbf{n}} \times \mathbf{E}_{\text{TEM}})$.
If $\text{PortType} > 0$ then $\mathbf{U} = 0$.
The coaxial waveguide ports are defined in the window *CoaxialPortTEM*.
See section 4.5.2 for more details.
- *Far Field Condition*: $\gamma = i\omega\sqrt{\epsilon_0\mu_0}$ and $\mathbf{U} = 0$ (sections 3.2 and 3.3).
- *Generic Robin Condition*: γ is defined in the window *Generic Robin Coefficients* and $\mathbf{U} = 0$.

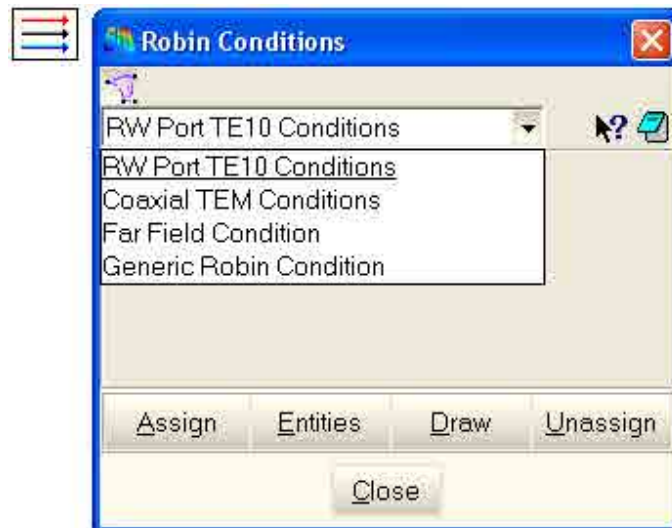


Figure A.9: *Robin Conditions* window.

A.3.8 Current Sources

The window *Current Sources* (see fig. A.10) assigns to volumes the electric current densities defined in the window *Current Sources Properties*.



Figure A.10: *Current Sources* window.

A.3.9 Modes Projection

The window *Modes Projection* (see fig. A.11) selects the waveguide ports, surfaces and volumes over which the computed fields are integrated:

- *Projection RWTE10*: computes the scattering parameter S_{ij} over the selected rectangular waveguide port (see section 3.7).
- *Projection CoaxialTEM*: computes the scattering parameter S_{ij} over the selected coaxial waveguide port (see section 4.5.2).
- *Field Surface Integral*: integrates the fields over the selected surface.
- *Field Volume Integral*: integrates the fields over the selected volume.

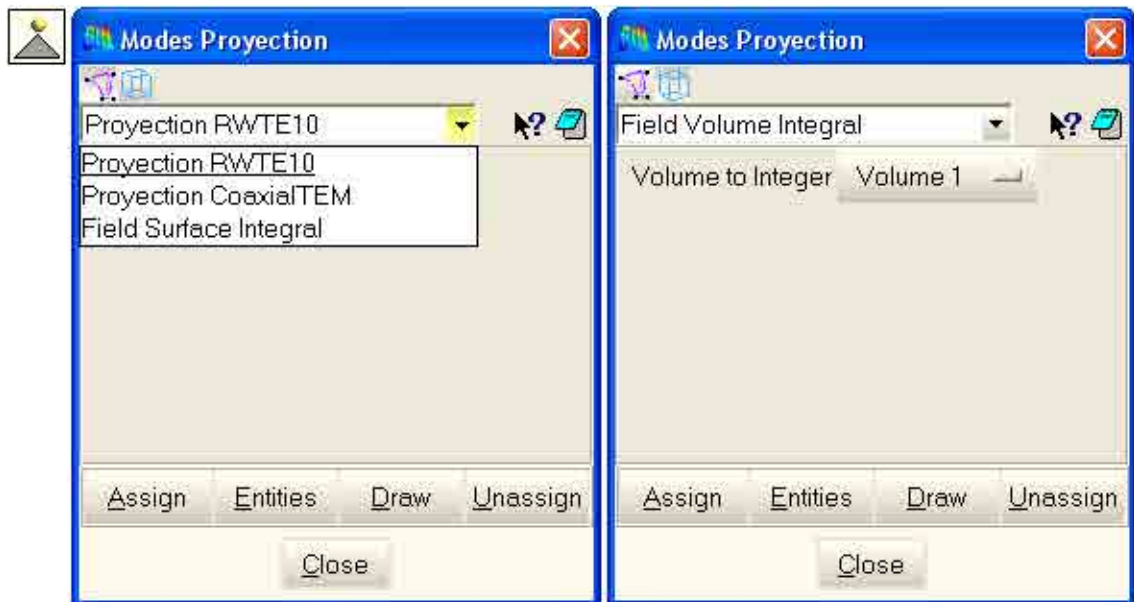


Figure A.11: *Modes Projection* window.

A.3.10 Solving Parameters

The window *Solving Parameters* (see fig. A.12) sets the problem parameters. It contains three tabs: *Frequency*, *Solvers* and *Geometric Data*.

The *Frequency* tab sets the parameters:

- *Frequency (Hz)*: problem frequency in Hz. If the checkbox *Frequency sweep* is checked then it is disabled.
- *Frequency sweep*: frequency sweep starting at *Initial freq*, ending at *End freq* and with a step *Step freq*. If the checkbox *Frequency sweep* is unchecked then it is disabled.

The *Solvers* tab sets the parameters:

- *Solver*: selects the method for solving the linear system.
- *Max iterations*: maximum number of iterations allowed for the iterative solver.
- *Step iterations*: the value of the residual $\|b - Ax\|/\|b\|$ is shown every *Step iterations*.
- *Tolerance*: solution is reached when $\|b - Ax\|/\|b\| < Tolerance$.
- *Preconditioner*: selects a preconditioner for the iterative solver.
- *Initial guess*: reads a file with an initial guess for the iterative solver.
- *Results in file*: writes the solution of the linear system in a file.
If *Results in file* = *No* then the option is disable.
If *Results in file* = *Every step* then the solution is saved every *Step iterations*.
If *Results in file* = *Final step* then the solution is saved when the solver finish.
- *External solver path*: if the option *External solver* is selected in *Solver* then ERMES writes the linear system in a file and executes *External solver path*.
- *Parameters*: parameters for the external solver.

The *Geometric Data* tab sets the parameters:

- *Dimensions*: If *Dimensions* = *3D* then ERMES solves $\mathbf{E} = (E_x, E_y, E_z)$ in all the domain.
If *Dimensions* = *3D-Exy* then ERMES solves \mathbf{E} with $E_z = 0$ in all the domain.
If *Dimensions* = *3D-Ez* then ERMES solves \mathbf{E} with $E_x = E_y = 0$ in all the domain.
If *Dimensions* = *3D-Ea* then ERMES solves $\mathbf{E} = (E_\rho, E_\varphi, E_y)$ with $E_\rho = E_\varphi = 0$ in all the domain (axis-symmetric problem around Y-axis).
- *Length factor (m)*: multiplies all the lengths for the factor indicated:
If *Length factor (m)* = *m* then the factor is 1.
If *Length factor (m)* = *dm* then the factor is 10.
If *Length factor (m)* = *cm* then the factor is 100.
If *Length factor (m)* = *mm* then the factor is 1000.
- *Normal type*: determines the type of smoothing for the boundary and contact normals.
- *Order*: order of the Lagrangian elements (1st, 2nd, 3rd or 4th).

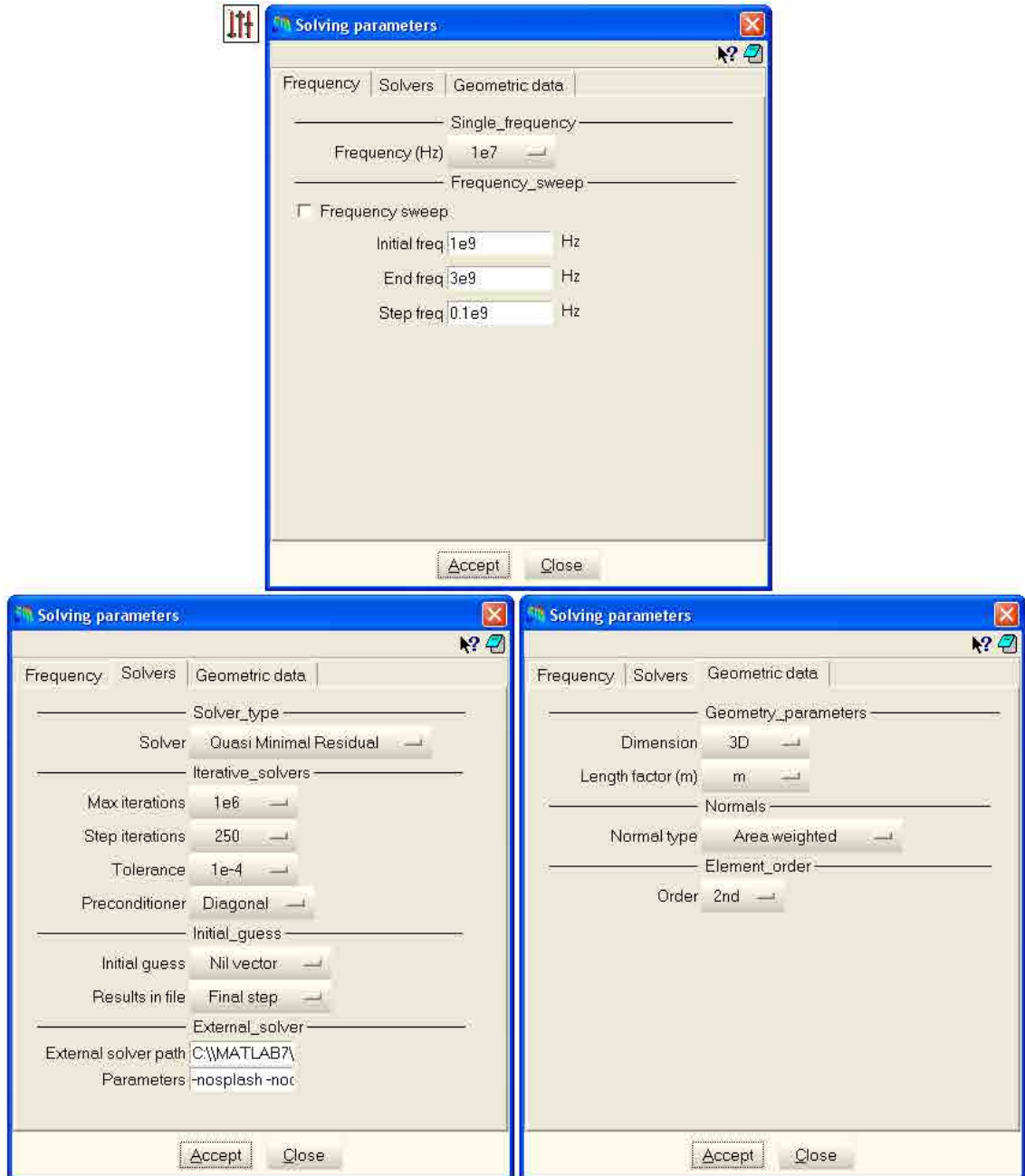


Figure A.12: Solving Parameters window.

A.3.11 Results

The window *Results* (see fig. A.13) selects the results to be displayed in the post process of GiD. It contains three tabs: *Frequency domain*, *Time domain* and *Geometric*.

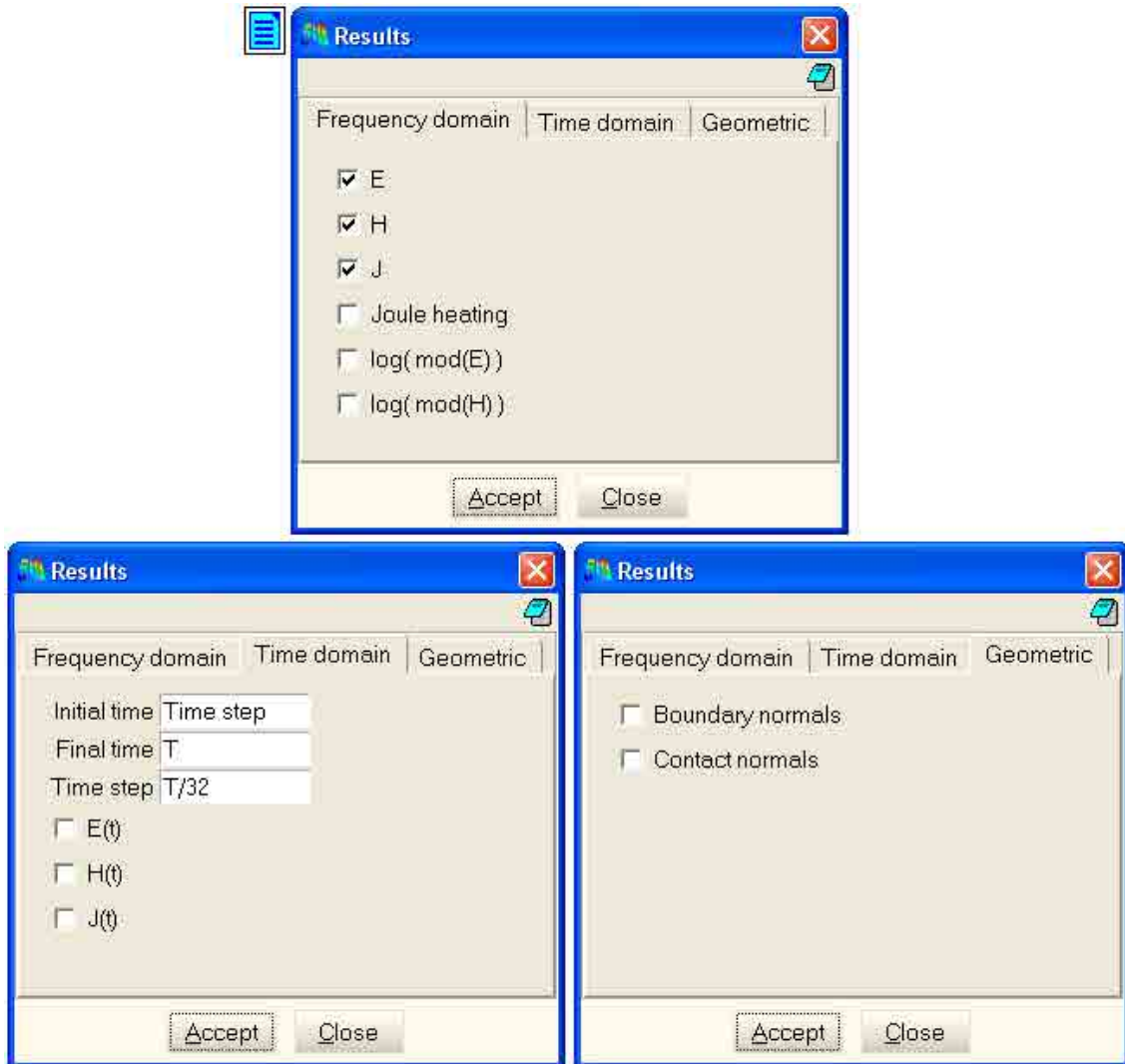


Figure A.13: Results windows.

A.4 Post-Process

ERMES displays the results of the simulations in two different modes: *single frequency* and *frequency sweep*. In the following subsections we explain the characteristics of these modes.

A.4.1 Single frequency

If the checkbox *Frequency sweep* of the window *Solving Parameters* is unchecked then ERMES solves the problem for a single frequency and the results are stored in the file **.flavia.res*. This file located in the folder **.gid*. We can visualize the results by sending the **.flavia.res* file to the GiD post processor. The frequency domain results are in the time step 0 of the *View Results & Deformation* window that we can find in the upper menu of *GiD Window* → *View results*. The time domain results are in the time steps > 0 of the same window. The time domain results are obtained from the frequency domain results with the formula (see section 2.3):

$$\mathbf{F}(\mathbf{r}, t) = \text{Real} [(\mathbf{F}_r(\mathbf{r}) + i \mathbf{F}_i(\mathbf{r}))e^{-i\omega t}] = \mathbf{F}_r(\mathbf{r}) \cos(\omega t) + \mathbf{F}_i(\mathbf{r}) \sin(\omega t). \quad (\text{A.3})$$

In the file **.info*, also located in the **.gid* folder, we can retrieve information related to the solver (residual, size of the problem, iterations, time spent) and the values of the integrals over the surfaces (*intSurf*) and volumes (*intVol*) selected in the window *Modes Projection*.

A.4.2 Frequency sweep

If the checkbox *Frequency sweep* of the window *Solving Parameters* is checked then ERMES solves the problem for the frequencies in the interval (*Initial freq*, *End freq*) with a step of *Step freq*. The results for each frequency are stored in the files **.dat* located in the **.gid* folder. There is a file for every volume or surface selected in the *Modes Projection* window. The name of the surfaces files are *Surfn.dat*, where *n* is the ID of the surface. The name of the volume files are *Vn.dat*, where *n* is the ID of the volume. These files store the values of the surface integrals (*si*) and volume integrals (*vi*) of \mathbf{E} , \mathbf{H} , \mathbf{J} , $|\mathbf{E}|^2$, $|\mathbf{H}|^2$ and $|\mathbf{J}|^2$. If the surface is a waveguide port then the name is *SIj.dat*, being $j = 1$ for the input port and $j = 2, 3, \dots$ for the output ports. In the files *SIj.dat* are stored the values of the scattering parameters S_{1j} for each frequency.

Bibliography

- [1] F. Assous, P. Ciarlet Jr., S. Labrunie, and S. Lohrengel. The singular complement method. *The 13th International Conference on Domain Decomposition Methods, October 9-12, Lyon (France), 2000.*
- [2] C. A. Balanis. *Advanced Engineering Electromagnetics*. John Wiley & Sons, 1990.
- [3] G. Bartels, W. Schaetzing, H.-P. Scheibe, and M. Leone. Simulation models of the electromagnetic forming process. *Acta Physica Polonica A*, 115:1128–1129, 2009.
- [4] F. A. Benson, P. A. Cudd, and J. M. Tealby. Leakage from coaxial cables. *IEE Proceedings*, 139:285–303, 1992.
- [5] J. Van Bladel. Lorenz or Lorentz. *IEEE Antennas and Propagation Magazine*, 33:69, 1991.
- [6] J. Van Bladel. *Singular Electromagnetic Fields and Sources*. IEEE Press, 1991.
- [7] W. E. Boyse, D. R. Lynch, K. D. Paulsen, and G. N. Minerbo. Nodal-based finite-element modeling of Maxwell's equations. *IEEE Transactions on Antennas and Propagation*, 40:642–651, 1992.
- [8] W. E. Boyse and A. A. Seidl. A hybrid finite element method for 3-D scattering using nodal and edge elements. *IEEE Transactions on Antennas and Propagation*, 42:1436–1442, 1994.
- [9] CASSIDIAN. Former EADS Defense & Security. *Elancourt, France*. [Online]. Available: <http://www.cassidian.com>, 2010.
- [10] S. Celozzi, R. Araneo, and G. Lovat. *Electromagnetic Shielding*, chapter 8. John Wiley and Sons, Inc., 2008.
- [11] P. Cendoya, E. Oñate, and J. Miquel. Nuevos elementos finitos para el análisis dinámico elastoplástico no lineal de estructuras laminares. Technical report, International Center for Numerical Methods in Engineering (CIMNE), ref.: M-36, 1997.
- [12] M. Cessenat. *Mathematical Methods in Electromagnetism: Linear Theory and Applications*. World Scientific Publishing, 1996.

- [13] A. Christ and H. L. Hartnagel. Three-dimensional finite-difference method for the analysis of microwave-device embedding. *IEEE Transactions on Microwave Theory and Techniques*, MTT-35(8):688–696, 1987.
- [14] P. Ciarlet. Augmented formulations for solving Maxwell equations. *Computer Methods in Applied Mechanics and Engineering*, 194:559–586, 2005.
- [15] M. Costabel. A coercive bilinear form for Maxwell’s equations. *Journal of Mathematical Analysis and Applications*, 157(2):527–541, 1991.
- [16] M. Costabel and M. Dauge. Maxwell and Lamé eigenvalues on polyhedra. *Mathematical Methods in Applied Science*, 22:243–258, 1999.
- [17] M. Costabel and M. Dauge. Weighted regularization of Maxwell equations in polyhedral domains. *Numerische Mathematik*, 93(2):239–277, 2002.
- [18] P. A. Cudd, F. A. Benson, and J. E. Sitch. Prediction of leakage from single braid screened cables. *IEE Proceedings A*, 133(3):144–151, 1986.
- [19] M. S. Dehra. *High Velocity Formability And Factors Affecting It*. PhD thesis, The Ohio State University, 2006.
- [20] A. S. Bonnet-Ben Dhia, C. Hazard, and S. Lohrengel. A singular field method for the solution of Maxwell’s equations in polyhedral domains. *SIAM Journal on Applied Mathematics*, 59(6):2028–2044, 1999.
- [21] D. M. Dobkin, S. M. Weigand, and N. Iye. Segmented magnetic antennas for near-field UHF RFID. *Microwave Journal*, 50(6), 2007.
- [22] A. El-Azab, M. Garnich, and A. Kapoor. Modeling of the electromagnetic forming of sheet metals: state-of-the-art and future needs. *Journal of Materials Processing Technology*, 142:744–754, 2003.
- [23] Euro Inox. *Stainless Steel: Table of Technical Properties*, volume 5 of *Materials and Applications Series*. Euro Inox, 2007.
- [24] Federal Communications Commission (FCC). Body tissue dielectric parameters. [Online]. Available: <http://www.fcc.gov/oet/rfsafety/dielectric.html>, 2010.
- [25] FEKO. EM simulation software. [Online]. Available: <http://www.feko.info>, 2010.
- [26] FEMM. Finite element method magnetics. *David Meeker, USA*. [Online]. Available: <http://www.femm.info/wiki/HomePage>, 2010.
- [27] G. K. Fenton and G. S. Daehn. Modelling of the electromagnetically formed sheet metal. *Journal of Materials Processing Technology*, 75:6–16, 1998.
- [28] R. W. Freund and N. M. Nachtigal. QMR: A quasi-minimal residual method for non-Hermitian linear systems. *SIAM Journal: Numerische Mathematik*, 60:315–339, 1991.

- [29] GiD. The personal pre and post processor. *International Center for Numerical Methods in Engineering (CIMNE), Barcelona, Spain*. [Online]. Available: <http://www.gidhome.com>, 2010.
- [30] D. J. Griffiths. *Introduction to Electrodynamics*. Prentice-Hall, 3rd edition, 1999.
- [31] Grifols. Biosciencie Division. *Sant Cugat del Vallès, Barcelona (Spain)*. [Online]. Available: <http://www.grifols.com>, 2010.
- [32] F. W. Grover. *Inductance Calculations*. Dover Publications, 2004.
- [33] H. Haase and J. Nitsch. High frequency model for the transfer impedance based on a generalized transmission-line theory. *IEEE International Symposium on EMC*, 2:1242–1247, 2001.
- [34] Y. U. Haiping and L. I. Chunfeng. Effects of current frequency on electromagnetic tube compression. *Journal of Materials Processing Technology*, 209:1053–1059, 2009.
- [35] R. F. Harrington. *Time-Harmonic Electromagnetic Fields*. McGraw-Hill, 1961.
- [36] C. Hazard and M. Lenoir. On the solution of the time-harmonic scattering problems for Maxwell's equations. *SIAM Journal on Mathematical Analysis*, 27:1597–1630, 1996.
- [37] O. Heaviside. On the forces, stresses and fluxes of energy in the electromagnetic field. *Philosophical Transactions of the Royal Society*, 183A:423–480, 1892.
- [38] H. Hinofer-Szalkay. Method of high-precision microsample blood and plasma mass densiometry. *Journal of Applied Physiology*, 60(3):1082–1088, 1986.
- [39] R. Hiptmair. Finite elements in computational electromagnetism. *Acta Numerica*, 1:237–339, 2002.
- [40] L. O. Hoelt and J. S. Hofstra. Measured electromagnetic shielding performance of commonly used cables and connectors. *IEEE Transactions on Electromagnetic Compatibility*, 30:260–275, 1988.
- [41] J. Jablonski and R. Winkler. Analysis of the electromagnetic forming process. *International Journal of Mechanical Sciences*, 20:315–325, 1978.
- [42] J. D. Jackson. *Classical Electrodynamics*. John Wiley & Sons, Inc., 3rd edition, 1999.
- [43] F. Jaspard, M. Nadi, and A. Rouane. Dielectric properties of blood: an investigation of haematocrit dependence. *Physiological Measurement*, 24(1):137–147, 2003.
- [44] J. Jin. *The Finite Element Method in Electromagnetics*. John Wiley & Sons, 2nd edition, 2002.
- [45] C. Johnson. *Numerical Solution of Partial Differential Equations by the Finite Element Method*. Cambridge University Press, 1987.

- [46] M. Kaltenbacher and S. Reitzinger. Appropriate finite-element formulation for 3-D electromagnetic-field problems. *IEEE Transactions on Magnetics*, 38:513–516, 2002.
- [47] S. C. Kashyap. Dielectric properties of blood plasma. *Electronics Letters*, 17(19):713–714, 1981.
- [48] H. Katzier. Streuverhalten elektromagnetischer Wellen bei sprunghaften Übergängen geschirmter dielektrischer leitungen. *Arch. Elek. Übertragung*, 38:290–296, 1984.
- [49] F. Kikuchi. Mixed and penalty formulations for finite element analysis of an eigenvalue problem in electromagnetism. *Computer Methods in Applied Mechanics and Engineering*, 64:509–521, 1987.
- [50] M. Kleiner, A. Brosius, H. Blum, F.-T. Suttmeier, M. Stiemer, B. Svendsen, J. Unger, and S. Reese. Benchmark simulation for coupled electromagnetic-mechanical metal forming processes. *Production Engineering and Development*, 11:85–90, 2004.
- [51] T. Kley. Optimized single-braided cable shields. *IEEE Transactions on Electromagnetic Compatibility*, 35:1–9, 1993.
- [52] R. Kubacki, J. Sobiech, J. Kieliszek, and A. Krawczyk. Comparison of numerical and measurement methods of SAR of ellipsoidal phantoms with muscle tissue electrical parameters. *COMPEL: The International Journal for Computation and Mathematics in Electrical and Electronic Engineering*, 25(3):691–696, 2006.
- [53] I. E. Lager. *Finite Element Modelling of Static and Stationary Electric and Magnetic Fields*. PhD thesis, Delft Univesity, 1996.
- [54] P. D. Ledger and K. Morgan. The application of the hp-finite element method to electromagnetic problems. *Archives of Computational Methods in Engineering*, 12(3):235–302, 2005.
- [55] K. S. H. Lee and C. E. Baum. Application of modal analysis to braided-shield cables. *IEEE Transactions on Electromagnetic Compatibility*, 17:159–169, 1975.
- [56] P. Lorrain, D. R. Corson, and F. Lorrain. *Electromagnetic fields and waves*. W.H. Freeman and Co., 3rd edition, 1988.
- [57] A. G. Mamalis, D. E. Manolakos, A. G. Kladas, and A. K. Koumoutsos. Physical principles of electromagnetic forming process: a constitutive finite element model. *Journal of Materials Processing Technology*, 161:294–299, 2005.
- [58] A. G. Mamalis, D. E. Manolakos, A. G. Kladas, and A. K. Koumoutsos. Electromagnetic forming tools and processing conditions: numerical simulation. *Materials and Manufacturing Processes*, 21:411–423, 2006.

- [59] T. E. Manea, M. D. Verweij, and H. Blok. The importance of the velocity term in the electromagnetic forming process. *The 27th General Assembly of the International Union of Radio Science (URSI 2002), Maastricht, The Netherlands, 17-24 August, 2002.*
- [60] R. R. Mansour, R. S. K. Tong, and R. H. Machpie. Simplified description of the field distribution in finlines and ridge waveguides and its application to the analysis of E-plane discontinuities. *IEEE Transactions on Microwave Theory and Techniques*, 36(12):1825–1832, 1988.
- [61] J. C. Maxwell. A dynamical theory of the electromagnetic field. *Royal Society Transactions*, 155:459–512, 1865.
- [62] J. C. Maxwell. *A Treatise on Electricity and Magnetism*. Oxford Clarendon Press, 1873.
- [63] C. Müller. *Foundations of the Mathematical Theory of Electromagnetic Waves*. Springer-Verlag, 1969.
- [64] J. R. Montejo-Garai and J. Zapata. Full-wave design and realization of multicoupled dual-mode circular waveguide filters. *IEEE Transactions on Microwave Theory and Techniques*, 43(6):1290–1297, 1995.
- [65] T. E. Motoasca. *Electrodynamics in Deformable Solids for Electromagnetic Forming*. PhD thesis, Delft University of Technology, 2003.
- [66] G. Mur. Edge elements, their advantages and their disadvantages. *IEEE Transactions on Magnetics*, 30:3552–3557, 1994.
- [67] G. Mur. The fallacy of edge elements. *IEEE Transactions on Magnetics*, 34:3244–3247, 1998.
- [68] P. J. Nahin. *Oliver Heaviside: The Life, Work, and Times of an Electrical Genius of the Victorian Age*. Johns Hopkins University Press, 2002.
- [69] J. C. Nedelec. Mixed finite elements in R^3 . *Numerische Mathematik*, 35:315–341, 1980.
- [70] R. Nevels and C.-S. Shin. Lorenz, Lorentz, and the gauge. *IEEE Antennas and Propagation Magazine*, 43:70–71, 2001.
- [71] D.A. Oliveira, M.J. Worswick, M. Finn, and D. Newmanc. Electromagnetic forming of aluminum alloy sheet: Free-form and cavity fill experiments and model. *Journal of Materials Processing Technology*, 170:350–362, 2005.
- [72] R. Otin. A high-order nodal finite element formulation for microwave engineering. *The 24th International Review of Progress in Applied Computational Electromagnetics (ACES 2008), March 30-April 4, Niagara Falls (Canada), 2008.*
- [73] R. Otin. Regularized maxwell equations with nodal elements as an alternative approach to the edge-based FEM formulations. *The 9th International Workshop on Finite Elements for Microwave Engineering, May 8-9, Bonn (Germany), 2008.*

- [74] R. Otin. ERMES: Numerical tool for SAR computations. Technical report, International Center for Numerical Methods in Engineering (CIMNE), ref.: IT-584, 2009.
- [75] R. Otin. Numerical study of the thermal effects induced by a RFID antenna in vials of blood plasma. Technical report, International Center for Numerical Methods in Engineering (CIMNE), ref.: IT-583, 2009.
- [76] R. Otin. Regularized Maxwell equations and nodal finite elements for electromagnetic field computations. *Electromagnetics*, 30:190–204, 2010.
- [77] R. Otin. Numerical study of the thermal effects induced by a RFID antenna in vials of blood plasma. *Progress In Electromagnetics Research Letters*, 22:129–138, 2011.
- [78] R. Otin. Specific absorption rate calculations with a nodal-based finite element formulation. *Submitted to Communications in Computational Physics*, 2011.
- [79] R. Otin, R. Mendez, and O. Fruitos. A frequency domain approach to the modeling of electromagnetic metal forming processes. *Submitted to Journal of Materials Processing Technologies*, 2010.
- [80] R. Otin, R. Mendez, and O. Fruitos. A numerical model for the search of the optimum capacitance in electromagnetic metal forming. *Accepted in the 8th International Conference and Workshop on Numerical Simulation of 3D Sheet Metal Forming Processes (NUMISHEET 2011), August 21-26, Seoul (Korea)*, 2011.
- [81] R. Otin, J. Verpoorte, and H. Schippers. A finite element model for the computation of the transfer impedance of cable shields. *Accepted in IEEE Transactions On Electromagnetic Compatibility*, 2011.
- [82] K. D. Paulsen, D. R. Lynch, and J. W. Strohbehm. Numerical treatment of boundary conditions at points connecting more than two electrically distinct regions. *Communications in Applied Numerical Methods*, 3:53–62, 1987.
- [83] K. D. Paulsen, D. R. Lynch, and J. W. Strohbehm. Three-dimensional finite, boundary, and hybrid element solutions of the Maxwell equations for lossy dielectric media. *IEEE Transactions on Microwave Theory and Techniques*, 36:682–693, 1988.
- [84] J. H. Poynting. On the transfer of energy in the electromagnetic field. *Philosophical Transactions of the Royal Society of London*, 175:343–361, 1884.
- [85] D. M. Pozar. *Microwave Engineering*. John Wiley & Sons, 1998.
- [86] K. Preis, O. Bíró, and I. Tícar. Gauged current vector potential and reentrant corners in the FEM analysis of 3D eddy currents. *IEEE Transactions on Magnetics*, 36:840–843, 2000.
- [87] X. Qing, C. K. Goh, and Z. N. Chen. Segmented loop antenna for UHF near-field RFID applications. *Electronics Letters*, 45(7):872–873, 2009.

- [88] Radiall. Design, development and manufacturing of connectors, antennas and microwave components. *Voreppe, France*. [Online]. Available: <http://www.radiall.com>, 2010.
- [89] M. M. Rahmann, J. E. Sitch, and F. A. Benson. Leakage from coaxial cables. *IEE Proceedings*, 127:74–80, 1980.
- [90] J. R. Reitz, F. J. Milford, and R. W. Christy. *Foundations of Electromagnetic Theory*. Addison-Wesley, 1996.
- [91] E. J. Rothwell and M. J. Cloud. *Electromagnetics*. CRC Press LLC, 2001.
- [92] M. Salazar-Palma, T. K. Sarkar, L.-E. García-Castillo, T. Roy, and A. Djordjevic. *Iterative and Self-Adaptive Finite-Elements in Electromagnetic Modeling*. Artech House Publishers, 1998.
- [93] S. Sali. An improved model for the transfer impedance calculations of braided coaxial cables. *IEEE Transactions on Electromagnetic Compatibility*, 33:139–143, 1991.
- [94] S. A. Schelkunoff. The electromagnetic theory of coaxial transmission lines and cylindrical shields. *Bell System Technical Journal*, 13:532–579, 1934.
- [95] H. Schippers, J. Verpoorte, and R. Otin. Electromagnetic analysis of metal braids. *The 9th International Symposium on EMC joint with the 20th International Wroclaw Symposium on EMC (EMC Europe 2010), September 13-17, Wroclaw (Poland)*, 2010.
- [96] H. Schippers, J. Verpoorte, and R. Otin. Electromagnetic analysis of metal braids. *Accepted in the International Symposium and Exhibition on Electromagnetic Compatibility (EMC Europe 2011), September 26-30, York (United Kingdom)*, 2011.
- [97] T. B. A. Senior. Impedance boundary conditions for imperfectly conducting surfaces. *Applied Science Research, sec. B*, 8:418–436, 1960.
- [98] T. B. A. Senior and J. L. Volakis. *Approximate Boundary Conditions in Electromagnetics*. IEE Press, 1995.
- [99] J. Shang. *Electromagnetically Assisted Sheet Metal Stamping*. PhD thesis, The Ohio State University, 2006.
- [100] M. A. Siddiqui. *Numerical Modelling And Simulation Of Electromagnetic Forming Process*. PhD thesis, University of Strasbourg, 2009.
- [101] M. A. Siddiqui, J. P. M. Correia, S. Ahzi, and S. Belouettar. A numerical model to simulate electromagnetic sheet metal forming process. *International Journal of Material Forming*, 1:1387–1390, 2008.
- [102] STAMPACK. A general finite element system for sheet stamping and forming problems. *Quantech ATZ, Barcelona, Spain*. [Online]. Available: <http://www.quantech.es>, 2010.

- [103] J. A. Stratton. *Electromagnetic Theory*. McGraw-Hill, 1941.
- [104] B. Svendsen and T. Chanda. Continuum thermodynamic formulation of models for electromagnetic thermoelastic solids with application in electromagnetic metal forming. *Continuum Mechanics and Thermodynamics*, 17:1–16, 2005.
- [105] N. Takatsu, M. Kato, K. Sato, and T. Tobe. High-speed forming of metal sheets by electromagnetic force. *The Japan Society of Mechanical Engineers International Journal*, 31:142–148, 1988.
- [106] F. M. Tesche, M. Ianoz, and T. Karlsson. *EMC Analysis Methods and Computational Models*, chapter 10. John Wiley and Sons, Inc., 1997.
- [107] R. Tiedemann. Current flow in coaxial braided cable shields. *IEEE Transactions on Electromagnetic Compatibility*, 45:531–537, 2003.
- [108] M. Tyni. The transfer impedance of coaxial cables with braided outer conductor. *Digest of the 10th International Worclaw Symposium on EMC*, pages 410–419, 1976.
- [109] I. Ulacia, I. Hurtado, J. Imbert, M. J. Worswick, and P. L'Eplattenier. Influence of the coupling strategy in the numerical simulation of electromagnetic sheet metal forming. *The 10th International LS-DYNA Users Conference, Dearborn, Michigan USA, June 8-10, 2008*.
- [110] J. Unger, M. Stiemer, M. Schwarze, B. Svendsen, H. Blum, and S. Reese. Strategies for 3D simulation of electromagnetic forming processes. *Journal of Materials Processing Technology*, 199:341–362, 2008.
- [111] E. F. Vance. Shielding effectiveness of braided wire shields. *Interaction note 172*, pages 1–39, 1974.
- [112] E. F. Vance. Shielding effectiveness of braided-wire shields. *IEEE Transactions on Electromagnetic Compatibility*, 17:71–77, 1975.
- [113] R. K. Wangsness. *Electromagnetic fields*. John Wiley & Sons, Inc., 1986.
- [114] J. P. Webb. Edge elements and what they can do for you. *IEEE Transactions on Magnetics*, 29:1460–1465, 1993.
- [115] L. P. Wheeler. *Josiah Willard Gibbs: the history of a great mind*. Ox Bow Press, 1998.
- [116] E. B. Wilson and J. W. Gibbs. *Vector analysis: A text-book for the use of students of mathematics and physics, founded upon the lectures of J. Willard Gibbs*. Charles Scribner's Sons, 1901.
- [117] H. Zhang, M. Murata, and H. Suzuki. Effects of various working conditions on tube bulging by electromagnetic forming. *Journal of Materials Processing Technology*, 48:113–121, 1995.